AD

MEMORANDUM REPORT ARBRL-MR-03377

COMPUTATIONAL STUDY OF INBORE AND INFLIGHT HEATING FOR THE 105MM, M774 PROJECTILE MODIFIED SWEPT FIN

Paul Weinacht
Walter B. Sturek
Perry A. Wooden

August 1984

US ARMY ARMAMENT RESEARCH AND DEVELOPMENT CENTER
BALLISTIC RESEARCH LABORATORY
ABERDEEN PROVING GROUND, MARYLAND

Destroy this report when it is no longer needed.
Do not return it to the originator.

Additional copies of this report may be obtained from the National Technical Information Service, U. S. Department of Commerce, Springfield, Virginia 22161.

The findings in this report are not to be construed as an official Department of the Army position, unless so designated by other authorized documents.

The use of trade names or manufacturers' names in this report does not constitute indorsement of any commercial product.

UNCLASSIFIED

SECURITY CLASSIFICATION OF THIS PAGE *(When Data Entered)*

REPORT DOCUMENTATION PAGE		READ INSTRUCTIONS BEFORE COMPLETING FORM
1. REPORT NUMBER MEMORANDUM REPORT ARBRL-MR-03377	2. GOVT ACCESSION NO. AD-A146 568	3. RECIPIENT'S CATALOG NUMBER
4. TITLE *(and Subtitle)* COMPUTATIONAL STUDY OF INBORE AND INFLIGHT HEATING FOR THE 105MM, M774 PROJECTILE MODIFIED SWEPT FIN		5. TYPE OF REPORT & PERIOD COVERED Final 6. PERFORMING ORG. REPORT NUMBER
7. AUTHOR(s) Paul Weinacht, Walter B. Sturek, & Perry Wooden		8. CONTRACT OR GRANT NUMBER(s)
9. PERFORMING ORGANIZATION NAME AND ADDRESS U.S. Army Ballistic Research Laboratory ATTN: DRXBR-LFD Aberdeen Proving Ground, Maryland 21005 -5066		10. PROGRAM ELEMENT, PROJECT, TASK AREA & WORK UNIT NUMBERS RDT&E 1L162618AH80
11. CONTROLLING OFFICE NAME AND ADDRESS US Army Ballistic Research Laboratory ATTN: DRXBR-OD-ST Aberdeen Proving Ground, MD 21005-5066		12. REPORT DATE August 1984 13. NUMBER OF PAGES 86
14. MONITORING AGENCY NAME & ADDRESS*(if different from Controlling Office)*		15. SECURITY CLASS. *(of this report)* Unclassified 15a. DECLASSIFICATION/DOWNGRADING SCHEDULE

16. DISTRIBUTION STATEMENT *(of this Report)*

Approved for public release, distribution unlimited.

17. DISTRIBUTION STATEMENT *(of the abstract entered in Block 20, if different from Report)*

18. SUPPLEMENTARY NOTES

This report supersedes BRL-IMR-773 and BRL-IMR-782.

19. KEY WORDS *(Continue on reverse side if necessary and identify by block number)*

Aeroheating	Supersonic Flow
Inbore Heating	Unsteady Heat Conduction
Swept Fins	Heat Transfer
Finned Projectiles	Numerical Modeling

20. ABSTRACT *(Continue on reverse side if necessary and identify by block number)*

Fin stabilized kinetic energy penetrator projectiles, such as the M774, have occasionally suffered from severe reduction in fin span due to inbore heating, inflight aerodynamic heating, or a combination of both. This report describes a computational investigation of the inbore and inflight thermal response of the M774 modified swept fins of aluminum and steel composition. The calculations demonstrate that both the inbore and inflight heating of the fin are significant, and that the steel fin shows an improved thermal response over the aluminum fin.

DD FORM JAN 73 1473 EDITION OF 1 NOV 65 IS OBSOLETE

UNCLASSIFIED

SECURITY CLASSIFICATION OF THIS PAGE *(When Data Entered)*

TABLE OF CONTENTS

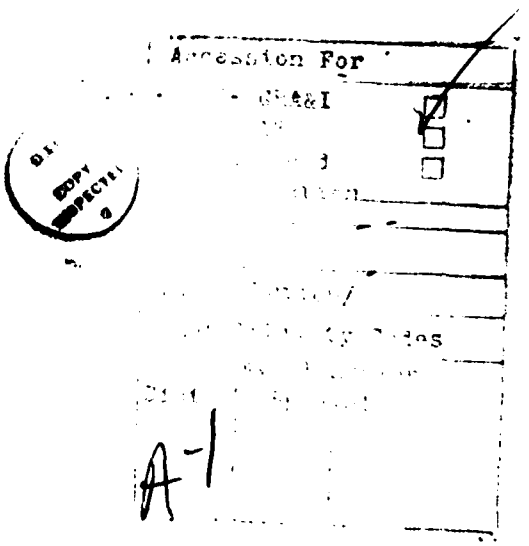

LIST OF ILLUSTRATIONS

LIST OF ILLUSTRATIONS (continued)

LIST OF ILLUSTRATIONS (continued)

LIST OF ILLUSTRATIONS (continued)

I. INTRODUCTION

Fin stabilized kinetic energy penetrator projectiles, such as the M774, have occasionally suffered from severe reduction in fin span due to inbore heating, inflight aerodynamic heating, or a combination of both. These problems compounded by the desire to increase the velocity of future generations of KE projectiles has necessitated investigation into the thermal response of these fins.

Presented in this report are the results of a computational study examining the inbore thermal response of two modified M774 fins and the impending effect on the inflight thermal response of the fins. The computational modeling of the fins consisted of considering the heat conduction in several chordwise two-dimensional sectional cuts of the fin, subjected to heat transfer at the surface. Several fin configurations are investigated here: an aluminum fin with or without a protective aluminum oxide hardcoat, and steel fins of a variety of material composition. The results of the computations are displayed as plots of in-depth temperature at specific times during the projectile flight and as temperature versus time for specific locations on and within the fin.

II: COMPUTATIONAL TECHNIQUES

A. In-bore Modeling

The in-depth, unsteady temperature response has been calculated using a computer code (CONCODE) which solves the two-dimensional, unsteady heat conduction equation with a partially implicit finite-difference computational technique which is second order accurate in space and time in the interior of the domain. The code, developed in part by Dwyer,[1] is formulated in generalized coordinates which facilitates computations for arbitrary geometries.

The fin geometries, shown in Figure 1, correspond to modified M774 fins with 72.7 degree sweep and have been modeled as closely as possible. The coordinate system and an example of the computational grid are shown in Figure 2. The particular fin section shown here corresponds to section 1, the section nearest the fin tip, of the aluminium fin. The computations were carried out with 30 points across the thickness of the fin and 30-35 points along the longitudinal direction of the fin. For those cases with a hardcoat, 10 points were used across the 0.0635 mm thick hardcoat layer. The inbore temperature of the fin was calculated for 15. milliseconds (real time) using 600, time steps.

The boundary conditions for the computations are indicated below. Here T is the local temperature within the fin, n is the unit normal with respect to the boundary, h is the local heat transfer coefficient, H_{amb} is the local

---

1. *H. A. Dwyer, R. J. Kee, and B. R., Sanders, "Adaptive Grid Method for Problems in Fluid Mechanics and Heat Transfer," AIAA Journal, Vol. 18, No. 10, October 1980, pp. 1205-1212.*

recovery enthalpy, H_{wall} is the enthalpy at the fin surface, and k is the local material conductivity.

At time = 0.; Temp= 294.4 K

At the outer boundary

$$h(H_{amb} - H_{wall}) = -k\ (dT/dn)$$

At the inner boundary

$dT/dn = 0$; symmetry condition

The material interface was coupled by requiring equal heat flux from both materials at the junction.

At the material interface

$$-k\ (dT/dn)_{Al} = -k(dT/dn)_{Al\ oxide}$$

At the trailing edge of the fin, one of the two boundary conditions indicated below was used.

Adiabatic condition

$dT/dn = 0$; symmetry condition

Heat flux condition

$$h(H_{amb} - H_{wall}) = -k\ (dT/dn)$$

For the heat flux condition, the values of heat transfer coefficient and recovery enthalpy were equated to the values on the upper surface of the fin at the trailing edge.

The heat transfer coefficient, h, for the inbore calculations was chosen as 13.7 kg/m^2 - s corresponding to that which may be found inside a boiler. The ambient enthalpy, H_{amb}, was calculated based on flame temperatures of 3050. K and 3500. K and yielded values of 2885. and 3356. kJ/kg respectively, with zero enthalpy defined at 289. K. The enthalpy at the boundary, H_{wall}, is obtained by multiplying the local surface temperature by the specific heat at constant pressure of air.

The parameters for the computations and the indentification of the cases run are summarized in Table 1. The physical properties of the materials used for this study are listed in Table 2.

TABLE 1. TWO-DIMENSIONAL COMPUTATIONAL MODELING PARAMETERS

Case ID	Fin Section	Material	T_{flame}	Trailing Edge B.C.
1	1	AL/NoCoating	3050.K	Adiabatic
2	2	AL/NoCoating	3050.K	Adiabatic
3	3	AL/NoCoating	3050.K	Adiabatic
4	1	AL/NoCoating	3500.K	Adiabatic

5	2	AL/NoCoating	3500.K	Adiabatic
6	3	AL/NoCoating	3500.K	Adiabatic
7	1	AL/Coating	3050.K	Adiabatic
8	2	AL/Coating	3050.K	Adiabatic
9	3	AL/Coating	3050.K	Adiabatic
10	1	AL/Coating	3500.K	Adiabatic
11	2	AL/Coating	3500.K	Adiabatic
12	3	AL/Coating	3500.K	Adiabatic
13	1	1050 Steel	3500.K	Adiabatic
14	2	1050 Steel	3500.K	Adiabatic
15	3	1050 Steel	3500.K	Adiabatic
16	1	4130 Steel	3500.K	Adiabatic
17	2	4130 Steel	3500.K	Adiabatic
18	3	4130 Steel	3500.K	Adiabatic
19	1	17-4PH Steel	3500.K	Adiabatic
20	2	17-4PH Steel	3500.K	Adiabatic
21	3	17-4PH Steel	3500.K	Adiabatic
22	1	AL/NoCoating	3500.K	Heat Flux
23	2	AL/NoCoating	3500.K	Heat Flux
24	3	AL/NoCoating	3500.K	Heat Flux

TABLE 2. FIN PHYSICAL PROPERTIES

Material/Property	Specific Heat J/kg-K	Thermal Conductivity W/m-K	Density kg/m^3
Aluminium	869.	43.4	2800.
Coating	794.	30.6	1850.
1050 Steel	439.	46.7	7833.
4130 Steel	585.	39.8	7844.
17-4PH Steel	418.	17.3	7806.

B. Inflight Modeling

Modeling of the inflight temperature response of the fin has been performed using the CONCODE heat conduction code in the same manner as with the inbore computations.

Calculation of the surface heat transfer due to aerodynamic heating was performed using the ASCC-79 code as modified for planar shapes.[2] The resulting values of surface heat transfer coefficient and local recovery temperature (or enthalpy) at the fin surface, representing the aerodynamic heating, served as input to the heat conduction code through the surface boundary conditions. The velocity-time and range-time relationships used for input into the ASCC

---

2. *K. E. Suchland, "Aerothermal Assessment of Projectiles using the ABRES Shape Change Code (ASCC)," Acurex Report TM-80-31-AS, June 1980.*

code are shown in Figures 3 and 4. The results of the inflight surface heat transfer calculations for the cases considered here are discussed in Reference 3.

The initial inflight temperature field inside each fin section was taken from the corresponding inbore calculation after 10. milliseconds of inbore heating. The inflight temperature response within the fin was then calculated in two parts. The first consisted of 30 milliseconds of calculation using the same time step as in the inbore calculations to allow the gradients within the fin to adjust to the new surface heat transfer. The time step was then increased such that an additional 591 steps were required to reach two seconds. (Projectile range = 3. km)

C. Computational Modeling Limitations

The computational modeling limitations for the results discussed in this report are outlined briefly below. These limitations stem from the modeling of the following areas; the convective heat transfer at the fin surface and the heat conduction within the fin.

The modeling of the heat conduction within the fin using a two-dimensional model is the primary limitation in these results because the effect of spanwise heat transfer can not be accounted for. This includes chord to chord heat conduction within the fin, heat conduction at the fin root into the projectile body, and surface heat transfer at the fin tip.

Other limitations in the heat conduction model are due to difficulties in generating a grid to match the sectional fin geometry exactly, and neglecting effects of melting and variation in material properties with temperature.

Uncertainity in the inbore surface heat transfer coefficient is the most significant limitation of the modeling of the convective heat transfer on the fin surface. Other less important limitations in this area are related to neglecting three dimensional variations in the flow field in the calculation of the heat transfer coefficient and recovery enthalpy, neglecting spacial variation in recovery enthalpy, and assuming no change in heat transfer coefficient and recovery enthalpy with variation in wall temperature. The latter, which allows the aeroheating portion of the problem to be decoupled from the heat conduction portion, has been shown[3] to be of minor importance.

III. COMPUTATIONAL RESULTS

A. Inbore Heating Results

Calculation of the inbore unsteady heat conduction within the fin was performed and the results are shown in Figures 5-18. Results are displayed

---

3. *W. B. Sturek, L. D. Kayser, and P. Weinacht, "Computational Study of Swept-Fin Aerodynamic Heating for the 105mm, M774," Ballistic Research Laboratory Memorandum Report to be published.*

as either the variation of temperature with time at a single location in the fin, or as the variation of temperature with position inside the fin at specific times, or as temperature contours within a fin section at specific times. In these figures, the chordwise coordinate, X, has been nondimensionalized by the chord length of section 1, L, while the coordinate across the fin thickness, Y, has been nondimensionalized by the leading edge radius of section 1, R, except in the contour plots where nondimensionalization is in terms of fractions of the chord length of section 1, L.

Results of the calculations of the inbore heating of the aluminum fin with hardcoat subject to the 3500 K flame temperature (Case ID 10, 11, 12) are shown in Figures 5, 6, and 7. Figures 5a,b display the temperatures along the centerline of the fin at 10 and 15 milliseconds respectively. To be noted here is the large temperature gradient near the leading edge. This result is significant because initial melting of the fin has been observed to occur at the leading edge and is due to the increased ratio of the fin surface area to fin volume in this region.

Figures 6a,b display the cross fin temperature profiles at the midchord of each section at 10 and 15 milliseconds and show the large crossfin temperature gradient which is characteristic of inbore heating.

Finally the temperature contours within each of the three fin sections are shown in Figures 7a,b,c. The large temperature gradients across the fin and near the leading edge are again seen. The contours indicate the direction of heat flow is essentially normal to the surface, due to the uniform heat transfer coefficient and flame temperature applied at the surface. These contours, as well the results in Figures 5 and 6, demonstrate the necessity of using a two-dimensional model, as opposed to one-dimensional model, to resolve the heat conduction due to gradients across the fin thickness and along the fin centerline. The results also show the probable existence of relatively small temperature gradients along the fin span, which are not accounted for in the two-dimensional model used here.

The effect of the coating in terms of thermal protection can be seen in Figures 8a,b and 9a,b. Displayed here, respectively, are the crossfin temperature profile and the centerline temperature distribution at 10 and 15 milliseconds for section 1 of the aluminum fin subject to a 3500 K flame temperature both with and without hardcoating. Use of the coating is seen to reduce the temperature at the surface of the aluminum by 26 K at 10 milliseconds and 29 K at 15 milliseconds. Similiar results are found for the other two sections of this fin. Along the fin centerline away from the leading edge, temperatures are reduced by 10 K and 15 K at 10 and 15 milliseconds, respectively, for section 1. Smaller reductions are found for the other two sections along the centerline because of the increased local thickness of the fins.

By examining the rate of heating at the surface of the aluminum near the leading edge, shown in Figure 10, the coating appears to extend the life of the fin inbore by 1.1 millisecond at 10 milliseconds and 1.4 milliseconds at 15 milliseconds.

The variation in the thermal reponse of the fin due to change in the flame temperature is shown in Figures 11a,b and 12a,b. Shown here, respectively, are the cross fin temperature distribution at midchord, and the

centerline temperature distribution at 10 and 15 milliseconds for section 1 of the aluminum fin with a hardcoat subject to flame temperatures of 3050 K and 3500 K. The respective temperature contours are shown in Figures 13 and 7. Increasing flame temperature from 3050 K to 3500 K increases the temperature at the midchord interface by as much at 36 K at 10 milli-seconds and 46 K at 15 milliseconds. For a melt temperature of aluminum of 800 K, the calculations predict that the increase in flame temperature is sufficient to cause melting to occur at the leading edge of the fin at about 15.- 16. milliseconds. Because of the uncertainty in the actual value of the heat transfer coefficient for the inbore heating, these results serve to mainly indicate that melting of the fin is possible in the inbore phase of heating, particularly as the flame temperature is increased and as the fins are exposed to increased duration of inbore heating.

Because of documented melting problems associated with aluminum fins, calculations on a steel fin configuration were made. Three types of steels were investigated, each with a melt temperature greater than 1650 K, significantly above the 800 K melt temperature of aluminum. Figures 14a,b and 15a,b display at 10 and 15 milliseconds the centerline and midchord cross fin temperature distributions, respectively, for section 1 of the steel fin for the three types of steels examined.

These figures demonstrate that the fins remain well below the melt temperature during the 15 milliseconds of inbore heating for each of the three steel types examined, with the 4130 steel fin showing the best performance because of it's larger heat capacity and conductivity.

An increased heat capacity, defined as the weight times the specific heat, allows the fin to experience a smaller increase in net temperature for the same applied heat load. This can be seen in Figure 14 and 15 by comparing the 4130 steel with the 1050 steel. While both have similiar conductivities, the 4130 steel has a larger heat capacity and thus experiences a lower temperature throughout.

The effect of varying the conductivity is also displayed in these figures. Comparing the 17-4PH steel with the 1050 steel which has larger conductivity and similiar heat capacity, it is seen that while both have similiar average temperatures, the 1050 steel has a lower temperature at the surface where the heat load is applied. This is because the 1050 steel, with it's large conductivity, is better able to conduct the heat away from the surface, thus lowering the maximum temperatures within the fin.

Temperature contours within the three sections of the 4130 steel fin, the best performing of the three steel fins, are shown in Figures 16a, b, c for completeness.

The effect of including the trailing edge heat flux boundary condition is shown in Figures 17a,b and 18a,b. From these figures the effect appears to be localized in the trailing edge region and no influence at the critical area near the leading edge for the inbore portion of the flight is seen. The results also show that the effect is more pronounced at sections near the tip of the fin where the ratio of the area at the trailing edge to the total sectional surface area is greater.

B. Inflight Aeroheating Results

Using the results of the inbore heating of the various fin configurations as an initial solution, the unsteady heat conduction within the fin for the aeroheating phase of the projectile flight was calculated. These results, shown in Figures 19-30, are displayed in a manner similiar to the inbore heating results.

Calculation of the inflight temperature response of the aluminum fin with hardcoat following 10 milliseconds of inbore heating (3500 K flame temperature, Case ID 10, 11, 12) was made.

Figure 19 shows the resulting temperature history at the leading edge aluminum/aluminum oxide interface. To be noted here is the temperature drop at the leading edge interface at early time, followed by a steady increase in temperature due the aerodynamic heating of the fin. This drop in temperature at the leading edge is due to the readjusting of the temperature gradients within the fin after the surface heat flux sharply decreases due to the transition from inbore to inflight heating. After this transition, regions near the surfaces where the heat loads are applied experience this drop in temperature while regions away from the surface experience a corresponding increase in temperature as heat is conducted from the hotter regions of the fin to the cooler regions.

Figures 20a, b, c display the centerline temperature distribution of the three sections at 0.5, 1.0, and 2.0 seconds respectively. A large temperature gradient near the leading edge is evident, and though this gradient is not as steep as for the inbore heating, the extent of the gradient encompasses nearly the entire chord. Also shown in these figures is the prediction that section 1 will completely reach the melt temperature as well as substantial portions of sections 2 and 3 by two seconds.

The midchord crossfin temperature distribution for section 1 at 0.5, 1.0, and 2.0 seconds is shown in Figures 21 a,b,c. Compared with the inbore crossfin temperature gradients, the inflight crossfin gradients are significantly smaller due to the differences in inbore and aeroheating heat flux. The magnitude of the gradients inflight is also seen to decrease with time of flight as the projectile slows and the temperature differences between the fin and the surrounding air decrease.

Temperature contours for the case above at section 1 are shown in Figure 22. To be noted here is that the flow of heat is predominantly from the leading edge of the fin to the trailing edge with a small component across the fin thickness. This is significantly different than that observed in the inbore calculations and is due to the high rate of heat transfer at the leading edge inflight, as opposed to essentially uniform surface heat transfer inbore.

Figures 20, 21, and 22 demonstrate the multi-dimensionality of the heat conduction within the fin, and emphasize the need for a fairly sophisticated model of the fin. Temperature gradients across the fin thickness and along the chordwise direction, resolved by the current two-dimensional model, are evident, and the probable existence of gradients across the fin span is demonstrated. While a three dimensional model is desirable and necessary to resolve the spanwise gradients, the effect of including spanwise gradients

would be a small redistribution of some of the heat at sections near the tip to sections at the fin root.

The effect of the coating on the inflight thermal response of the aluminum fin is shown in Figures 23 and 24a, b, c. Figure 23 displays the inflight temperature history on the surface of the aluminum at the leading edge for sections 1 and 3 with and without hardcoating. The coating appears to provide a significant degree of protection at the leading edge of section 3, delaying melting here by 0.22 seconds, and less at section 1, where melting is delayed by only 0.05 seconds. The smaller leading edge radius at section 3 in relation to the coating thickness accounts for the difference in the degree of protection at the two sections.

Figures 24a,b,c display the centerline temperature distribution of the above sections at 0.5, 1.0, and 2.0 seconds. The degree of protection at the leading edge of section 3 is again evident. At the midchord position the coating appears to reduce the temperature in each of the fin sections by about 10 K.

The variation in the inflight thermal response of the fin due to changes in the inbore flame temperature is shown in Figure 25 and 26a,b,c. Shown in Figure 25 is the inflight time history of the temperature at the leading edge aluminum/aluminum oxide interface for sections 1 and 3 of the aluminum fin with hardcoating subject to flame temperatures of 3050 K and 3500 K. This figure demonstrates that fins subject to a higher flame temperature will leave the gun tube at higher temperatures and remain hotter throughout the flight, requiring less time to sustain damage. For the case shown in Figure 25 the calculations predict that increasing the flame temperature from 3050 K to 3500 K will cause melting at the leading edge to occur 0.06 seconds sooner.

It should be noted that this analysis does not take into account the effect of any damage the fin might experience inbore, which may cause the fin to experience increased surface heat transfer. Thus if the fin sustained damage inbore for the higher flame temperature, and none for the lower heat transfer, the difference between the time of failure of the fins may be significantly greater than the 0.06 seconds indicated above.

Figures 26a,b,c display the centerline temperature distribution at sections 1 and 3 of the aluminum fin with hardcoat for the two flame temperatures at 0.5, 1.0, and 2.0 seconds. The difference in the temperatures of the fins subject to the two flame temperatures is seen to decrease during the flight, due to the slightly higher surface heat transfer to the cooler fin.

Results were obtained for the inflight thermal response of the three steel fins. It should be noted that although the steel fins are not expected to melt inflight because the melt temperature is well above the recovery temperature, substantial structural weakening is possible, necessitating the evaluation of the temperature response of the steel fins. Shown in Figure 27 is the temperature history at the leading edge for section 1 of the three steel fins. The 4130 steel fin is seen to have the lowest temperature at this position throughout the flight, while the 17-4PH steel fin, the thermally poorest performing fin of the three, actually heats up to the recovery temperature at about 1.2 seconds on the leading edge.

Figures 28a,b,c display the centerline temperature distribution at section 1 of the three steel fins at 0.5, 1.0, and 2.0 seconds respectively. The 4130 steel fin shows the lowest temperature at each point along the centerline, primarily due to its larger specific heat, for the reasons discussed in the inbore results.

Inflight temperature contours for the 4130 steel fin at each of the three sections are shown in Figures 29a,b,c. The leading edge to trailing edge flow of heat, characteristic of the inflight heating is again seen.

The effect of including the heat flux at the trailing edge is displayed in Figures 30a, b, c. Shown here is a comparison of the centerline temperature distribution with and without heat flux at the trailing edge for section 1 and 3 at 0.5, 1.0, and 2.0 seconds inflight. Though there is some heat load applied at the trailing edge inflight, the inflight heat conduction appears to involve mainly diffusion of the heat load applied there inbore, and is seen to be most significant at sections near the fin tip where the heat is able to diffuse across the entire chord length during the flight.

IV. DISCUSSION AND CONCLUSIONS

The results of this computational study demonstrate that both the inbore and inflight heating contribute significantly to the thermal response of the fins. The results show that the heat conduction inbore proceeds nearly normal to the surface and is characterized by large gradients in this direction. Inflight the flow of heat is seen to be mainly from the leading edge of the fin to the trailing edge with a small component across the fin thickness. The results establish the fact that the heat conduction within the fin is multi-dimensional and should be modeled as such to properly resolve the thermal response of the fin.

The following conclusions were reached after examining the results of this study.

-The calculations predict that melting of portions of the aluminum fin is expected to occur inflight.

-Melting of the fins inbore is possible particularly for high values of flame temperature and heat transfer coefficient.

-Areas near the leading edge and at the fin tip are thermally the most critical both inbore and inflight.

-The aluminum oxide coating has a positive effect in terms of thermal protection, though the results indicate that it is small.

-Increasing the flame temperature will increase the temperature within the fin, particularly at the leading edge and on the fin surface inbore.

-In contrast to the aluminum fins, the steel fins which have a higher melt temperature, show an improved thermal response, and warrant

consideration for future generations of KE penetrator projectile fins.

-The thermal performance of a fin can be improved by replacing its original material by a material with larger values of melt temperature, heat capacity, and conductivity.

V. RECOMMENDATIONS

1. In the design of future generations of KE penetrator fins, serious consideration should be given to fins composed of materials with a higher melt temperature than the aluminum currently used, but not at the expense of significantly decreasing the current values of conductivity and heat capacity. One such material which meets these requirements is the 4130 steel examined here.

2. Additional computational effort should be carried out to establish the capability within AMCCOM to model the inbore and inflight heating for the full three dimensional geometry of the swept fin.

PLAN VIEW OF THE MODIFIED
M774 ALUMINUM FIN

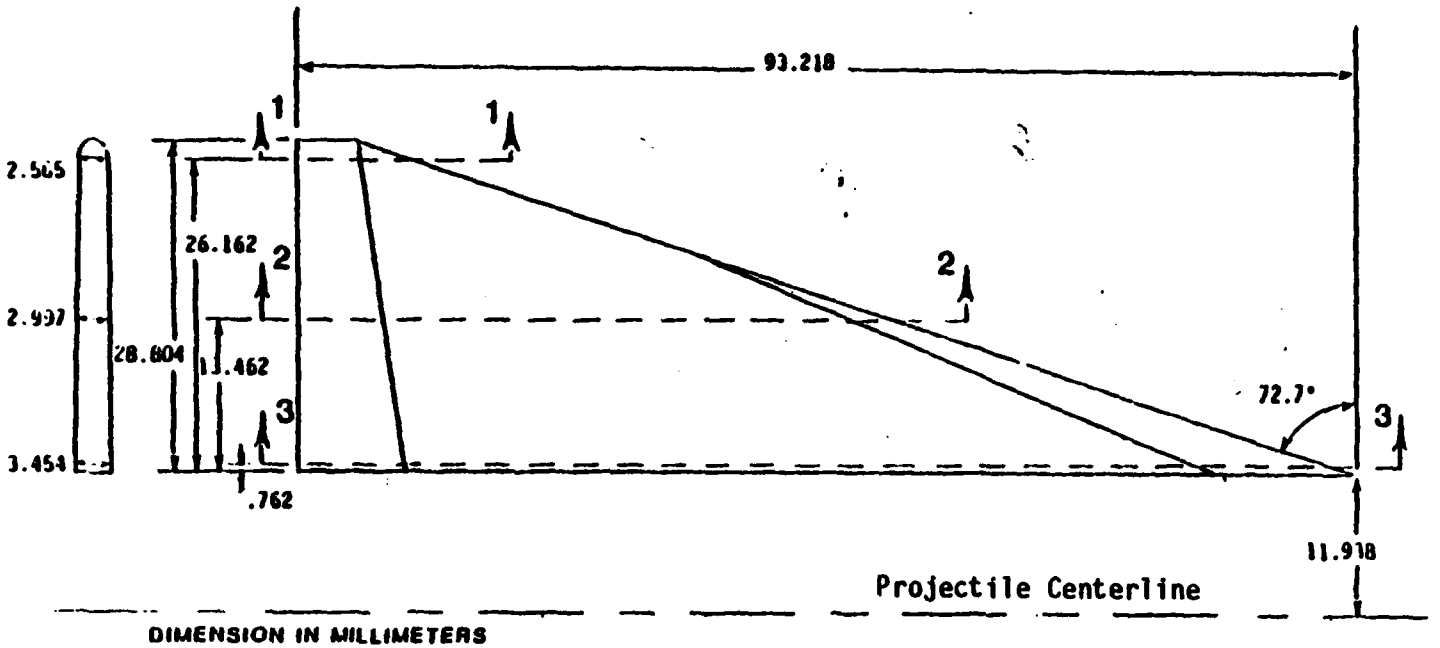

Figure 1a. Planform Drawing of the Modified Swept Fin

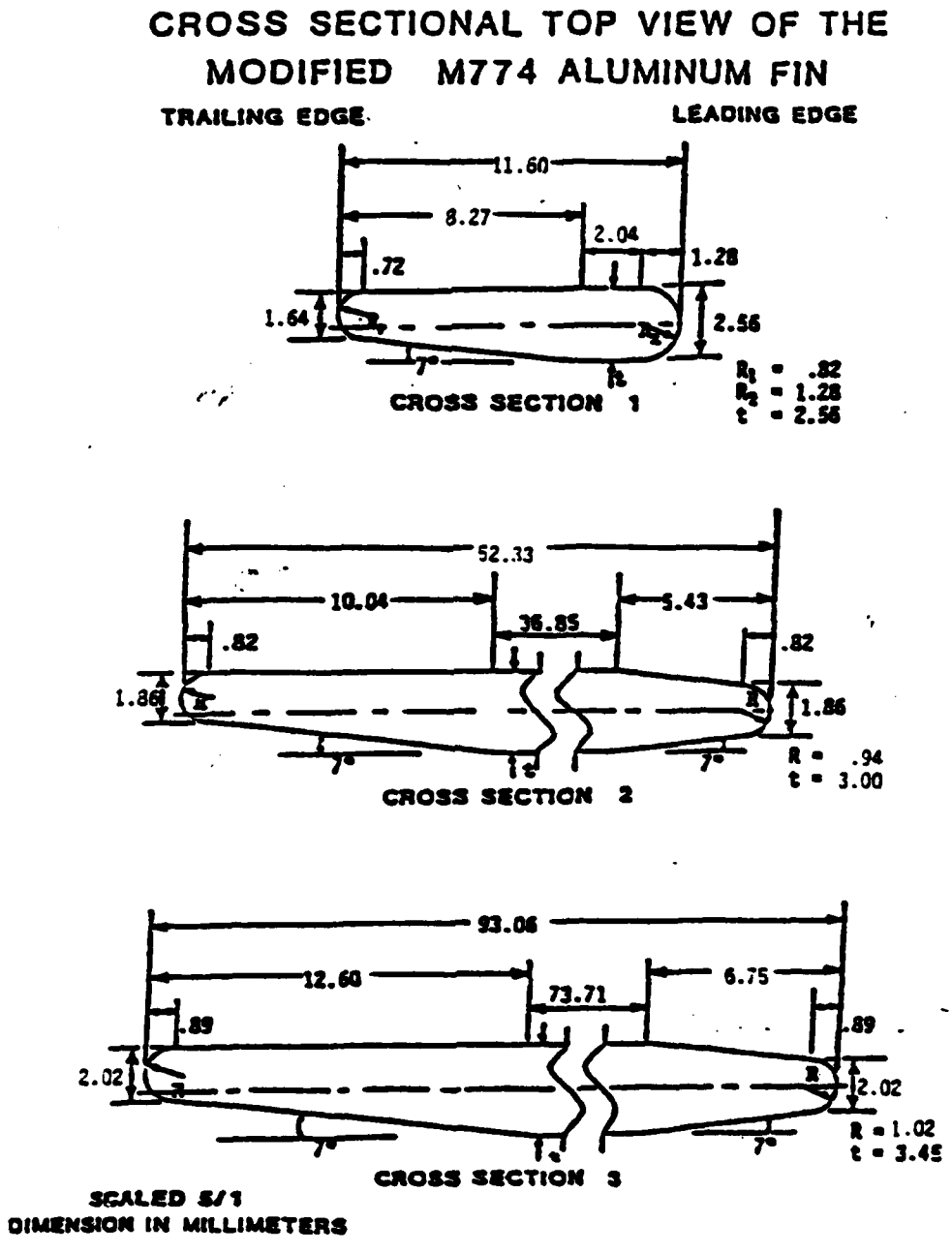

Figure 1b. Cross Sectional Drawings of the Aluminum Fin

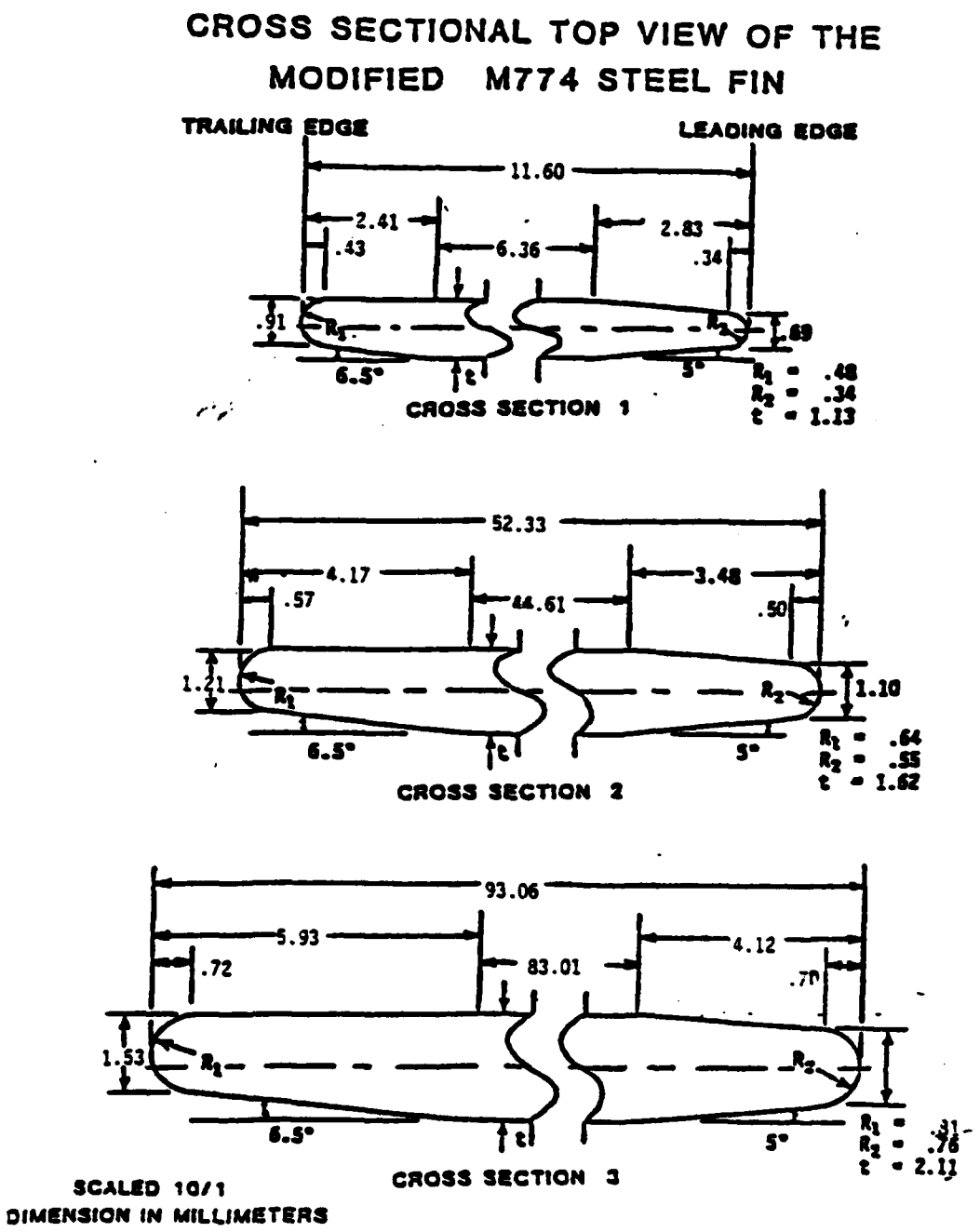

Figure 1c. Cross Sectional Drawings of the Steel Fin

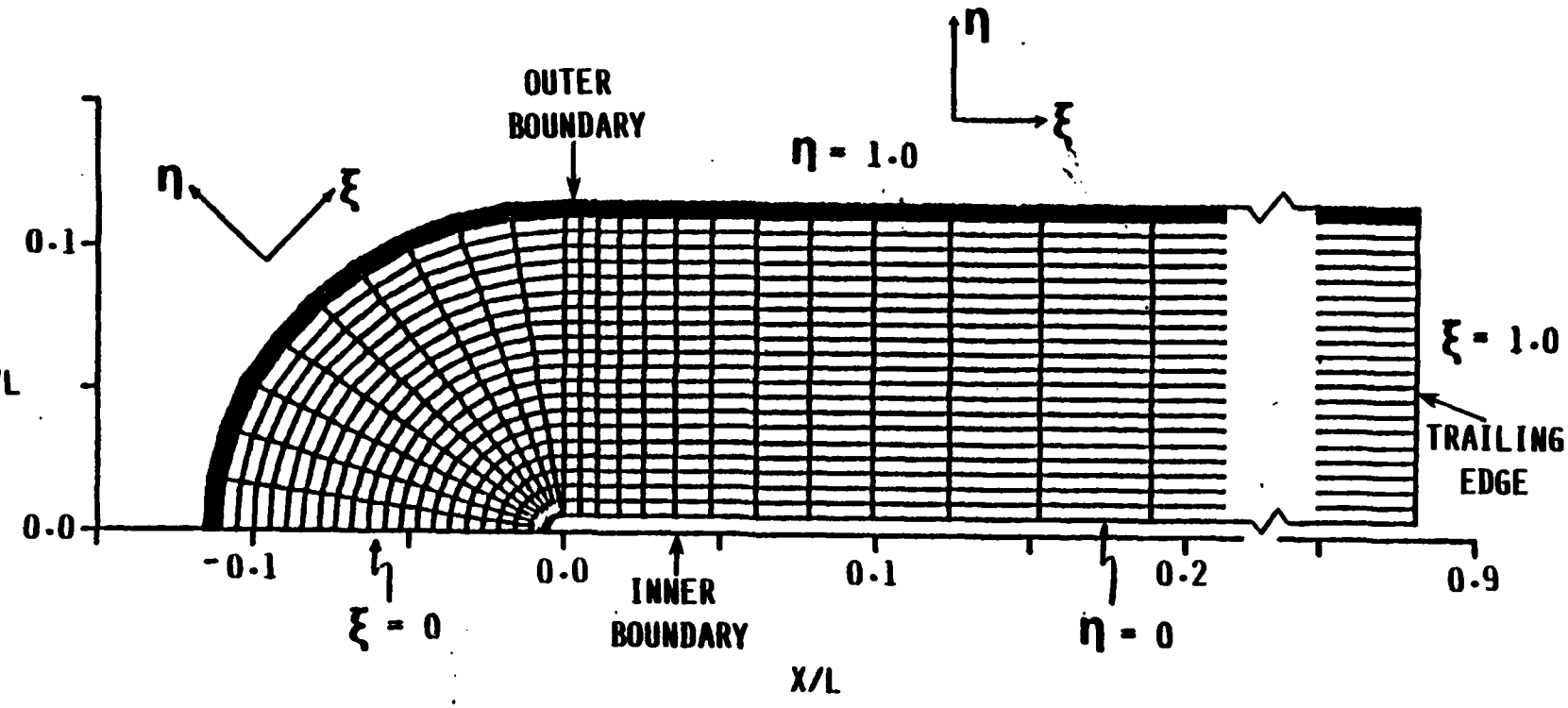

Figure 2. Computational Grid for the 2D Calculations

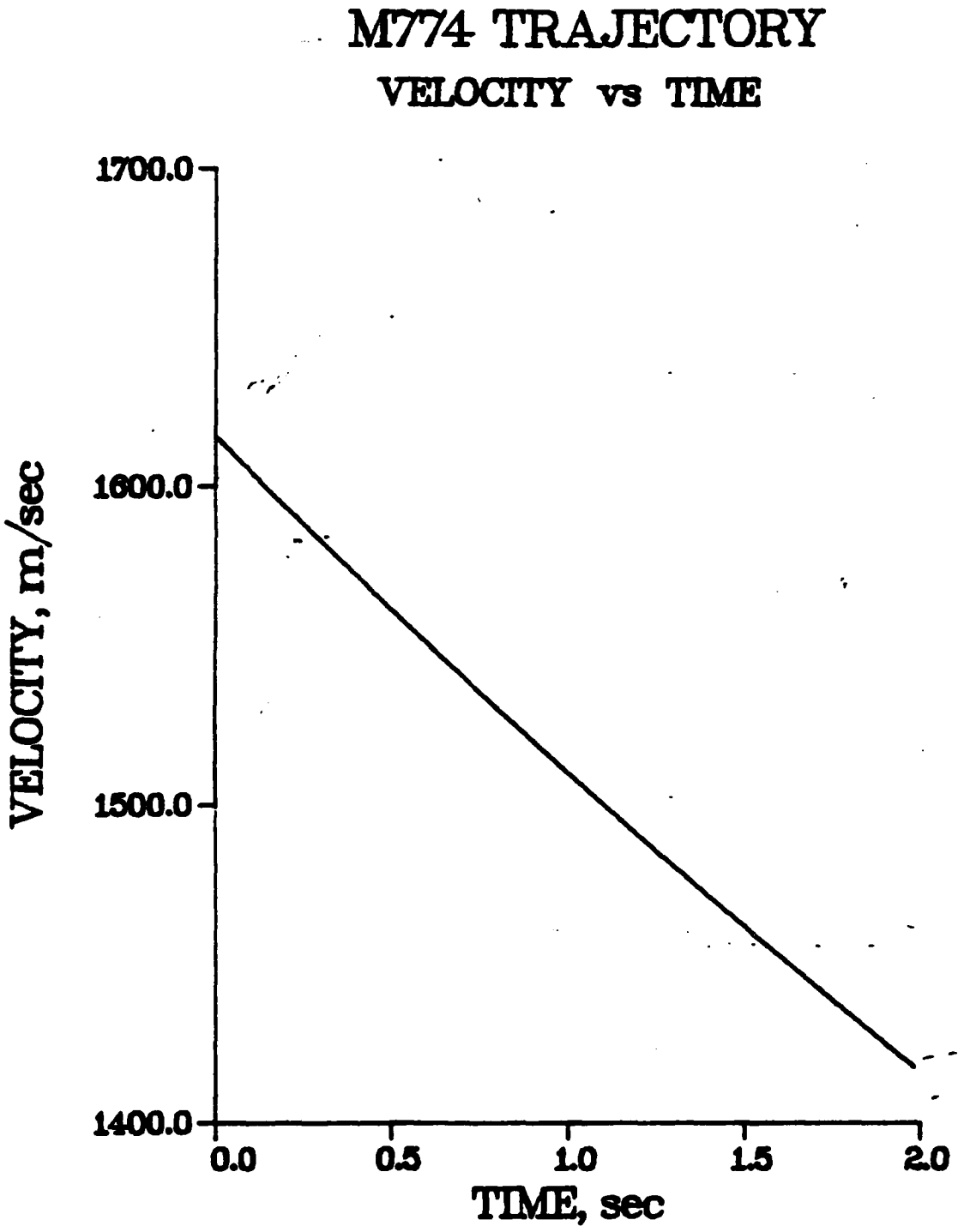

Figure 3. Velocity-Time Relationship Used as Input for ASCC-79 Code

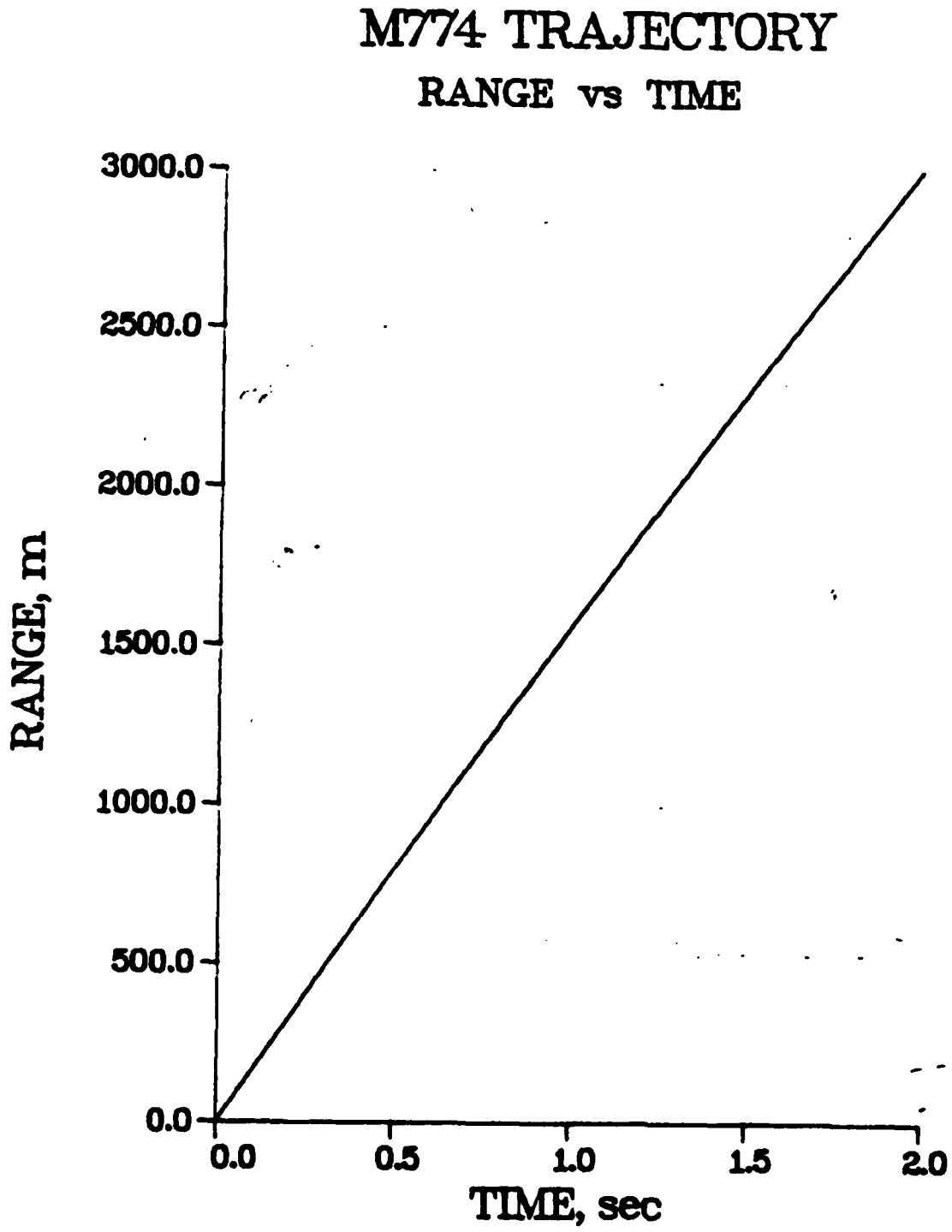

Figure 4. Range-Time Relationship for the M774

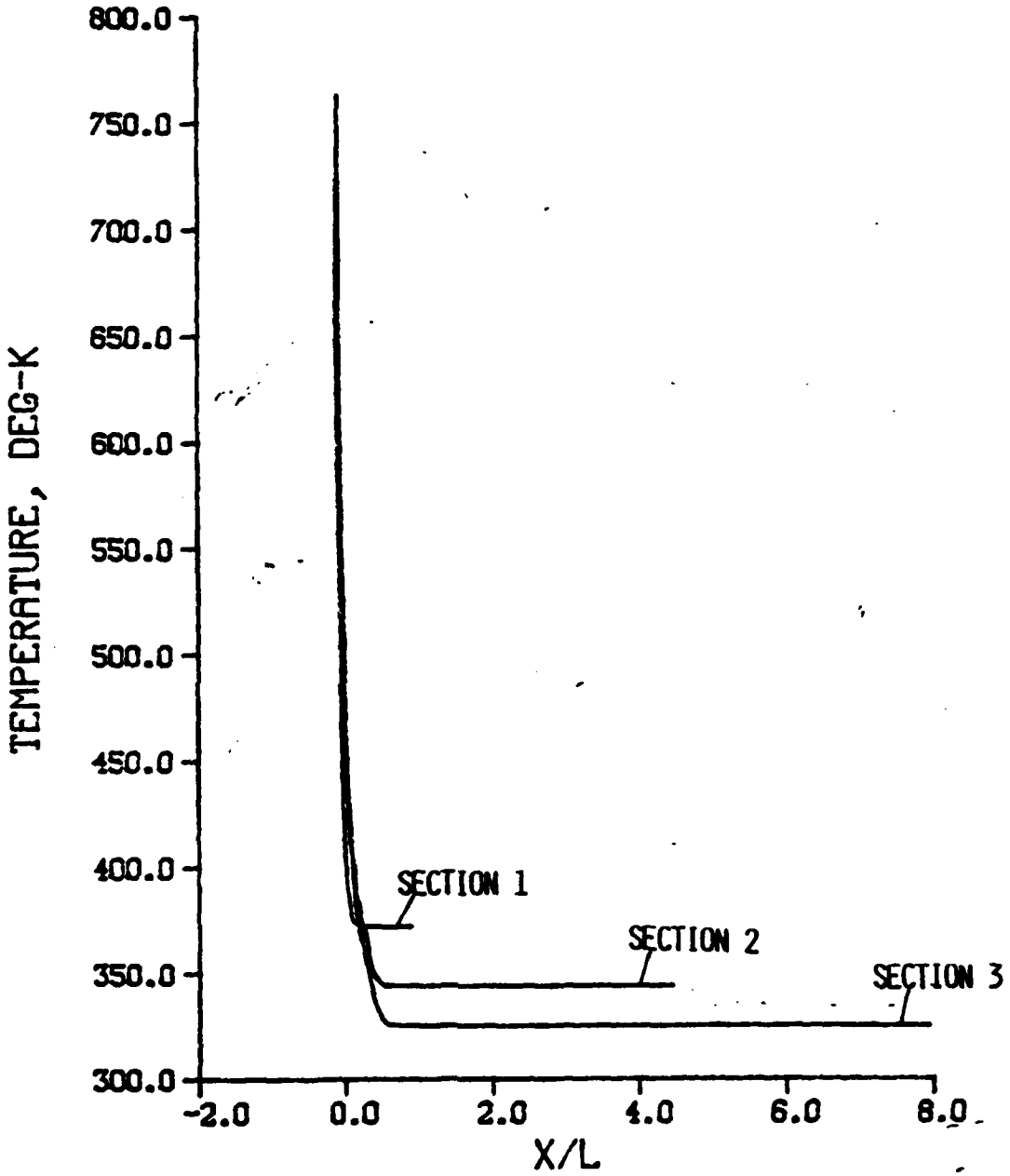

Figure 5. Temperature Along Fin Centerline, Aluminum Fin with Hardcoating, T_{flame} = 3500. K, Case ID 10, 11, 12

a. t = 10. milliseconds

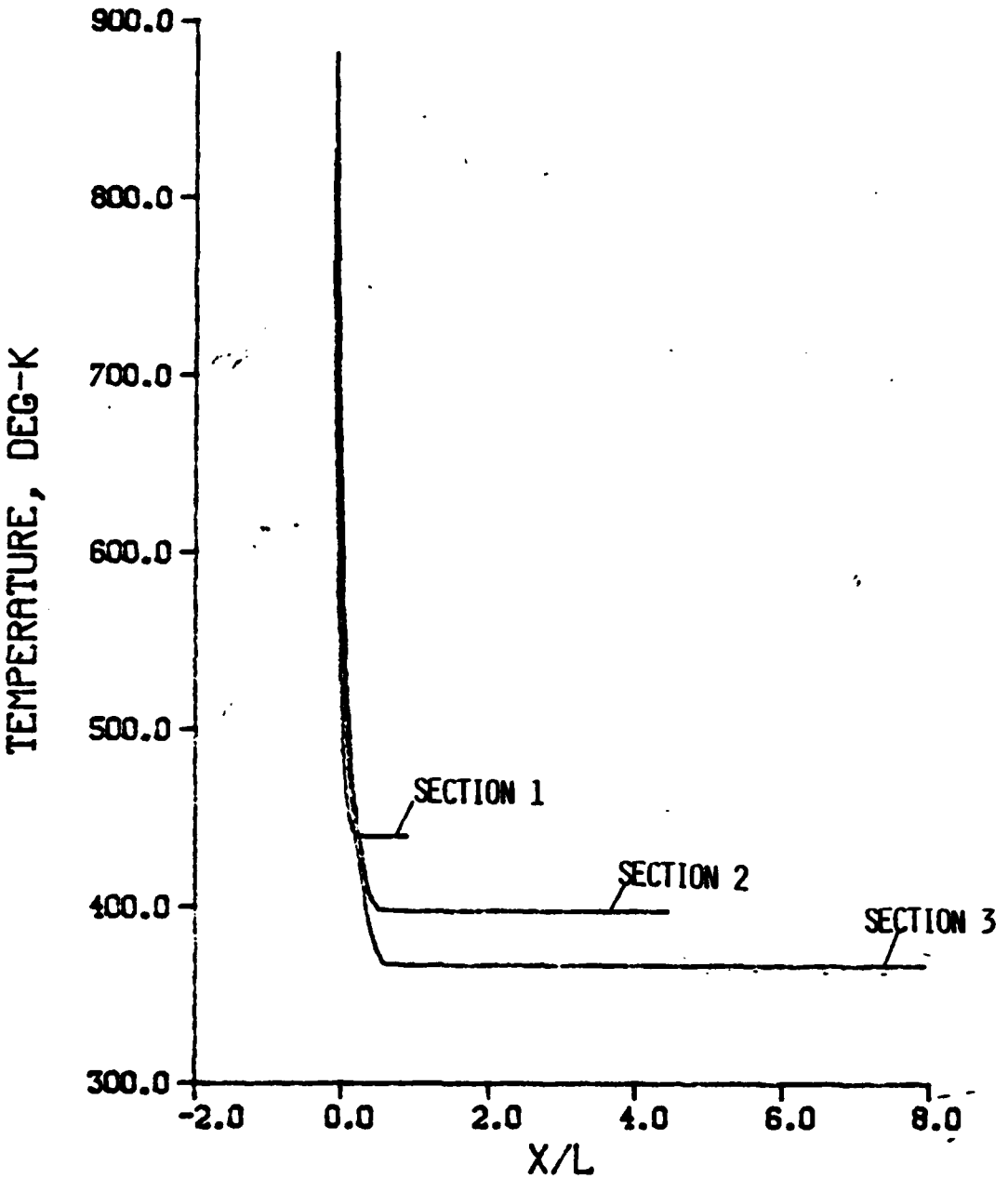

Figure 5. Continued

b. t = 15. milliseconds

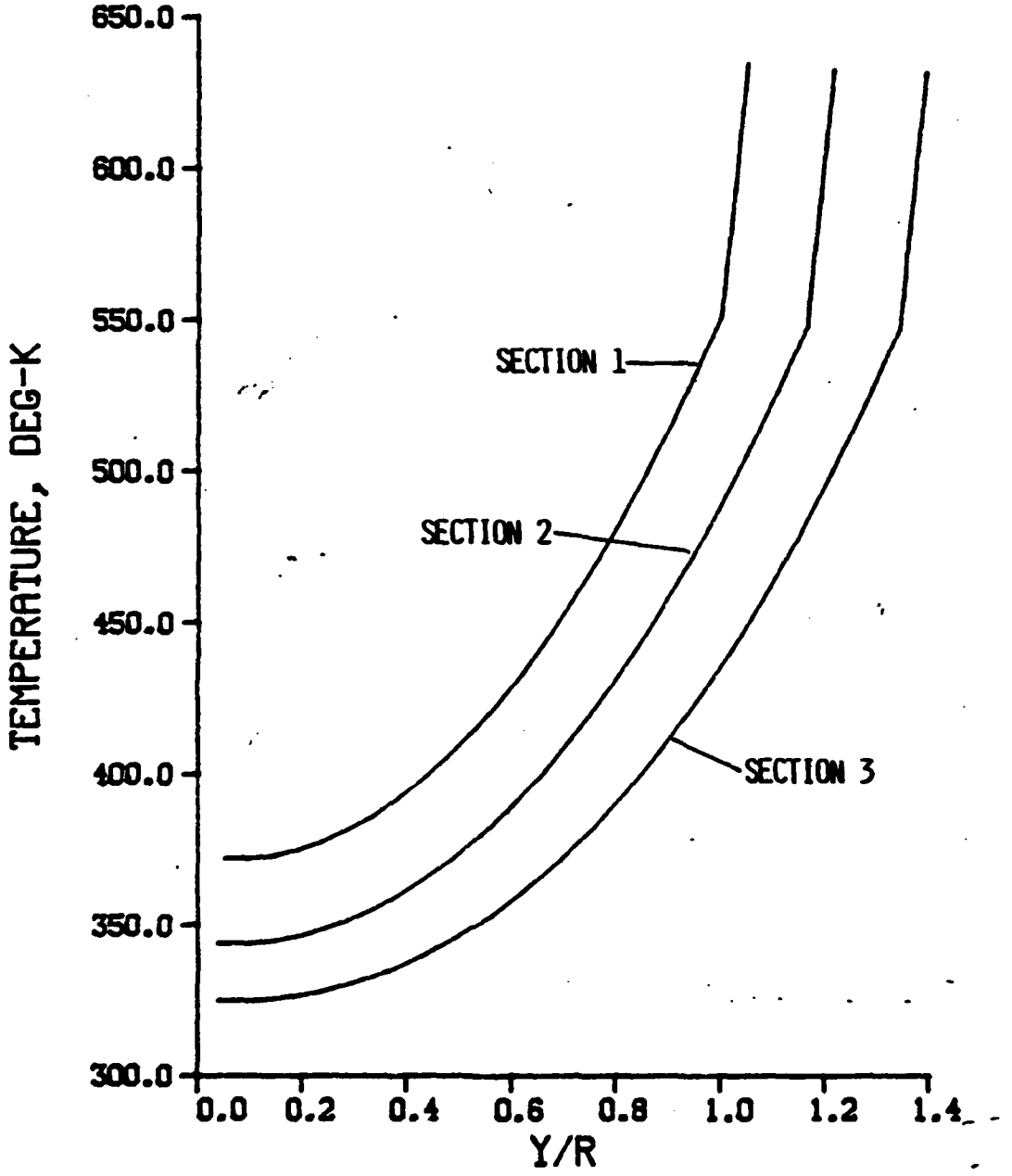

Figure 6. Temperature Profile Across Fin at Midchord, Aluminum Fin with Hardcoating, T_{flame} = 3500. K, Case ID 10, 11, 12

a. t = 10. milliseconds

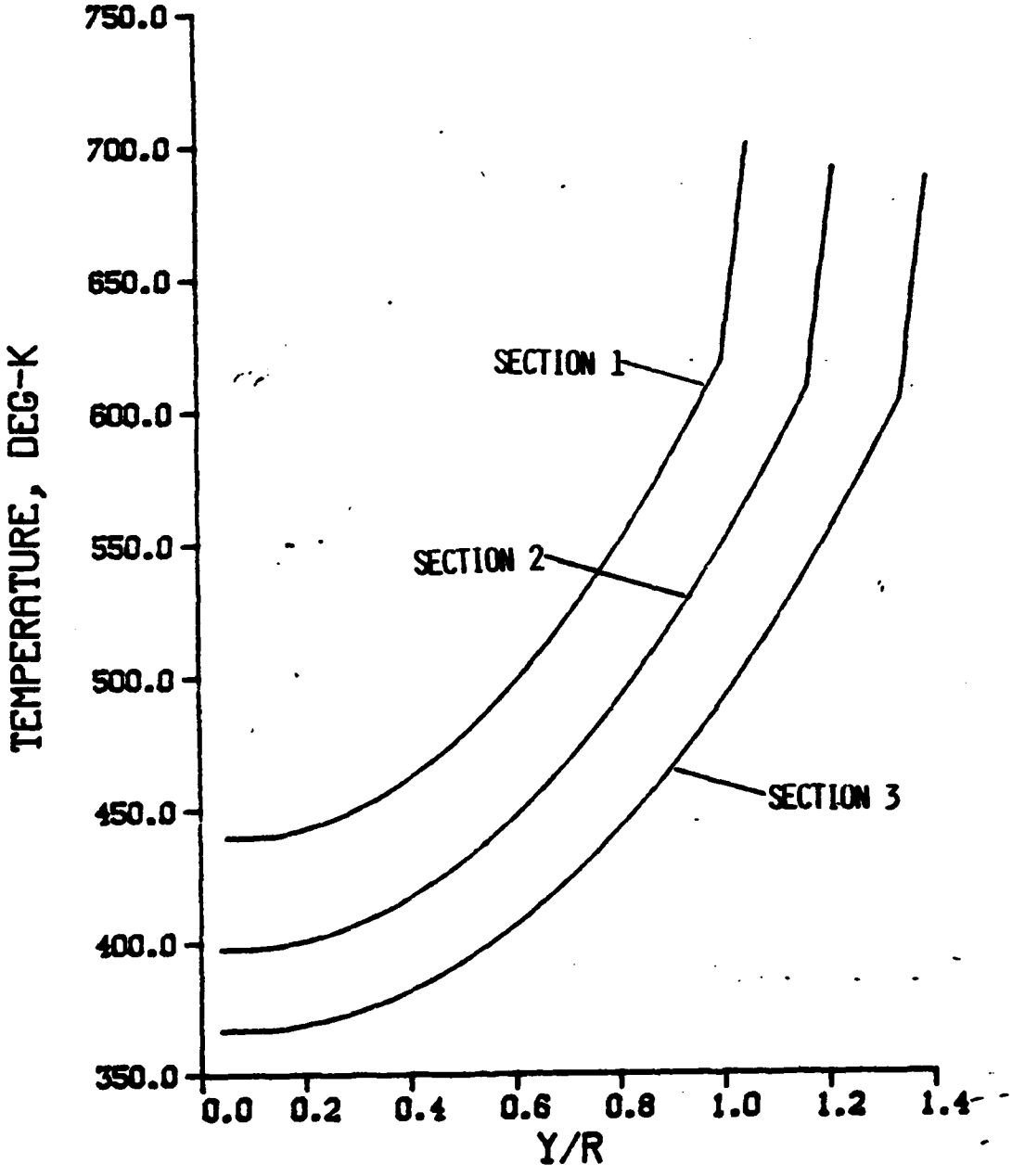

Figure 6. Continued

b. t = 15. milliseconds

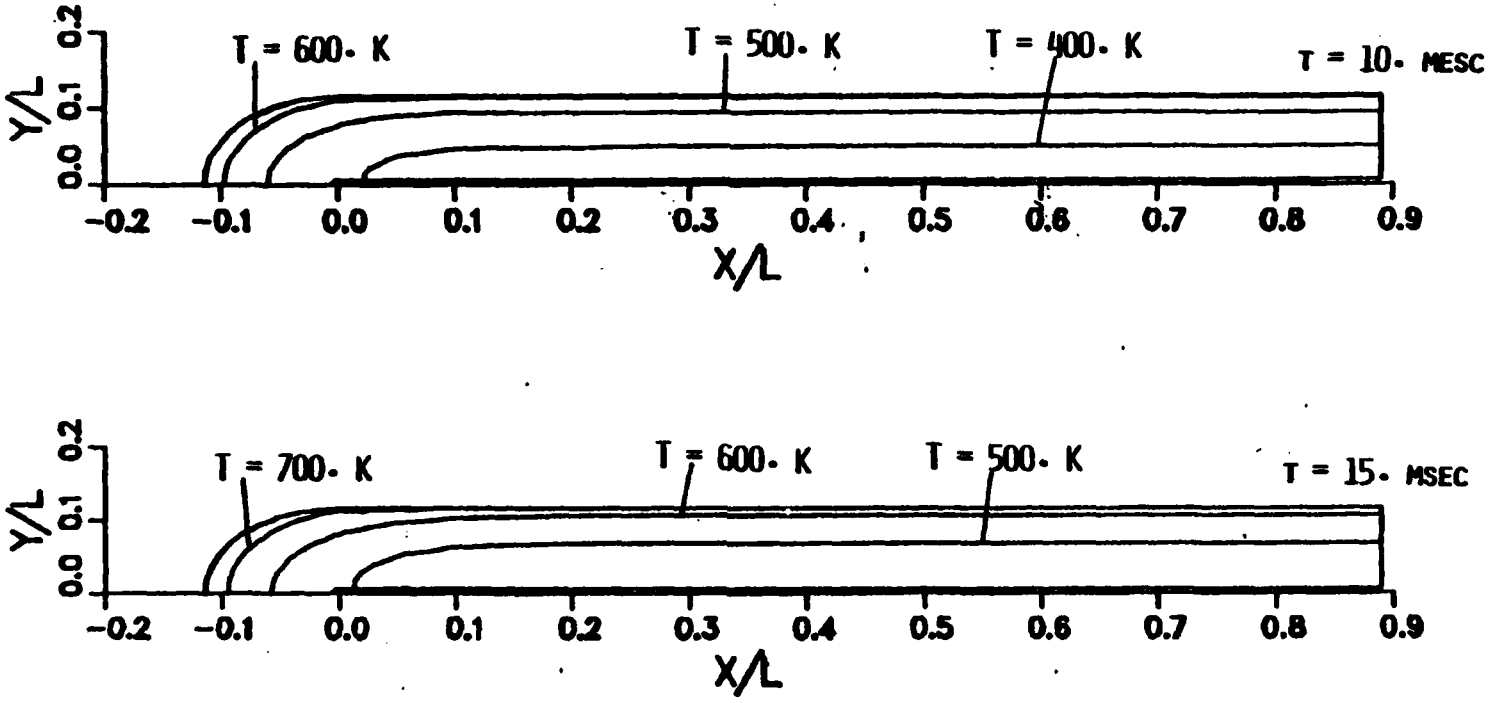

Figure 7. Inbore Temperatures Contours, Aluminum Fin with Hardcoating, T_{flame} = 3500. K

a. Section 1, Case ID 10

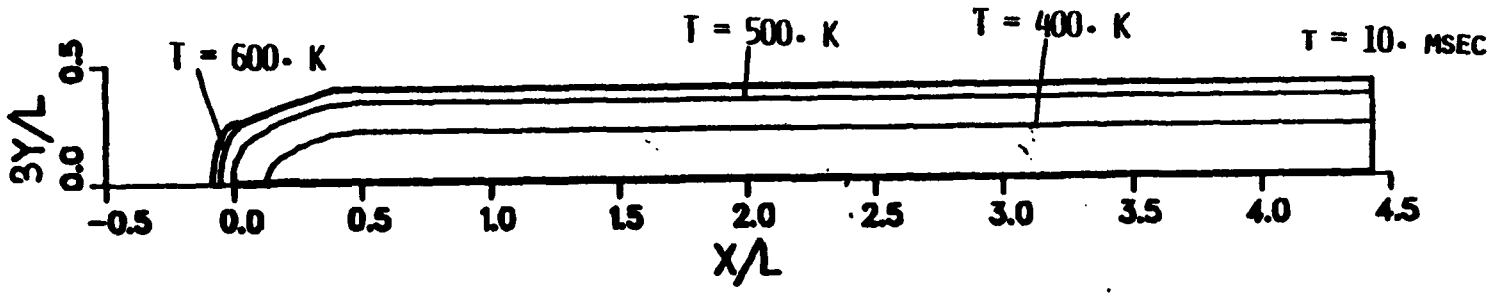

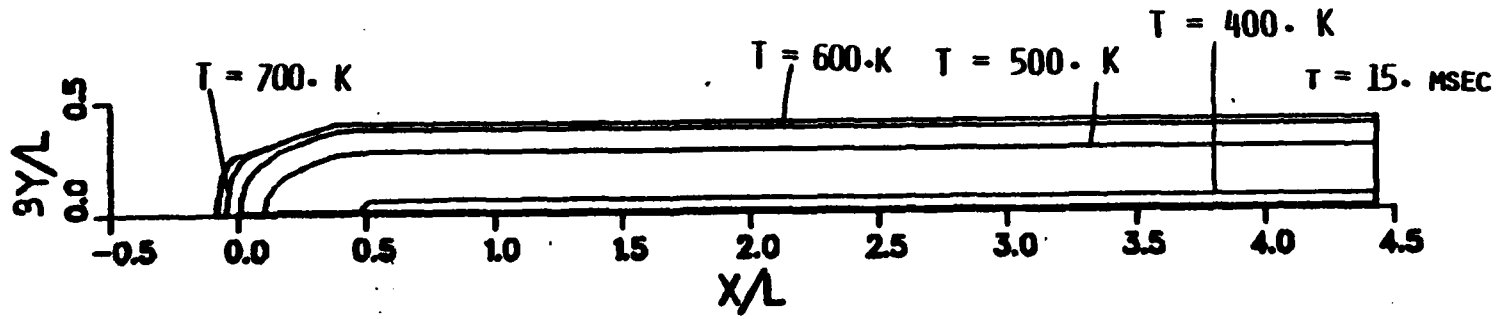

Figure 7. Continued

b. Section 2, Case ID 11

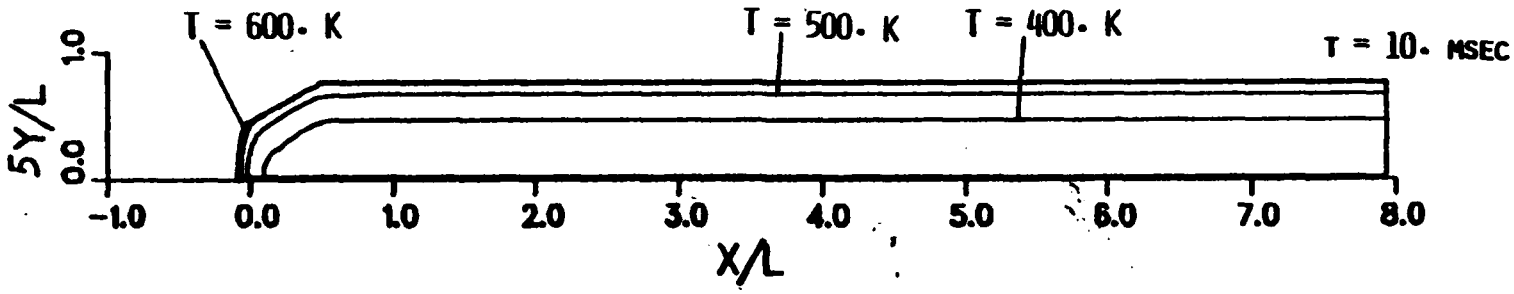

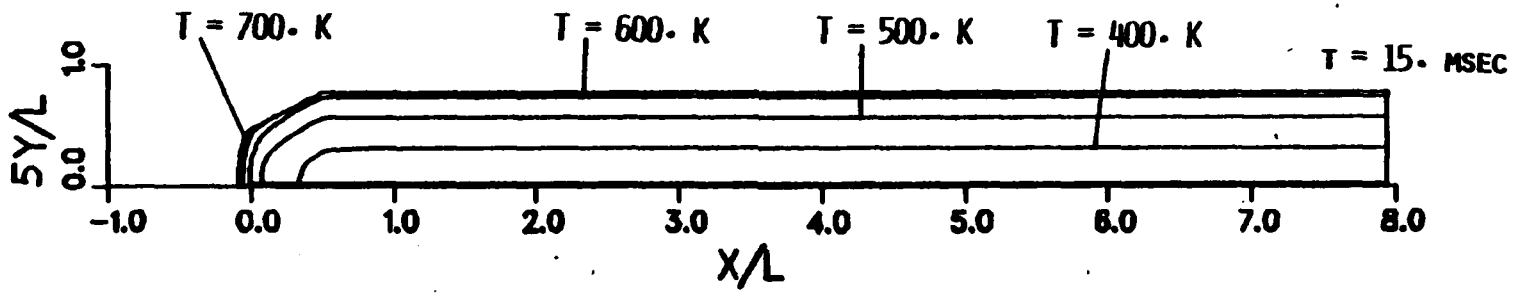

Figure 7. Continued

c. Section 3, Case ID 12

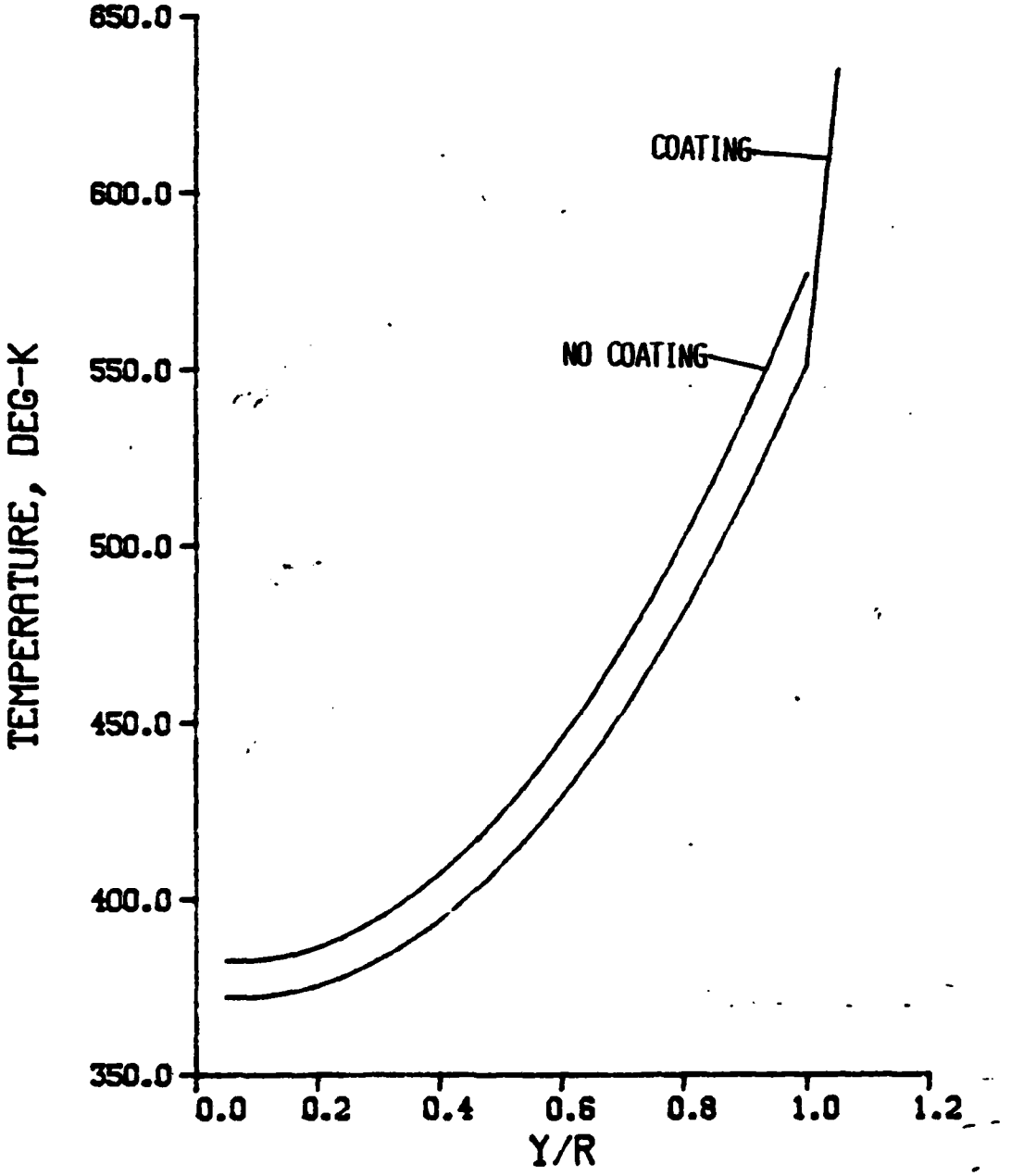

Figure 8. Temperature Profile Across Fin at Midchord, Aluminum Fin with/without Hardcoating, Section 1, T_{flame} = 3500. K, Case ID 4, 10

a. t = 10. milliseconds

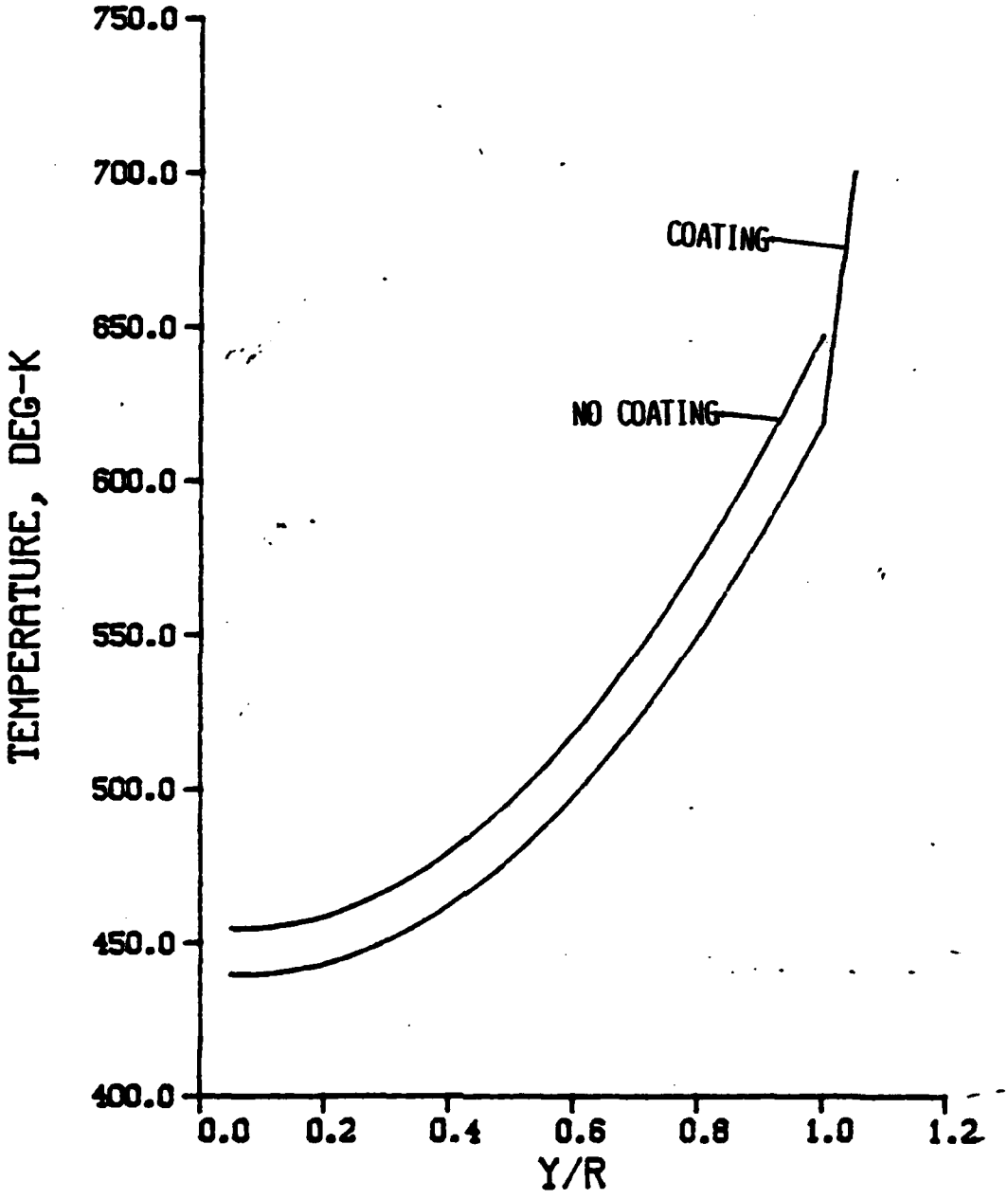

Figure 8. Continued

b. t = 15. milliseconds

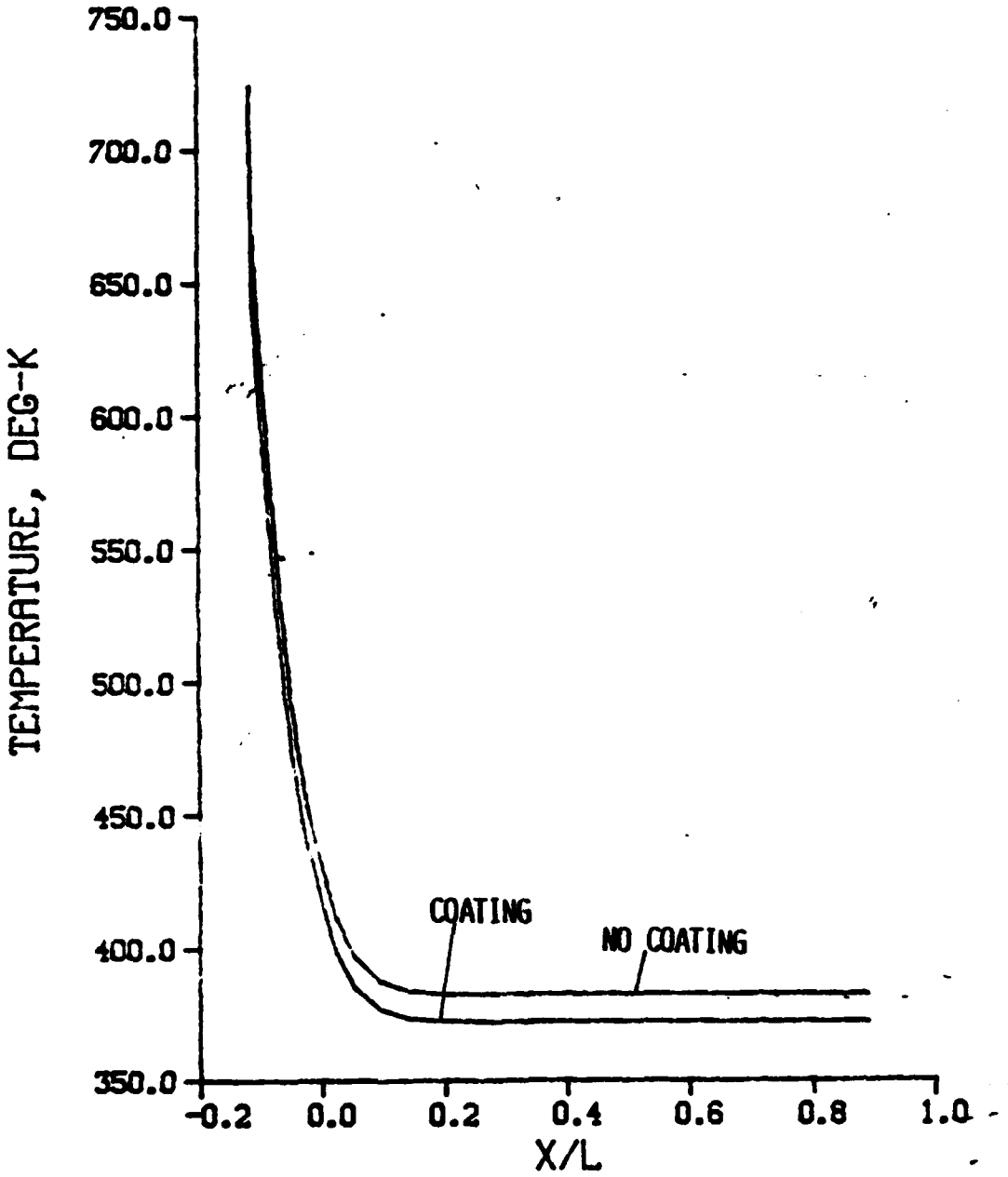

Figure 9. Temperature Along Fin Centerline, Aluminum Fin with/without Hardcoating, Section 1, T_{flame} = 3500. K, Case ID 4, 10

a. t = 10. milliseconds

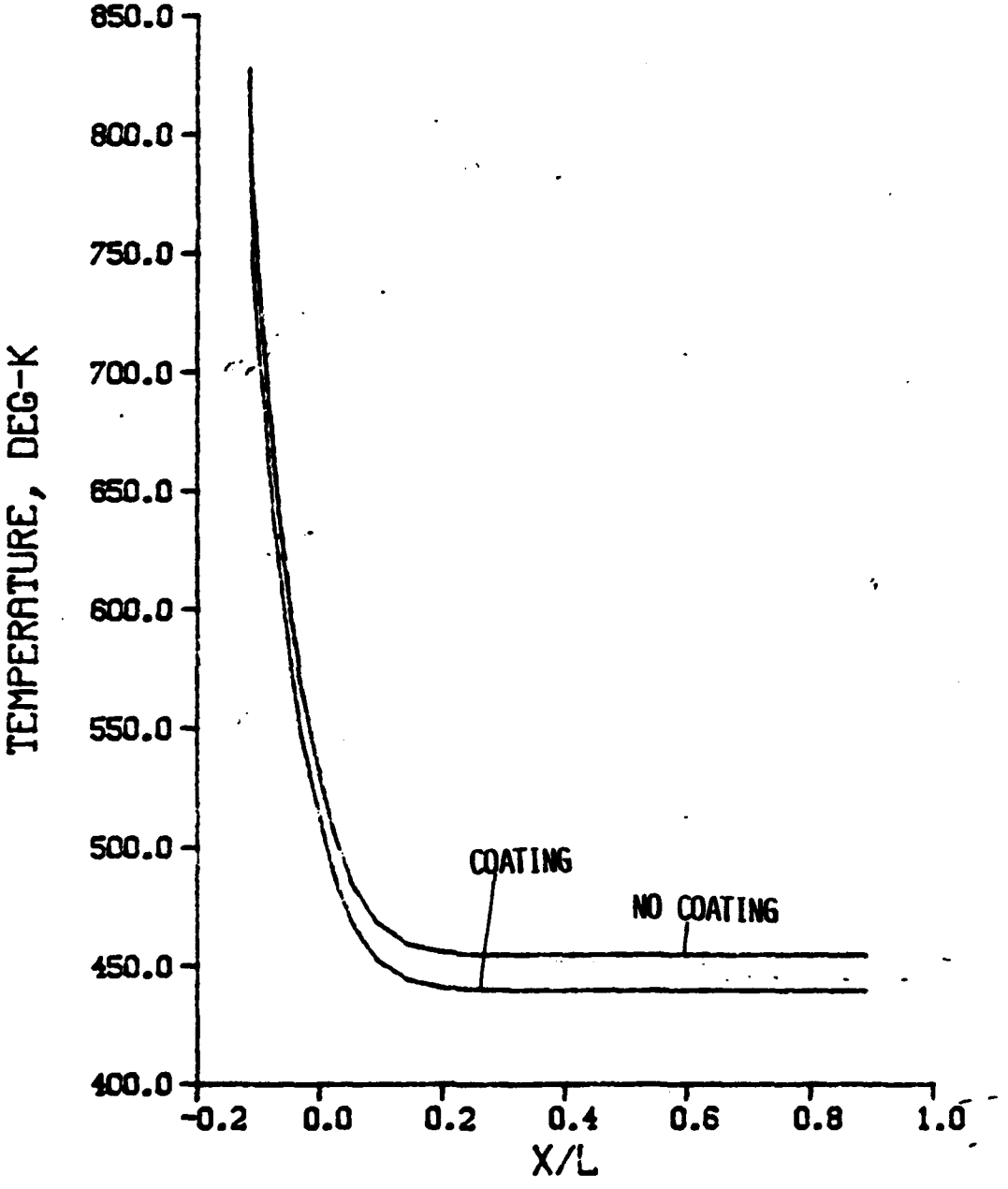

Figure 9. Continued

b. t = 15. milliseconds

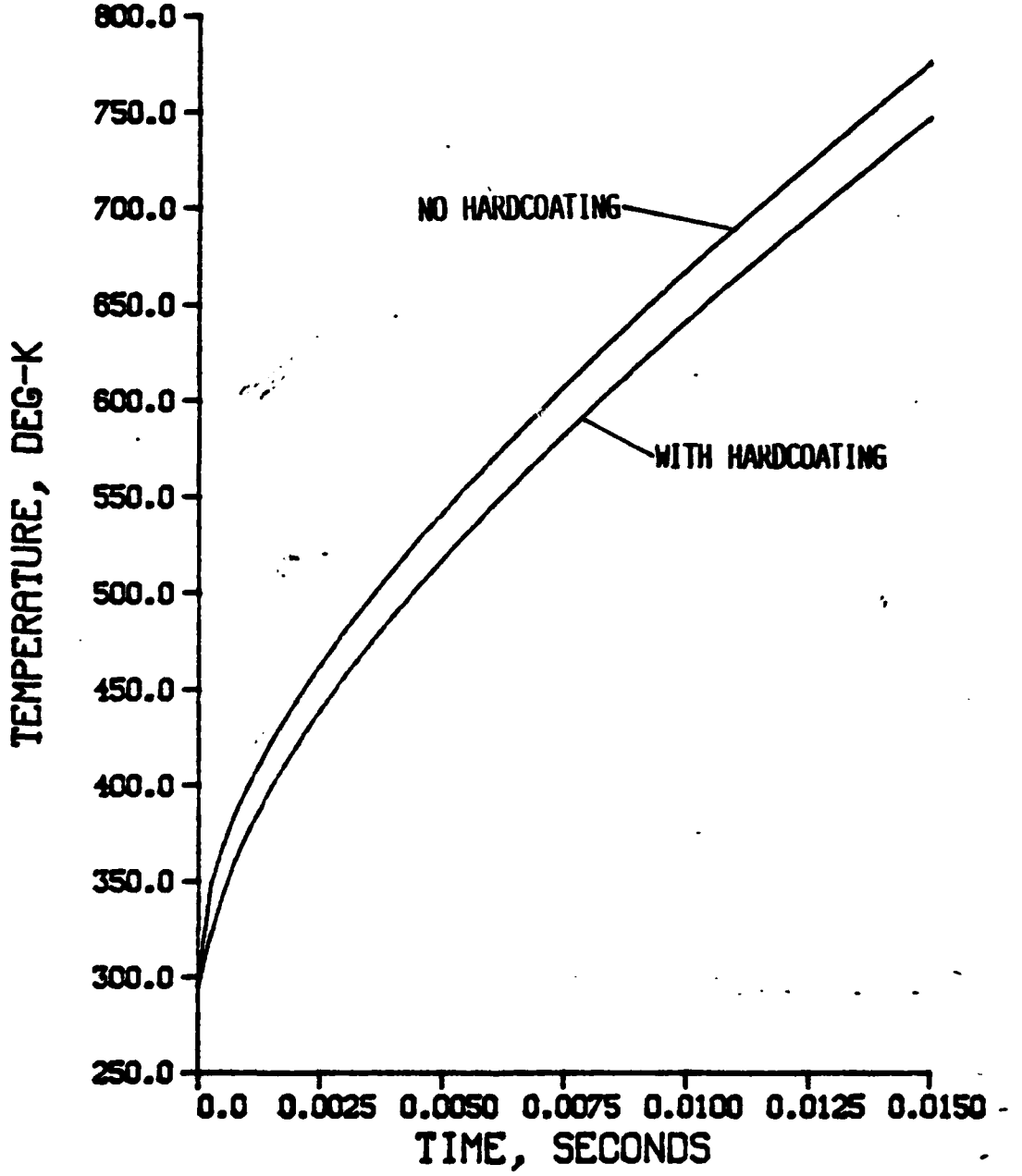

Figure 10. Temperature on Aluminum Surface at Leading Edge versus Time, Aluminum Fin with/without Hardcoating, Section 1, T_{flame} = 3500. K, Case ID 4, 10

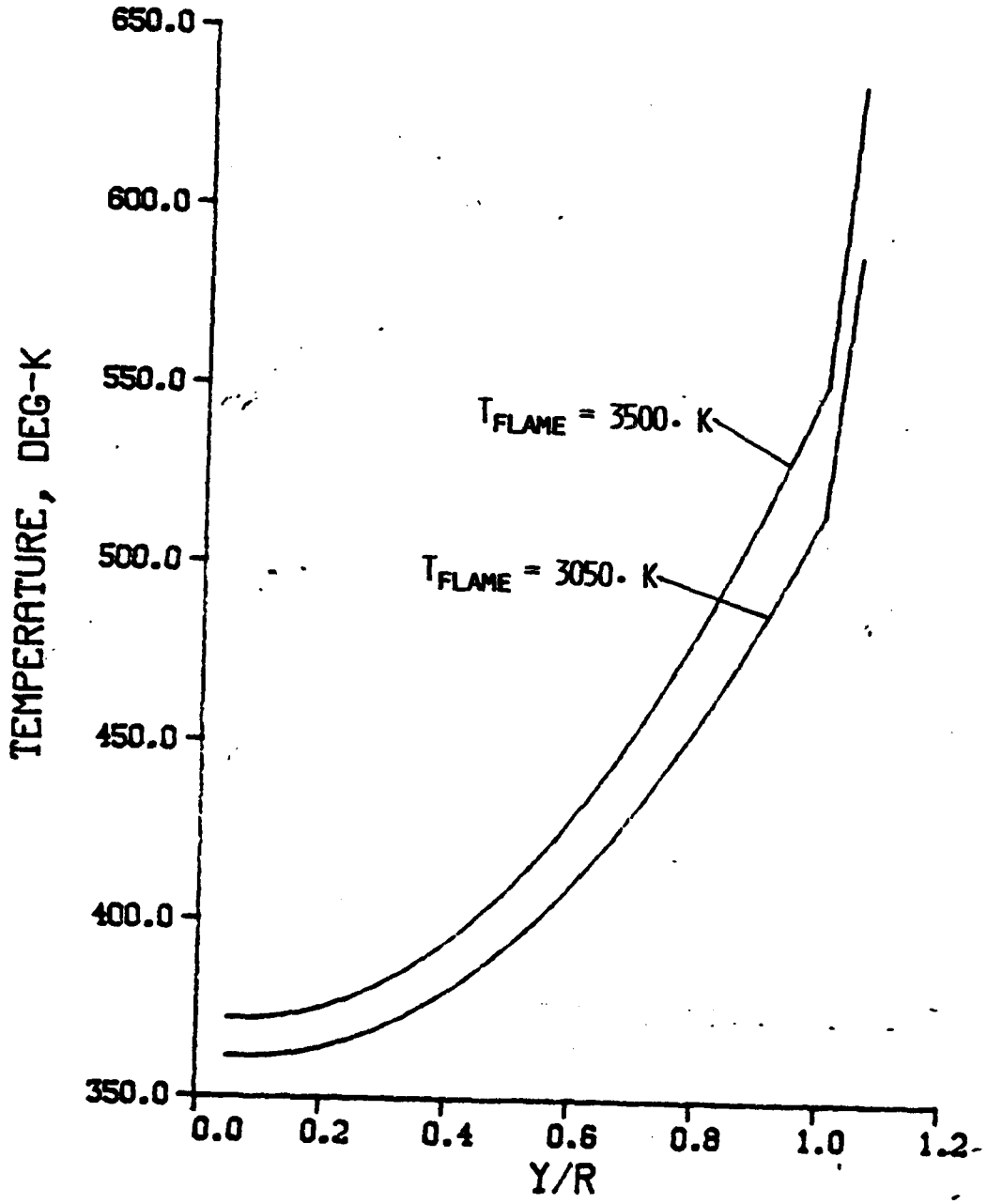

Figure 11. Temperature Profile Across Fin at Midchord, Aluminum Fin with Hardcoating, Section 1, Case ID 7, 10

a. t = 10. milliseconds

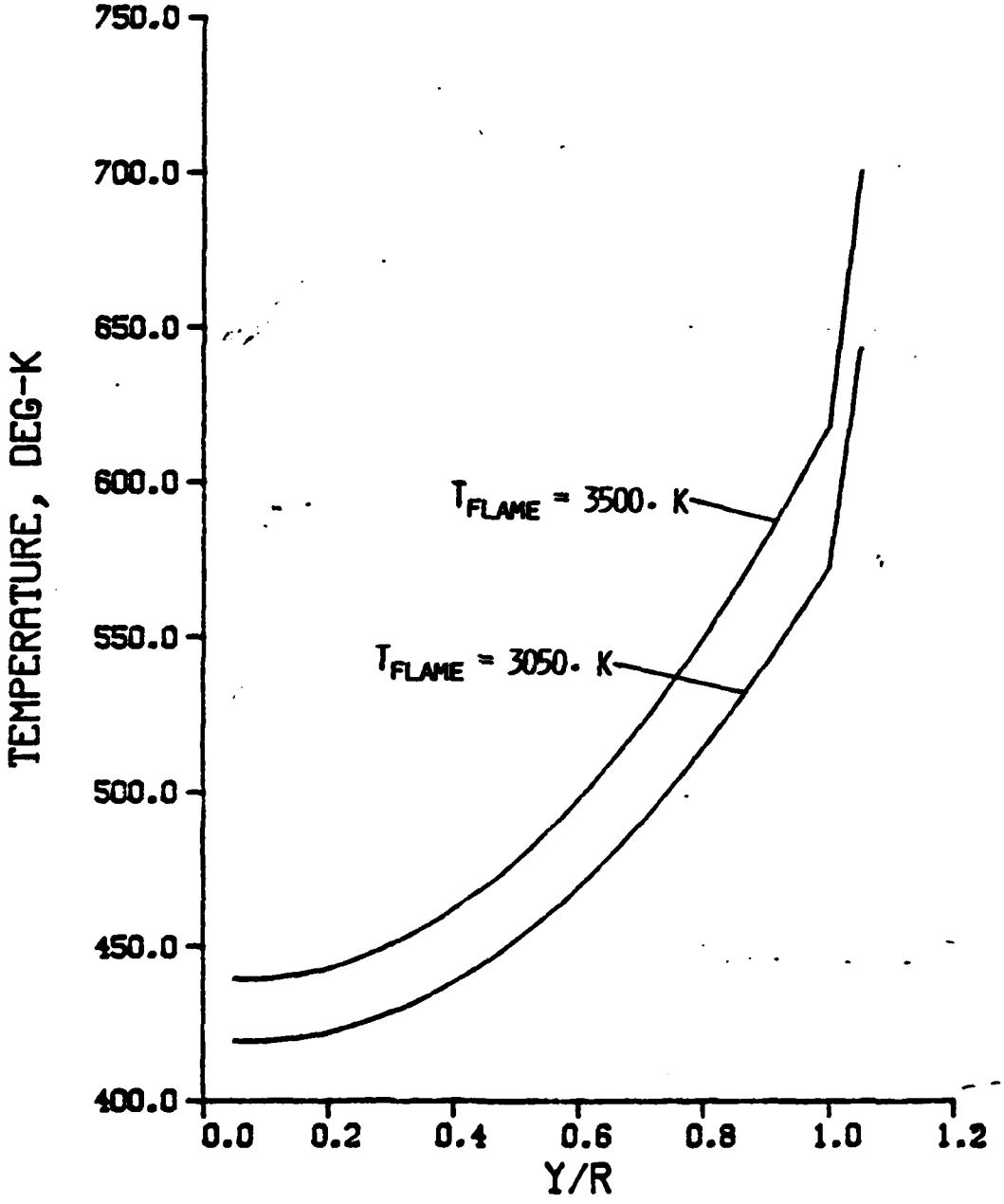

Figure 11. Continued

b. t = 15. milliseconds

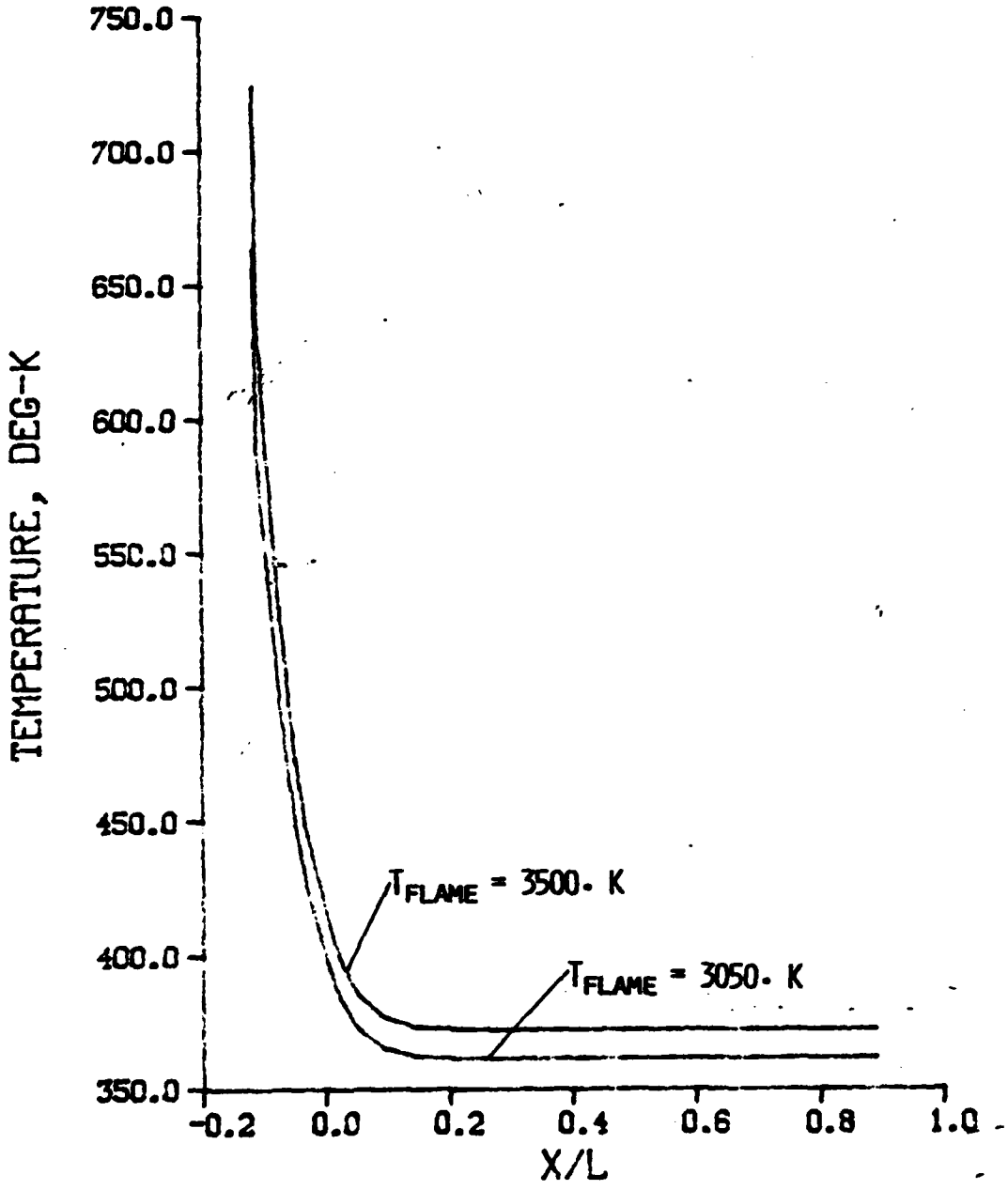

Figure 12. Temperature Along Fin Centerline, Aluminum Fin with Hardcoating, Section 1, Case ID 7, 10

a. t = 10. milliseconds

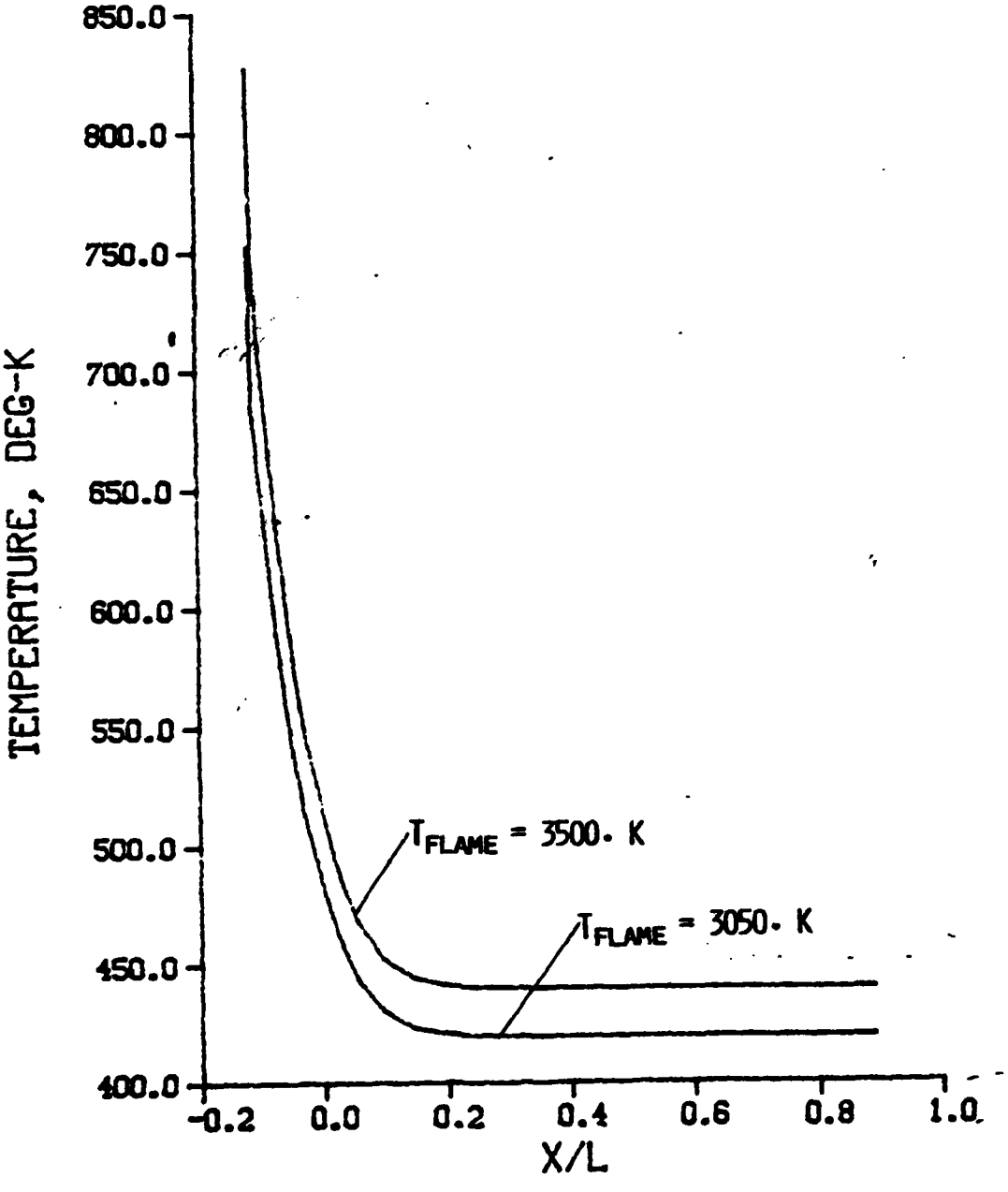

Figure 12. Continued

b. t = 15. milliseconds

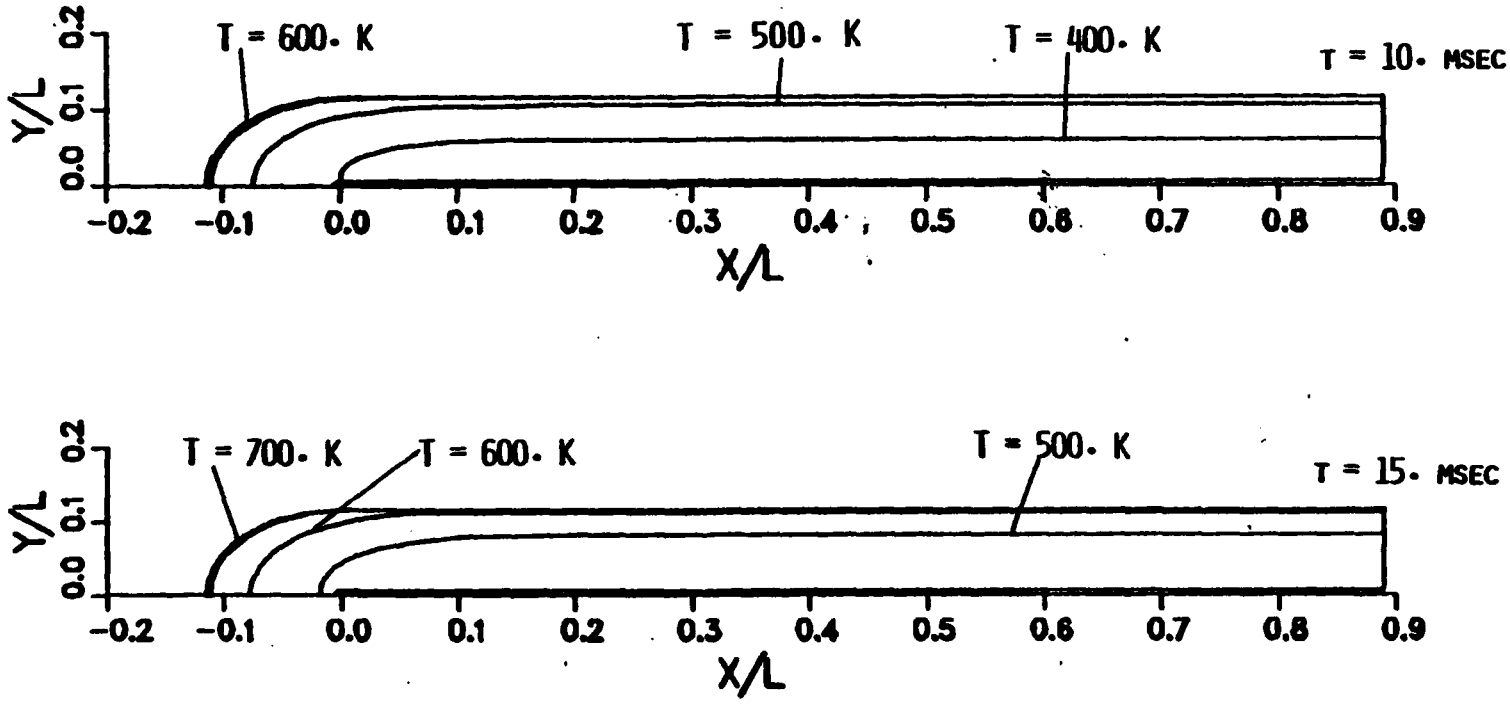

Figure 13. Inbore Temperature Contours, Aluminum Fin with Hardcoating, Section 1, T_{flame} = 3050. K, Case ID 7

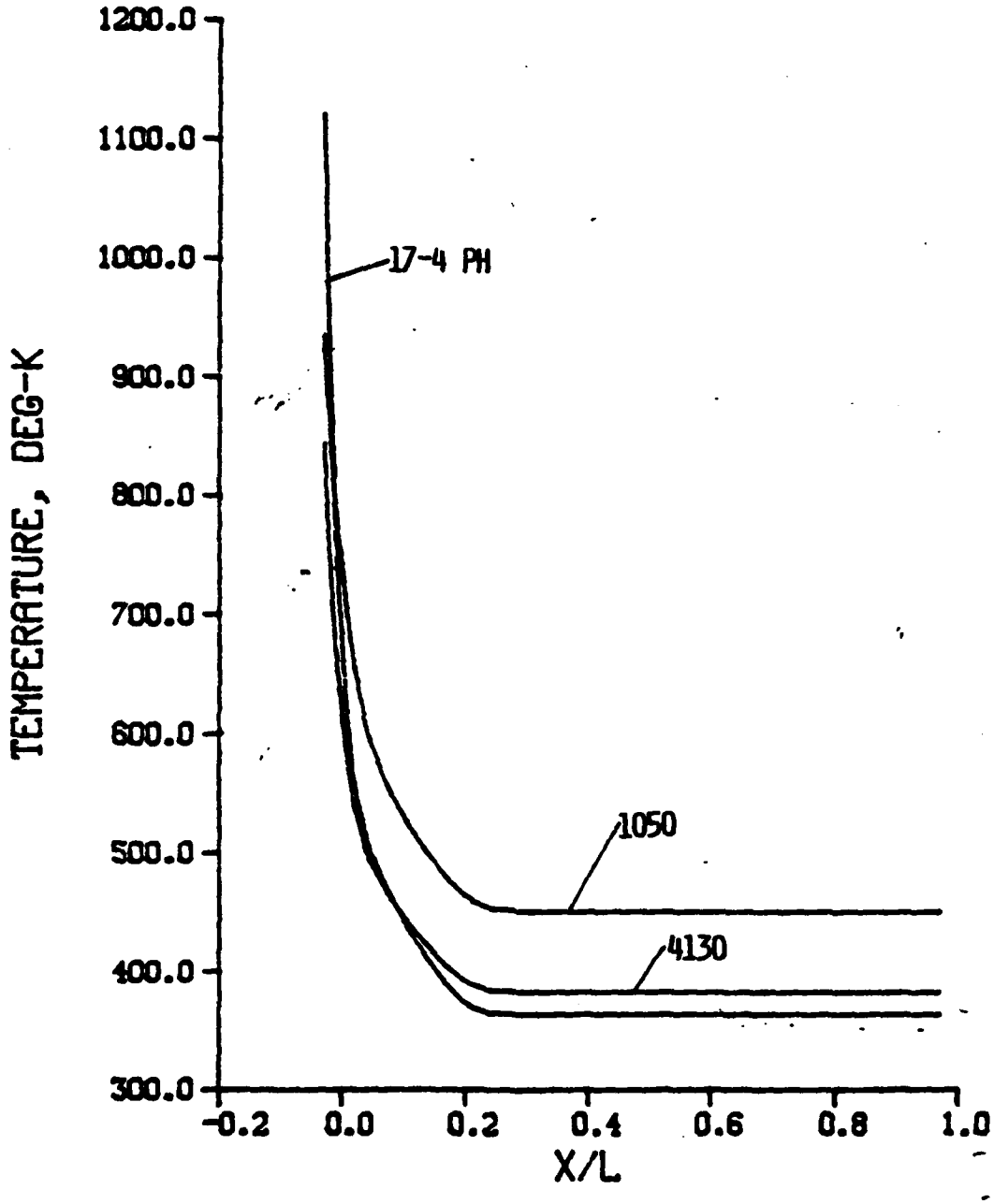

Figure 14. Temperature Along Fin Centerline, Steel Fins, Section 1, T_{flame} = 3500. K, Case ID 13, 16, 19

a. t = 10. milliseconds

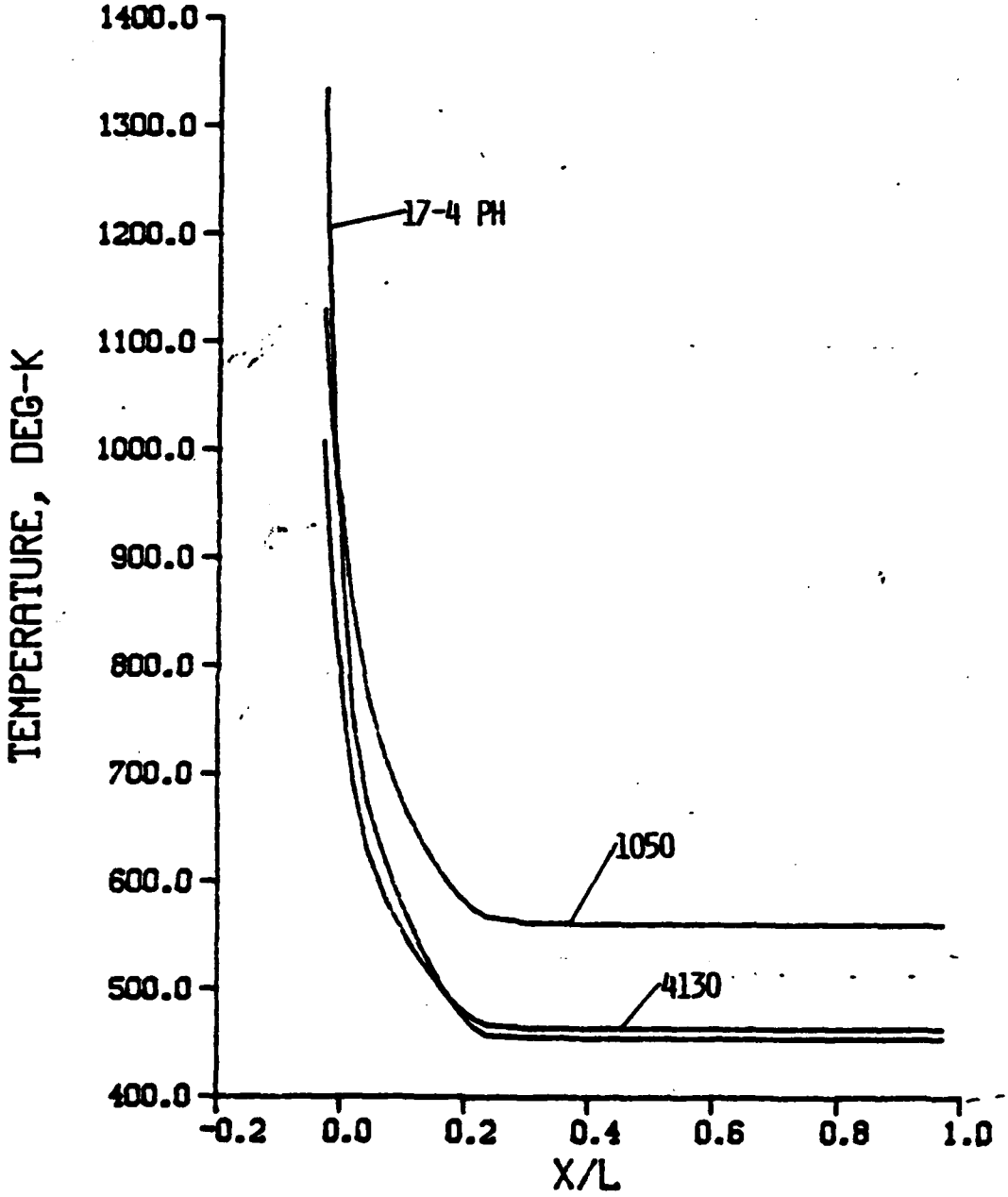

Figure 14. Continued

b. t = 15. milliseconds

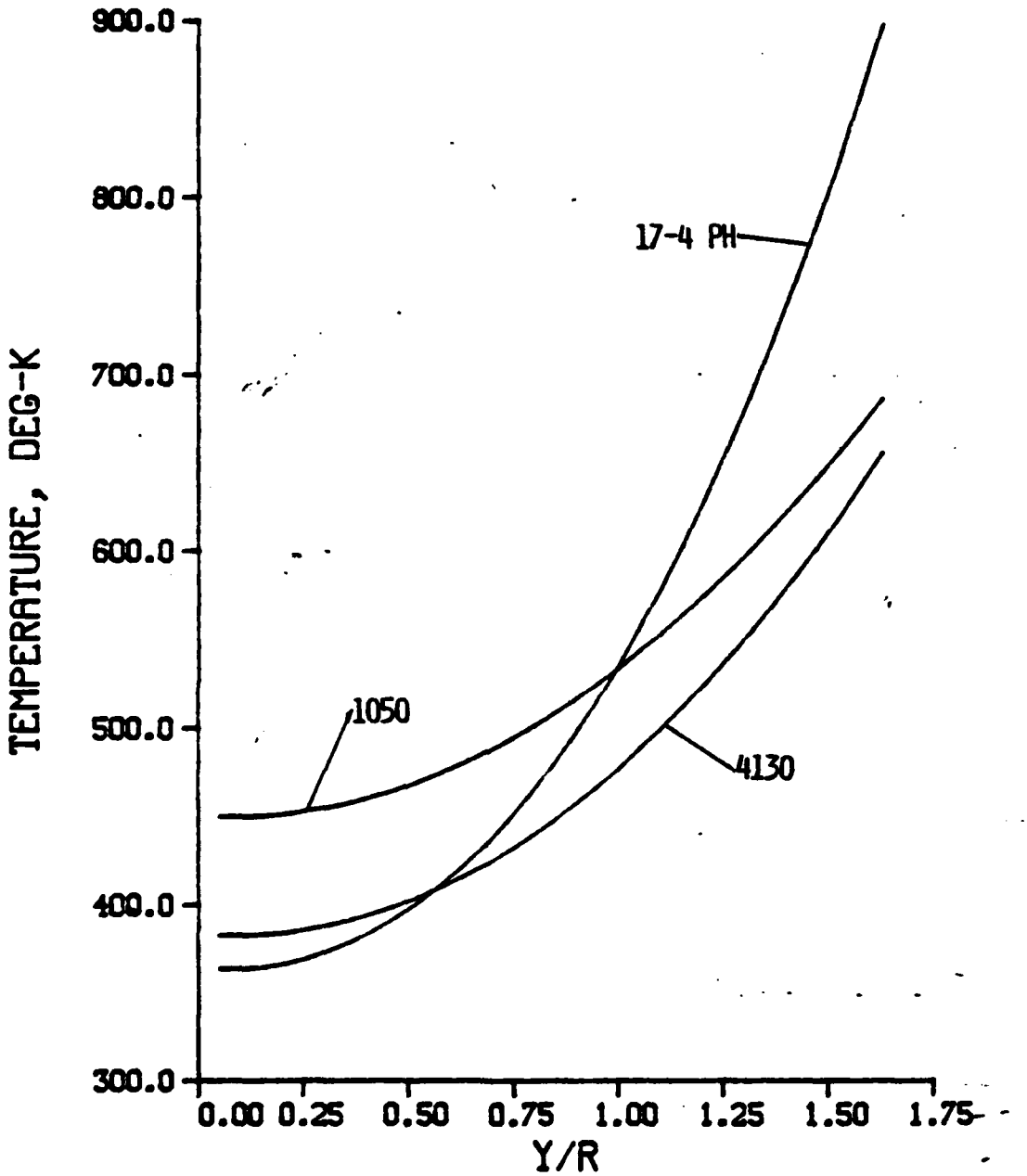

Figure 15. Temperature Profile Across Fin at Midchord, Steel Fins, Section 1, T_{flame} = 3500. K, Case ID 13, 16, 19

a. t = 10. milliseconds

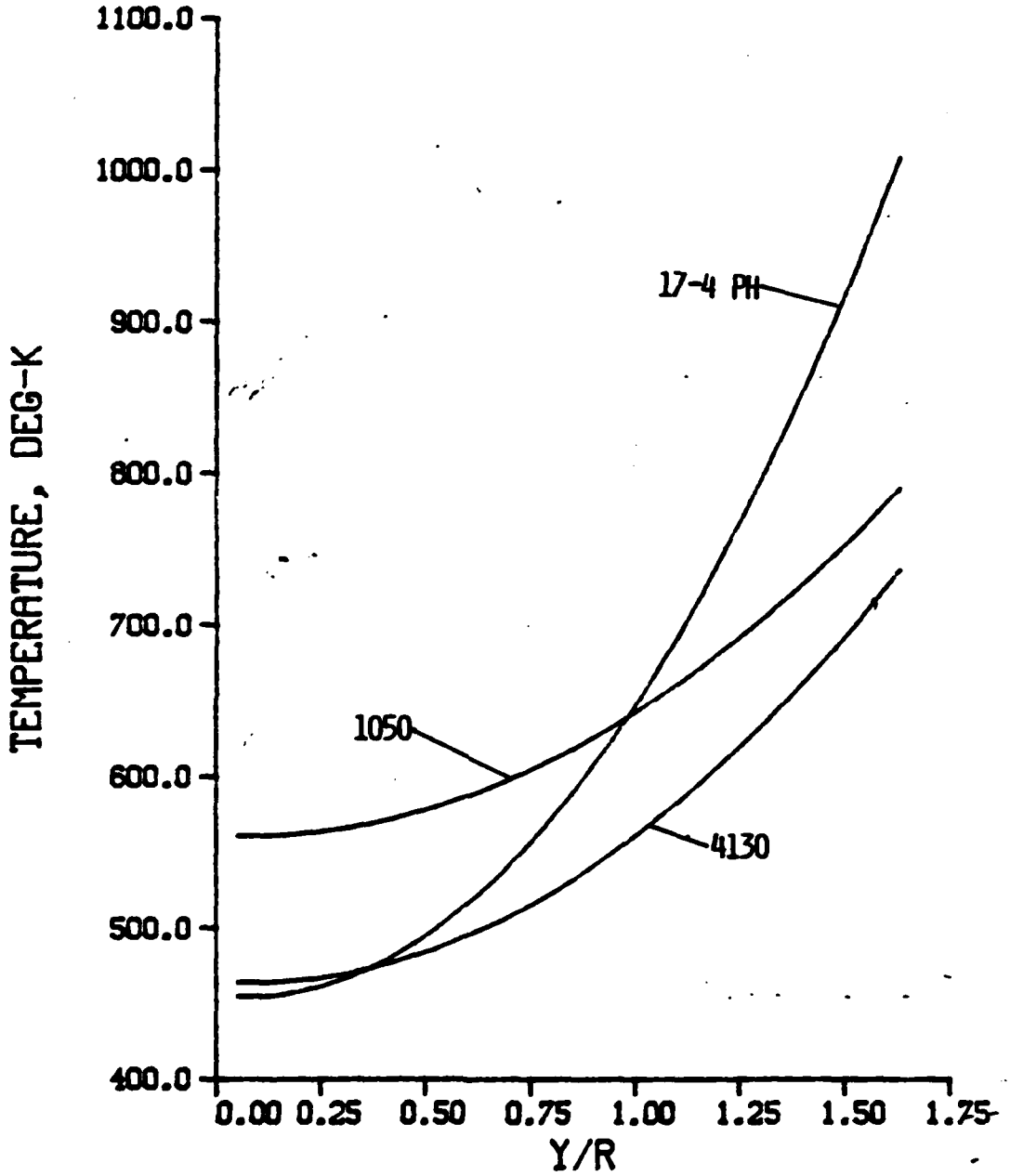

Figure 15. Continued

b. t = 15. milliseconds

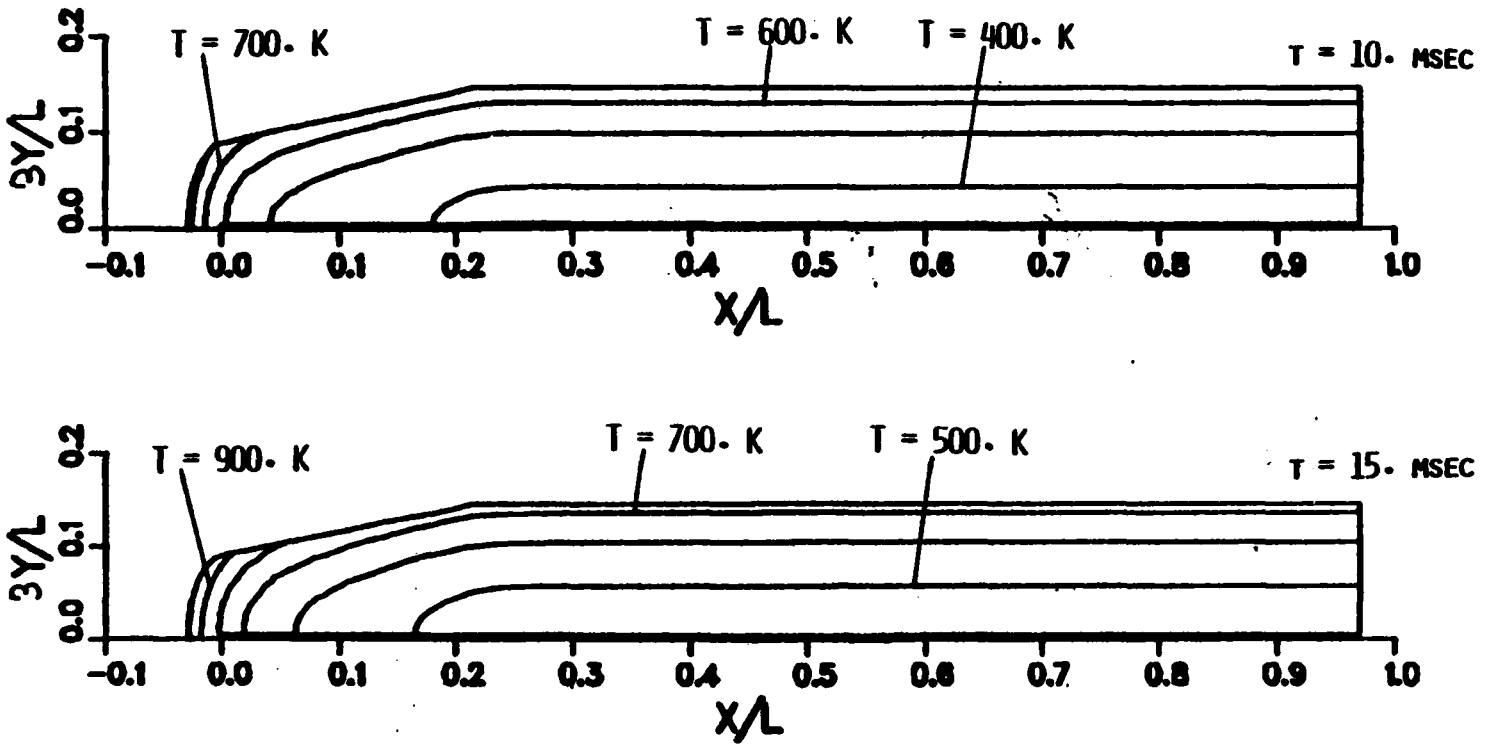

Figure 16. Inbore Temperature Contours, 4130 Steel Fin, T_{flame} = 3500. K

a. Section 1, Case ID 19

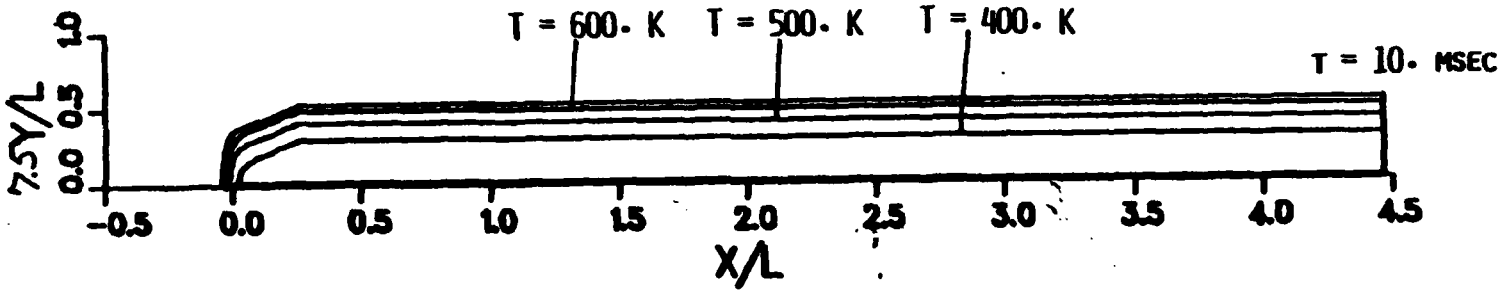

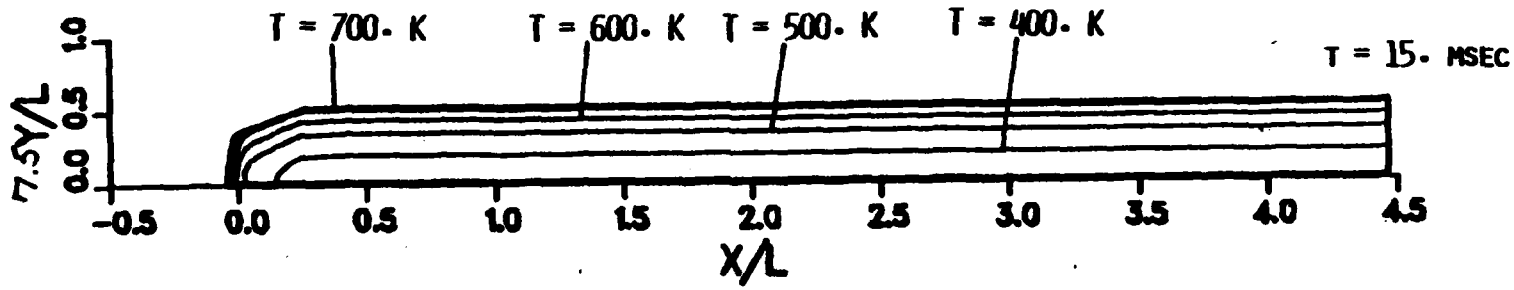

Figure 16. Continued

b. Section 2, Case ID 20

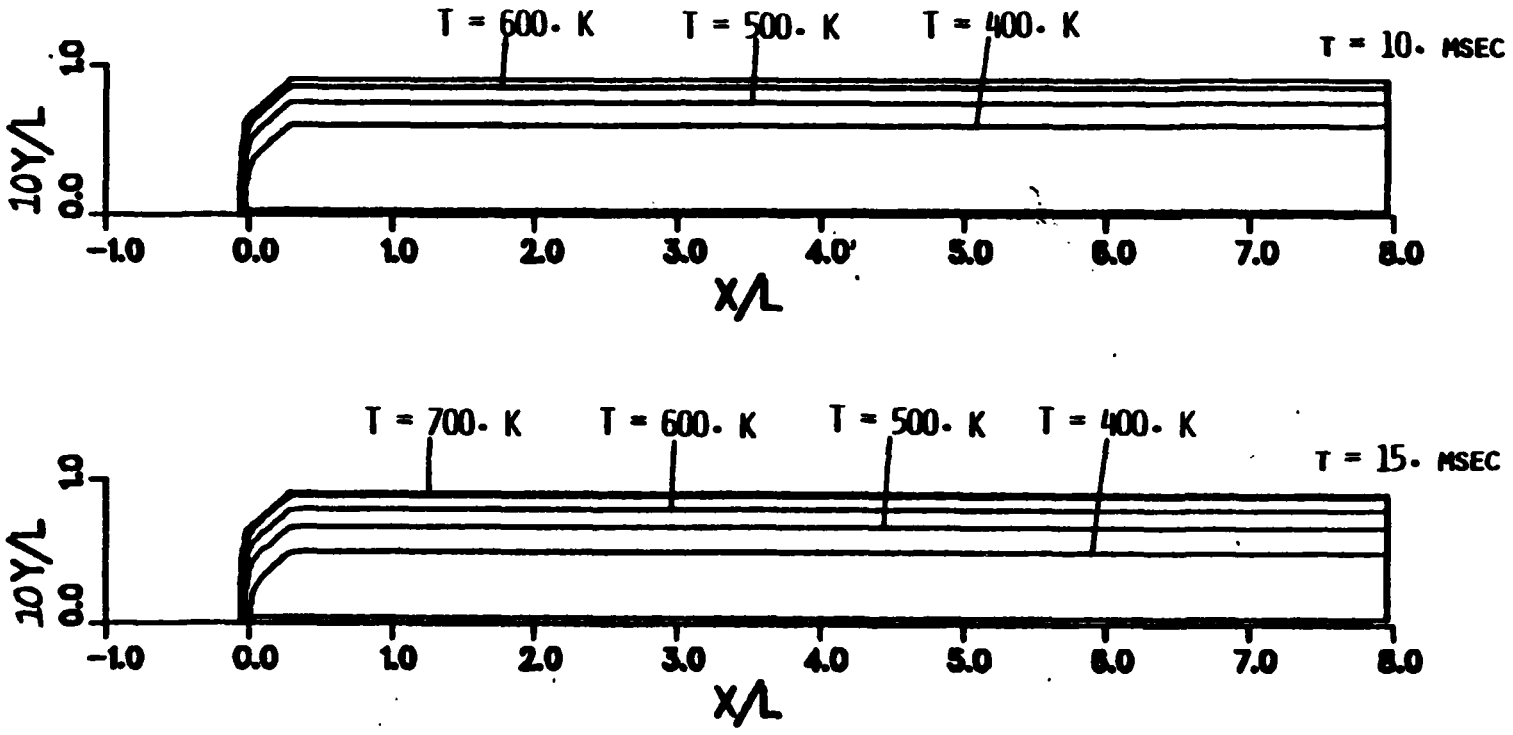

Figure 16. Continued

c. Section 3, Case ID 21

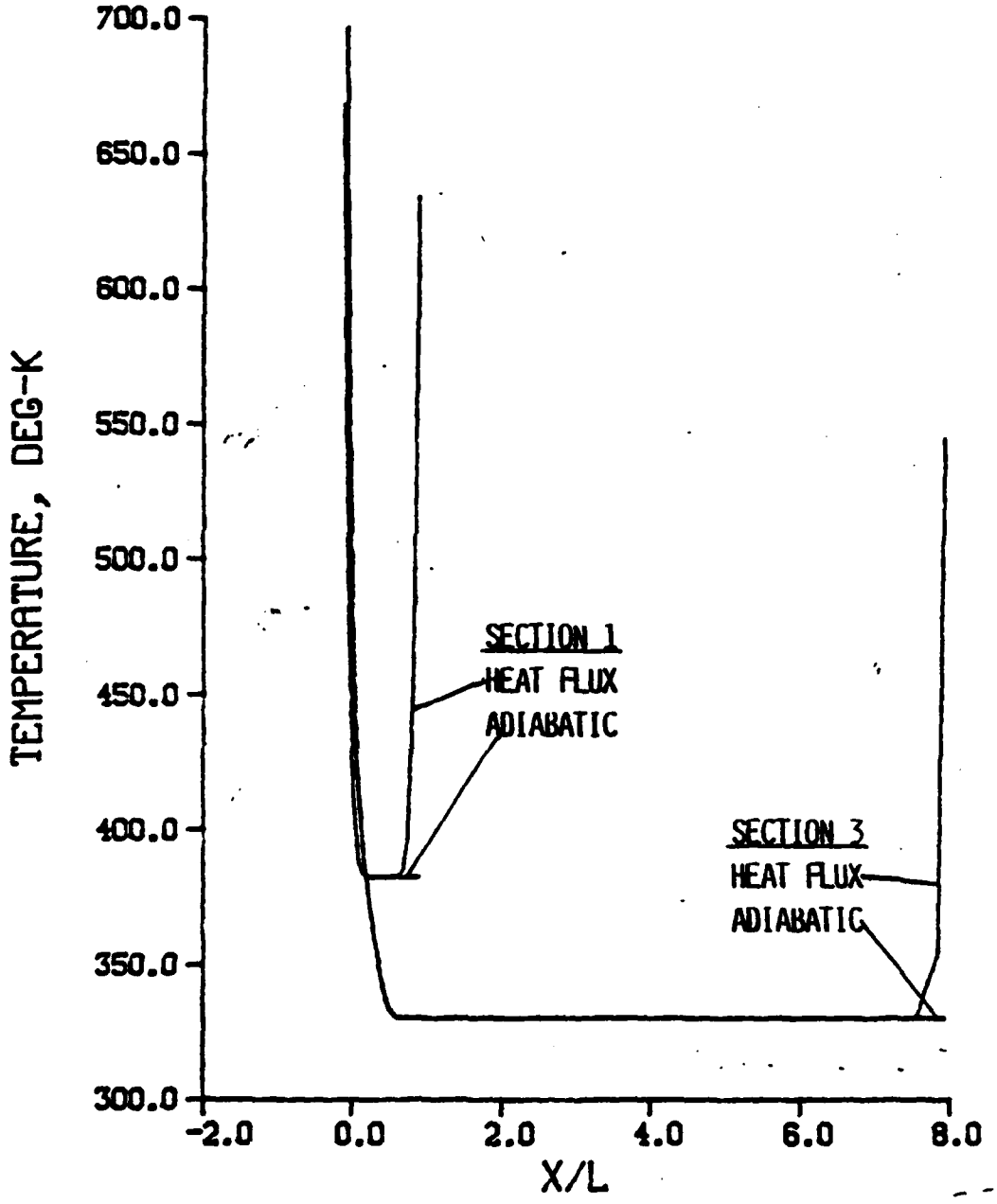

Figure 17. Temperature Along Fin Centerline, Aluminum Fin with No Hardcoat, T_{flame} = 3500. K, Sections 1, 3, Case ID 4, 6, 22, 24

a. t = 10. milliseconds

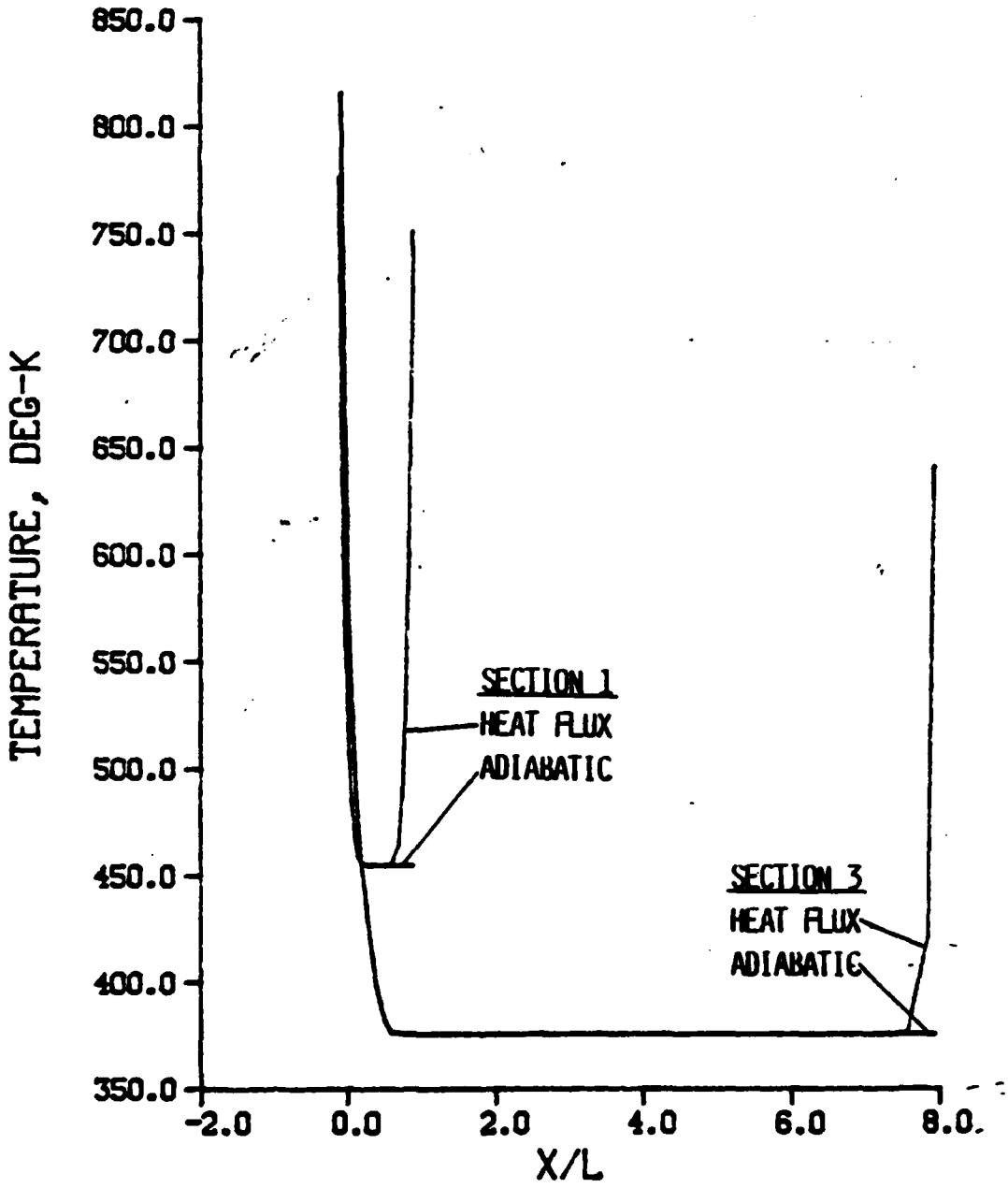

Figure 17. Continued

b. t = 15. milliseconds

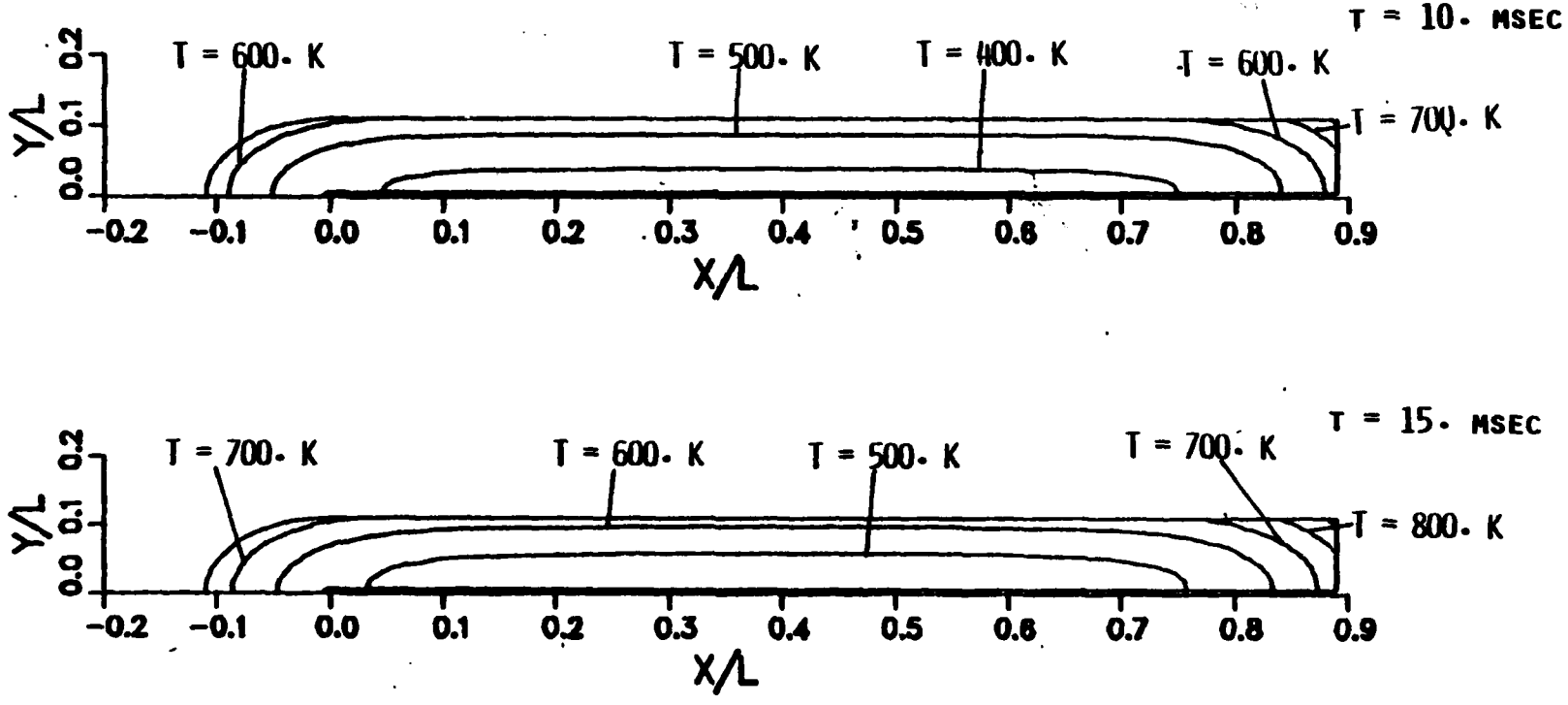

Figure 18. Inbore Temperature Contours, Aluminum Fin, No Hardcoat, Section 1, T_{flame} = 3500. K

a. Heat Flux Trailing Edge Boundary Condition, Case ID 25

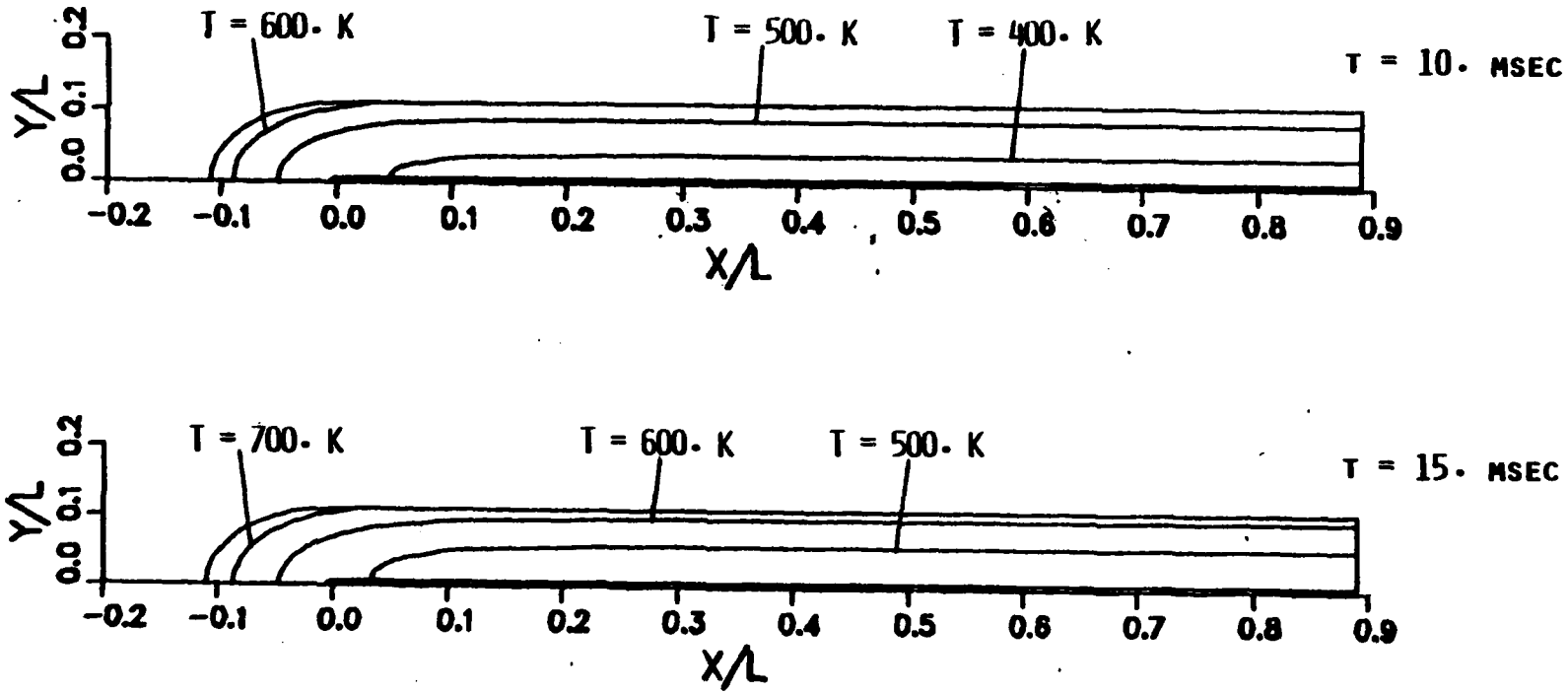

Figure 18. Continued

b. Adiabatic Trailing Edge Boundary Condition, Case ID 4

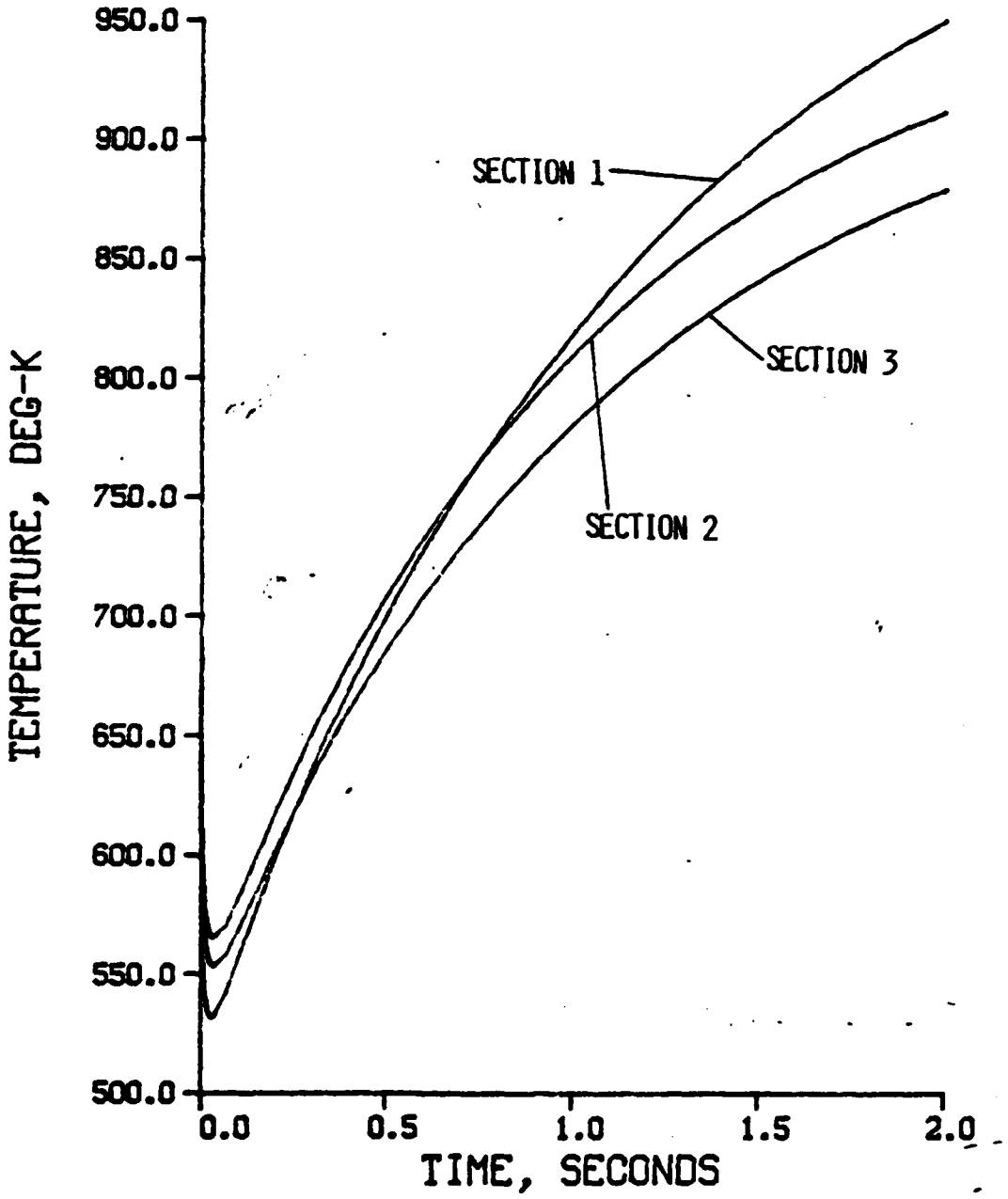

Figure 19. Temperature on Al/Al Oxide Interface at Leading Edge versus Time, Aluminum Fin with Hardcoating, Sections 1, 2, 3, T_{flame} = 3500. K, Case ID 10, 11, 12

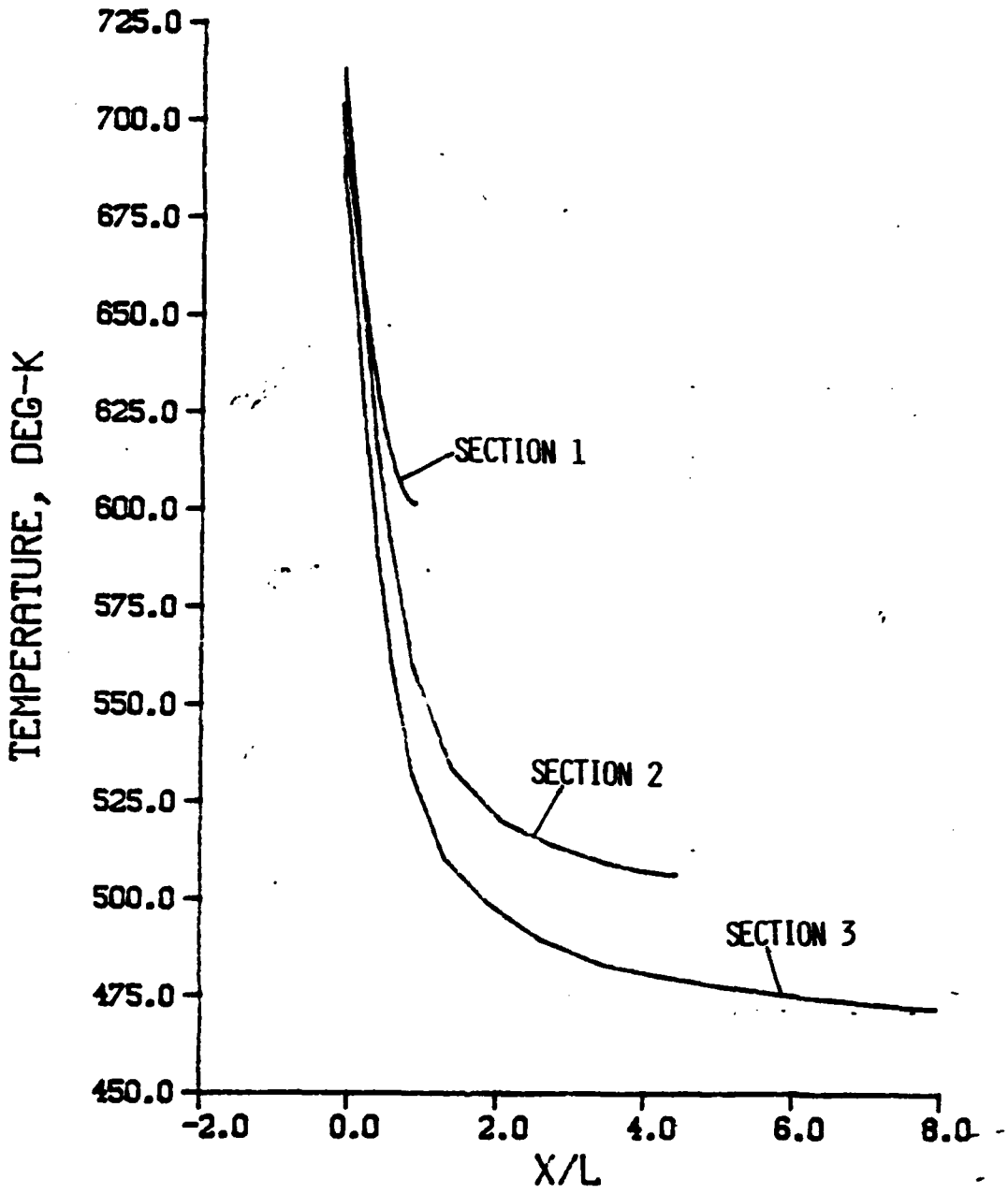

Figure 20. Temperature Along Fin Centerline, Aluminum Fin with Hardcoating, Sections 1, 2, 3, T_{flame} = 3500. K, Case ID 10, 11, 12

a. t = 0.5 seconds

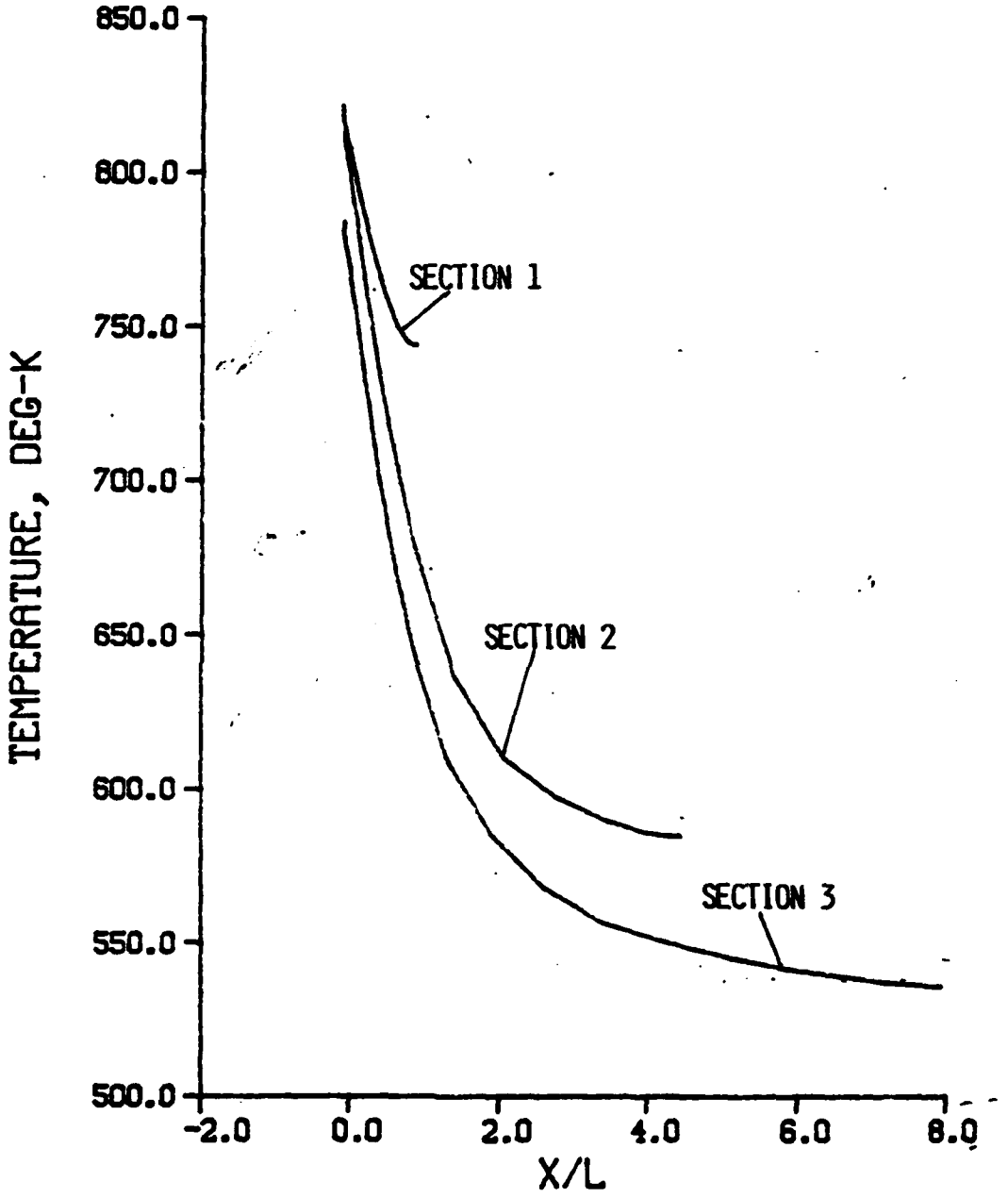

Figure 20. Continued

b. t = 1.0 seconds

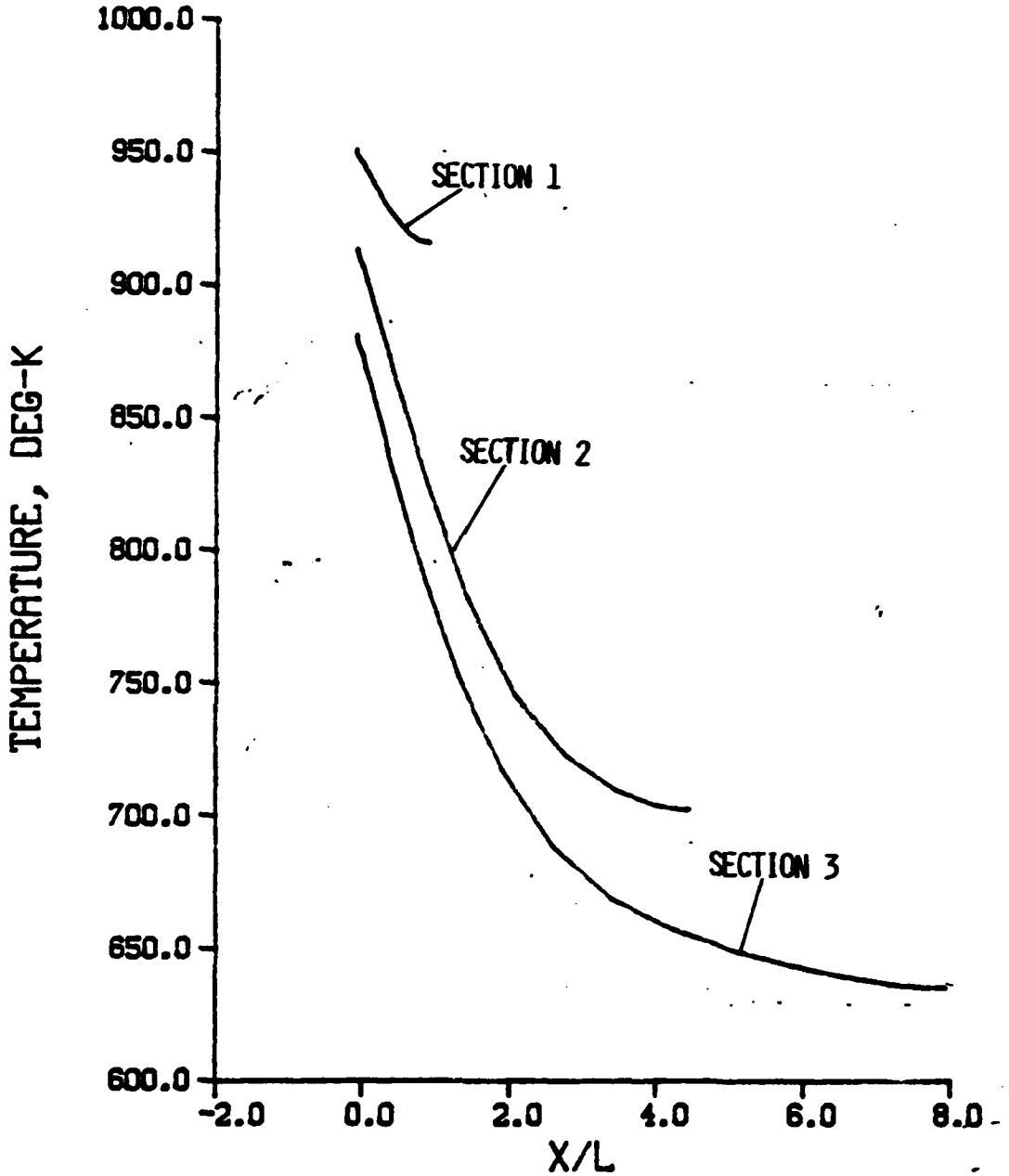

Figure 20. Continued

c. t = 2.0 seconds

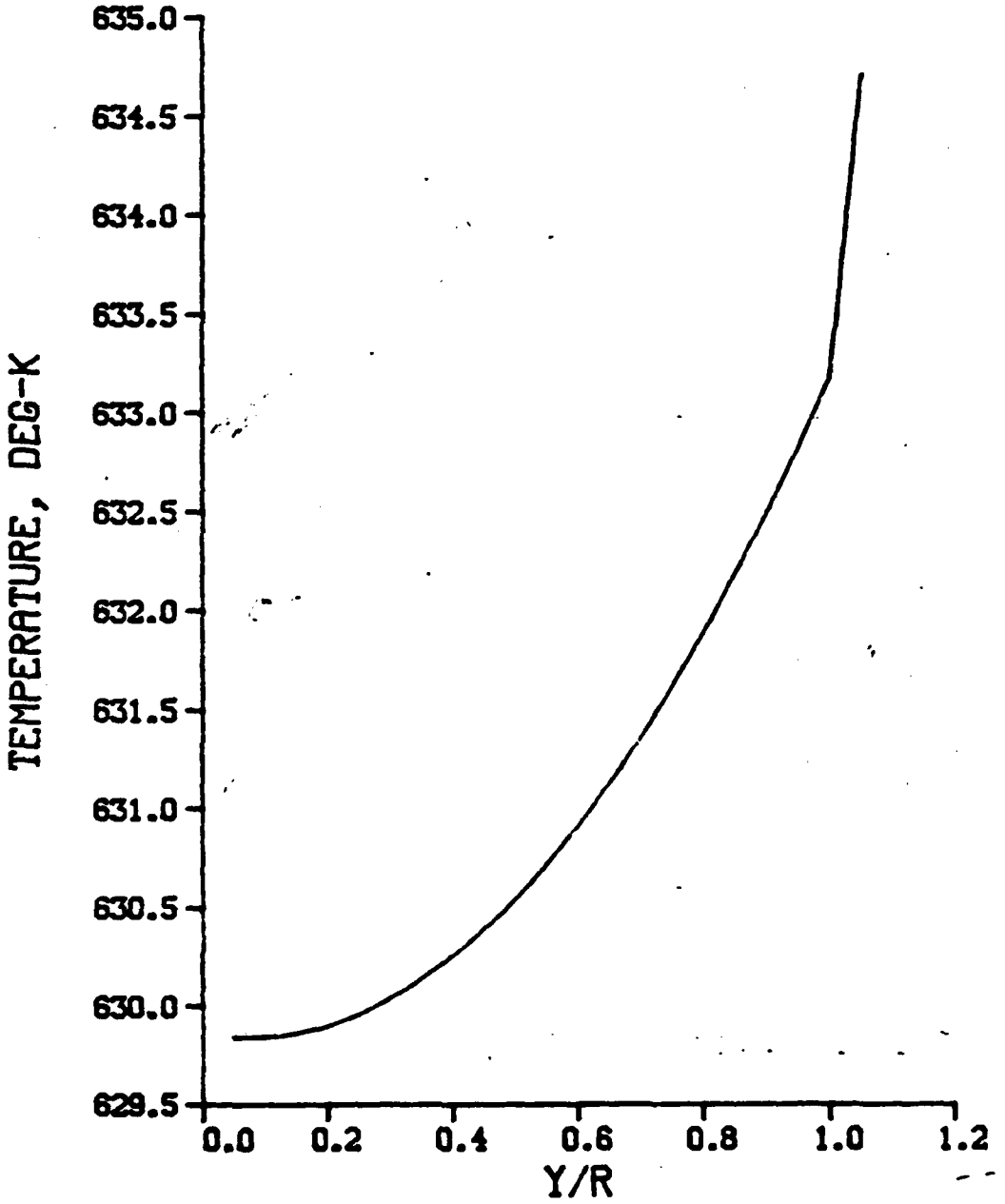

Figure 21. Temperature Profile Across Fin at Midchord, Aluminum Fin with Hardcoating, Section 1, T_{flame} = 3500. K, Case ID 10

a. t = 0.5 seconds

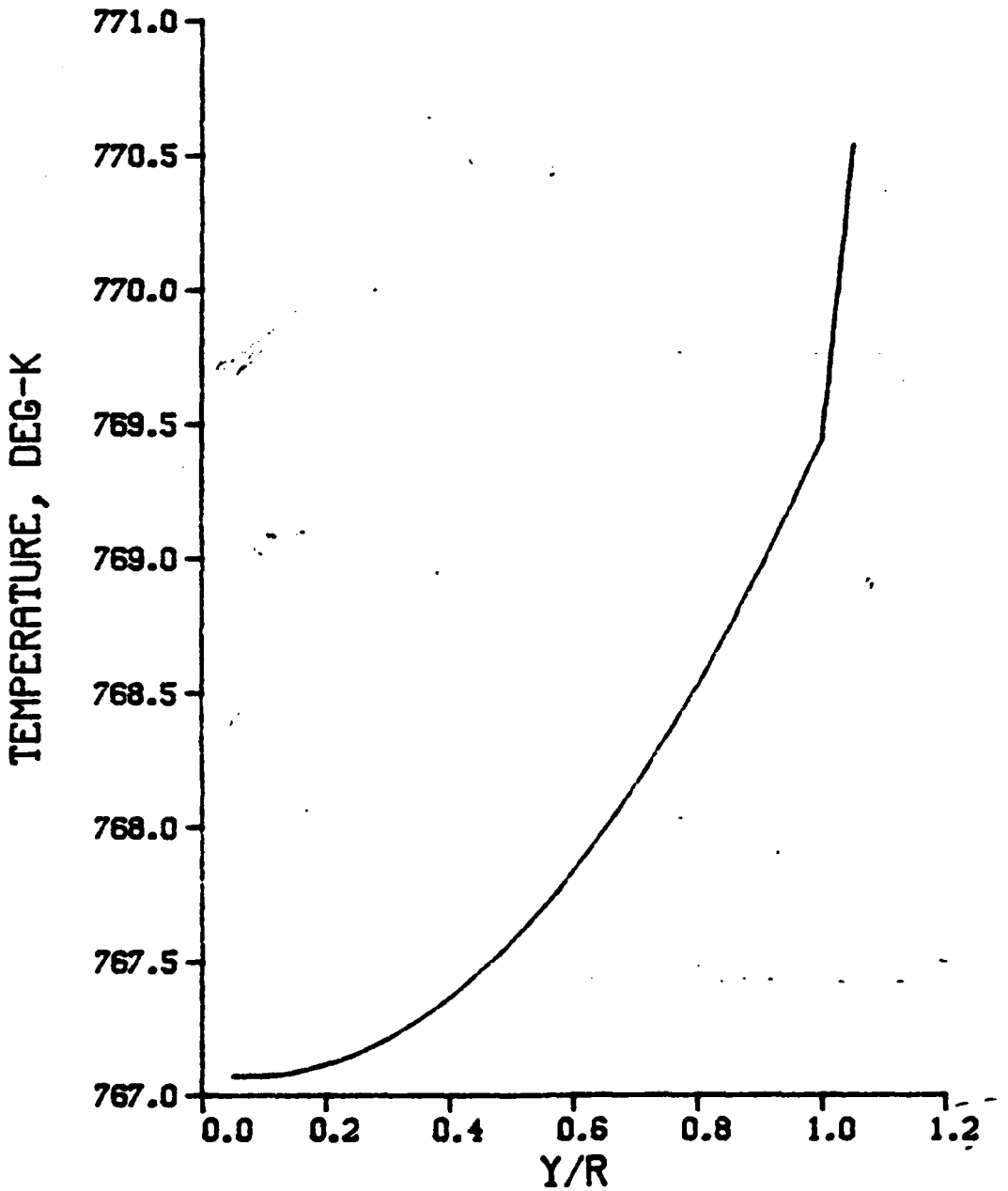

Figure 21. Continued

b. t = 1.0 seconds

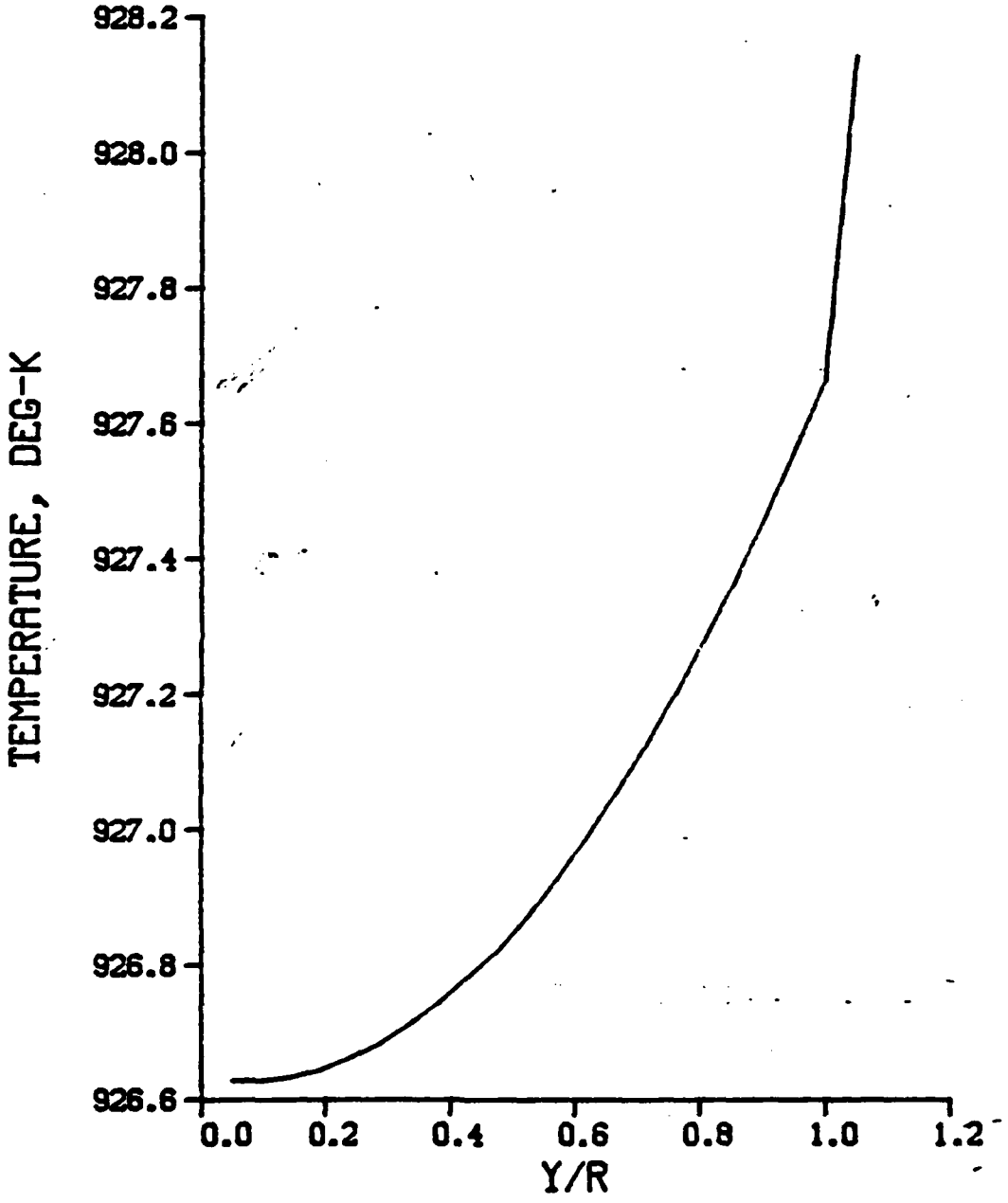

Figure 21. Continued

c. t = 2.0 seconds

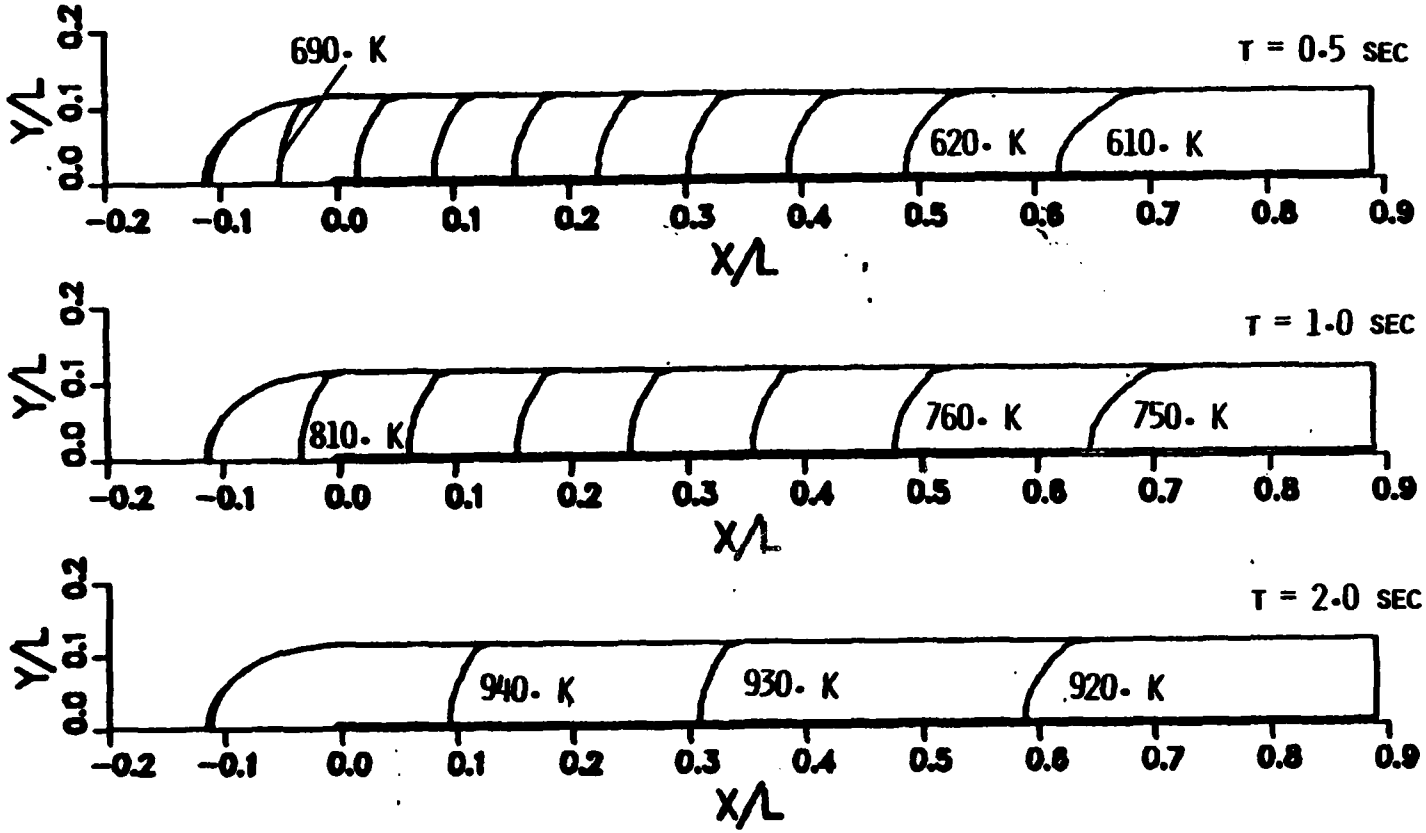

Figure 22. Inflight Temperature Contours, Aluminum Fin with Hardcoating, T_{flame} = 3500. K

a. Section 1, Case ID 10

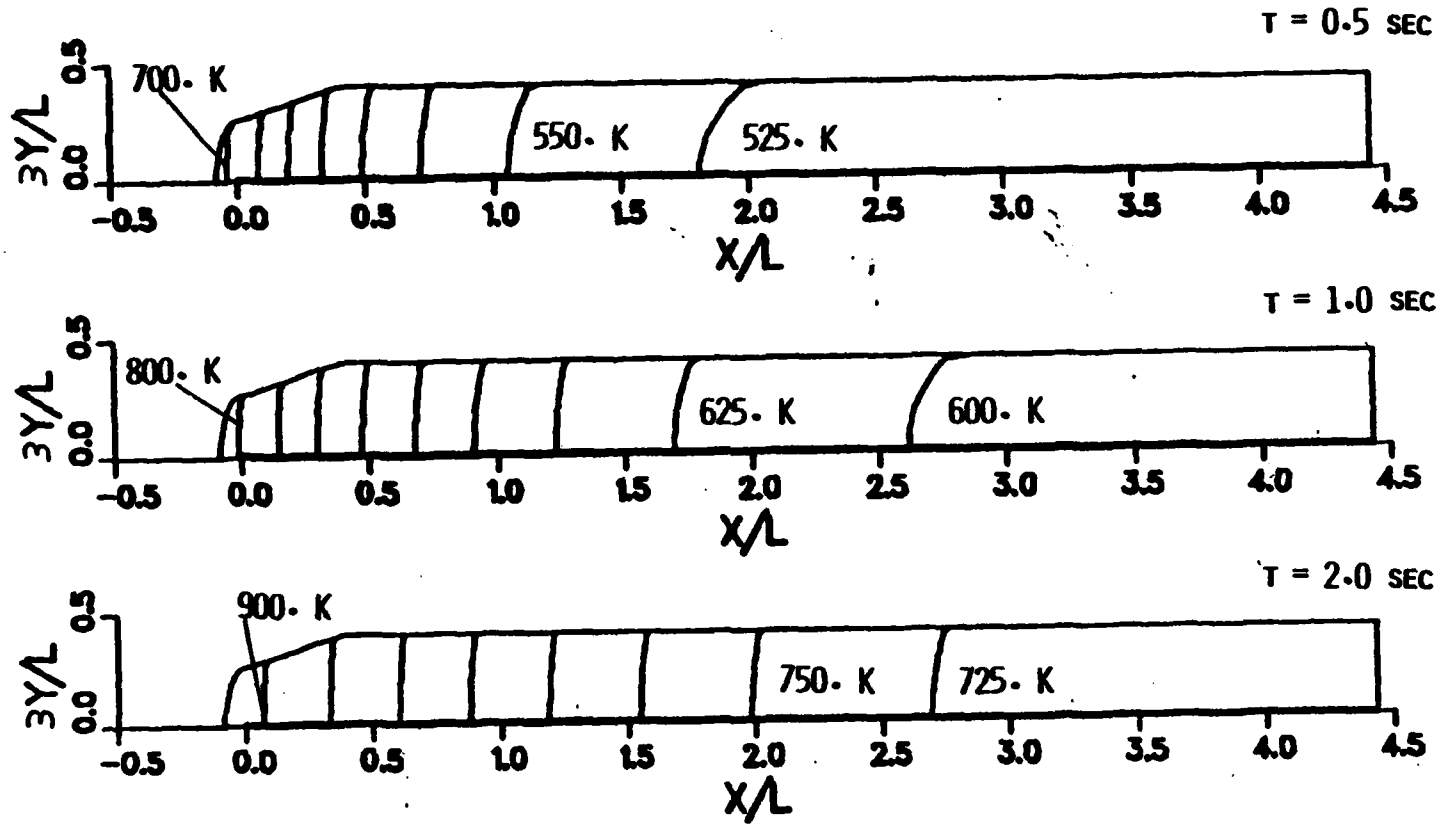

Figure 22. Continued

b. Section 2, Case ID 11

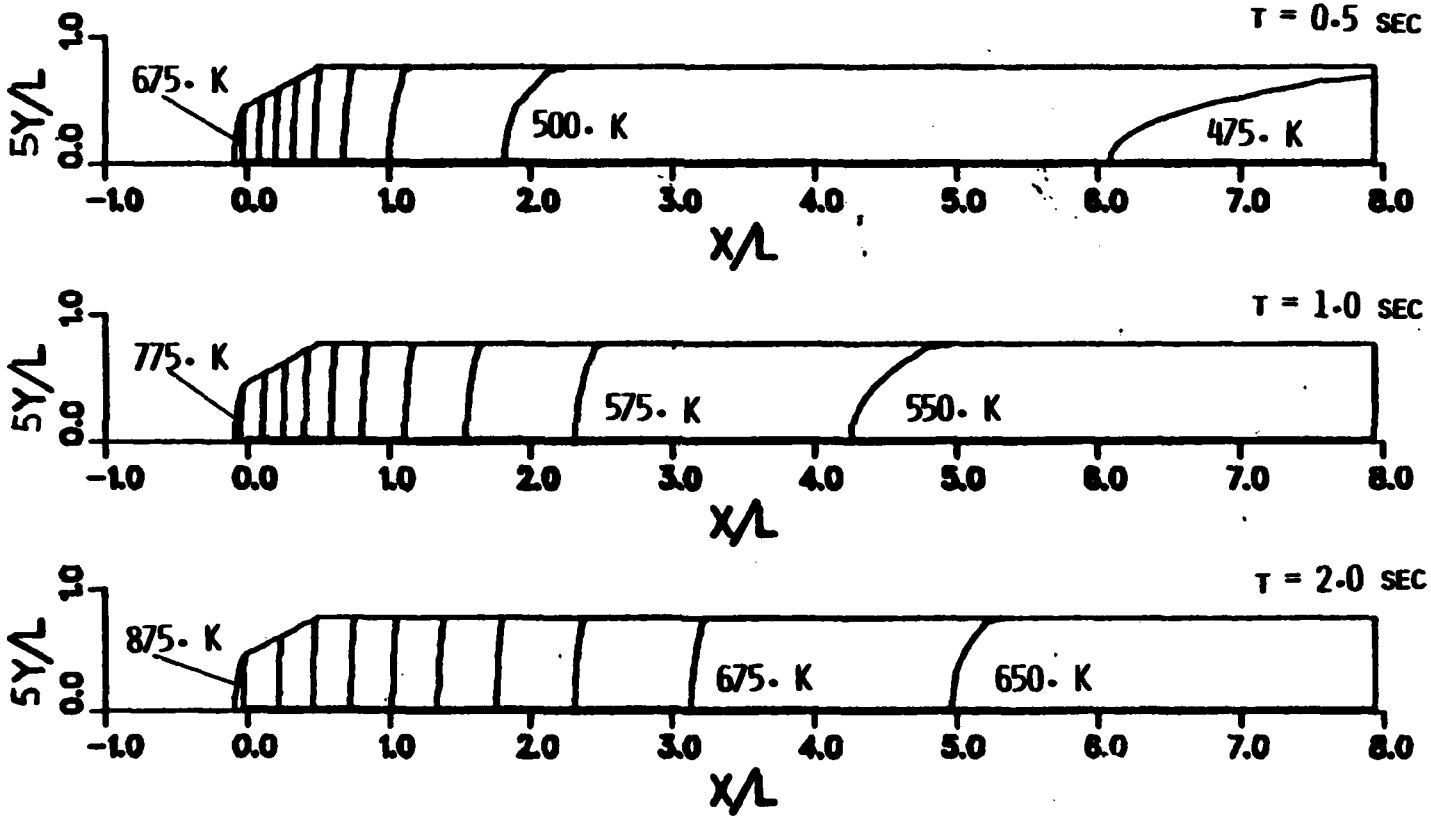

Figure 22. Continued

c. Section 3, Case ID 12

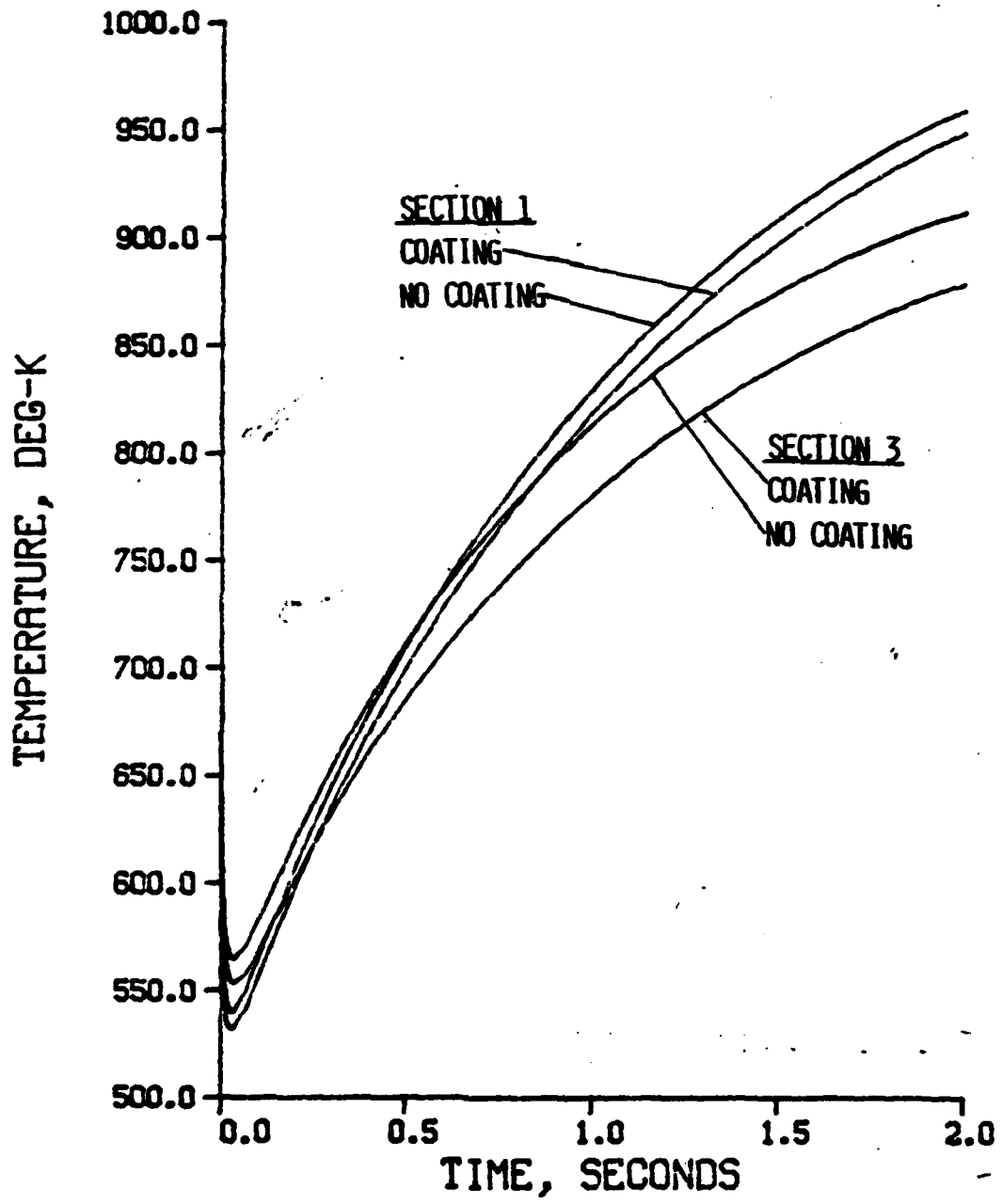

Figure 23. Temperature on Aluminum Surface at Leading Edge versus Time, Aluminum Fin with/without Hardcoating, Sections 1, 3, T_{flame} = 3500. K, Case ID 4, 10, 6, 12

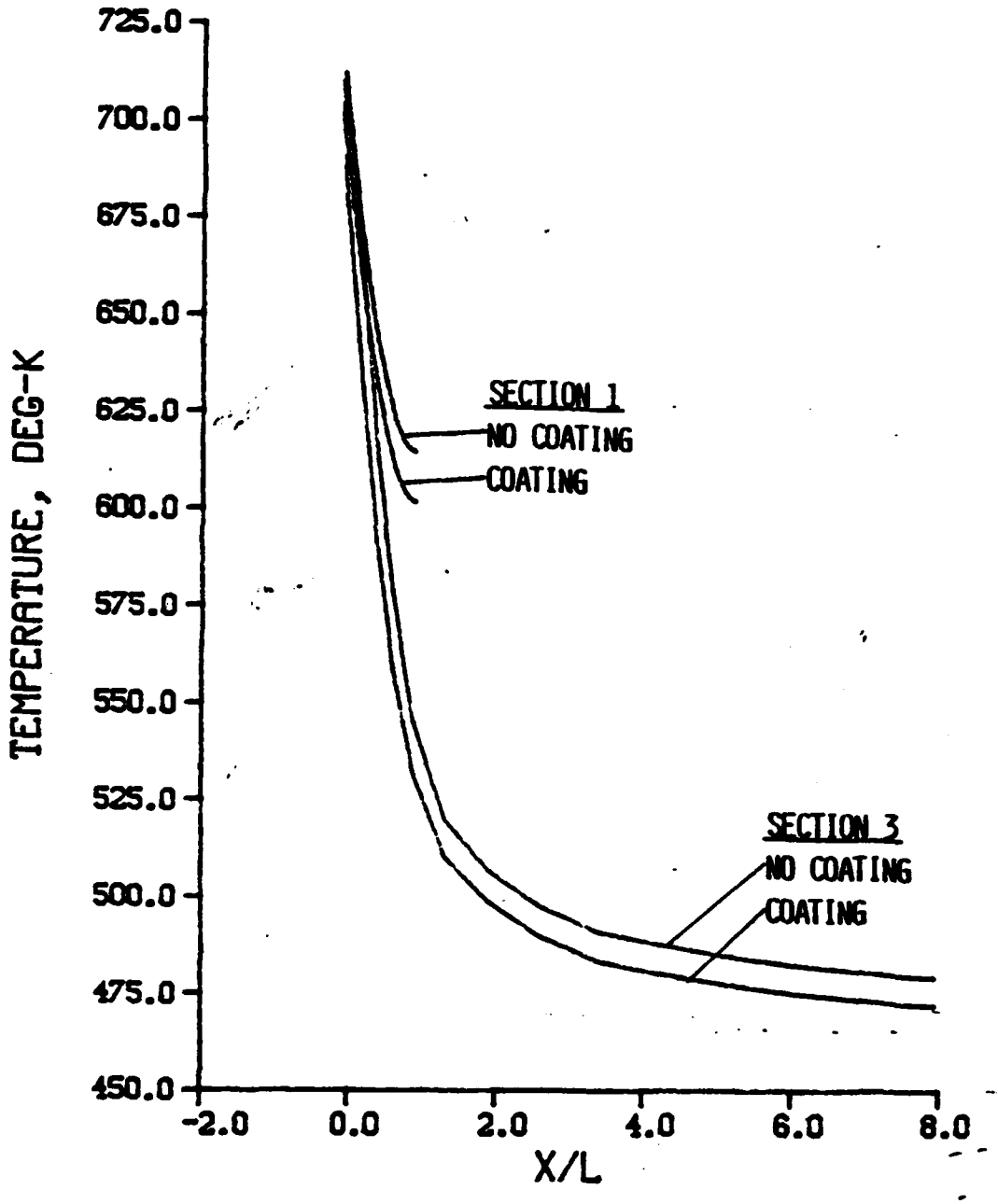

Figure 24. Temperature Along Fin Centerline, Aluminum Fin with/without Hardcoating, Sections 1, 3, T_{flame} = 3500. K, Case ID 4, 6, 10, 12

a. t = 0.5 seconds

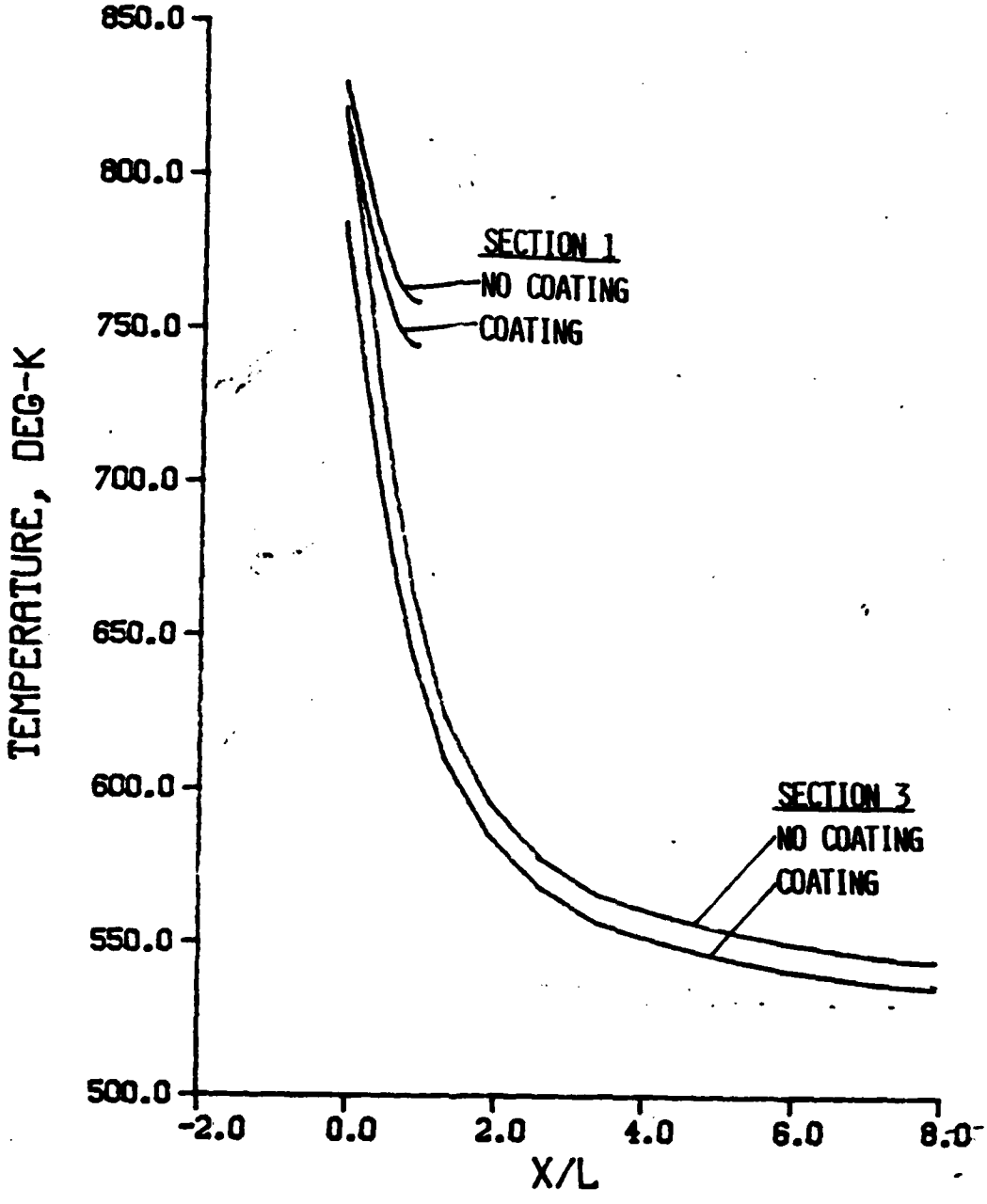

Figure 24. Continued

b. t = 1.0 seconds

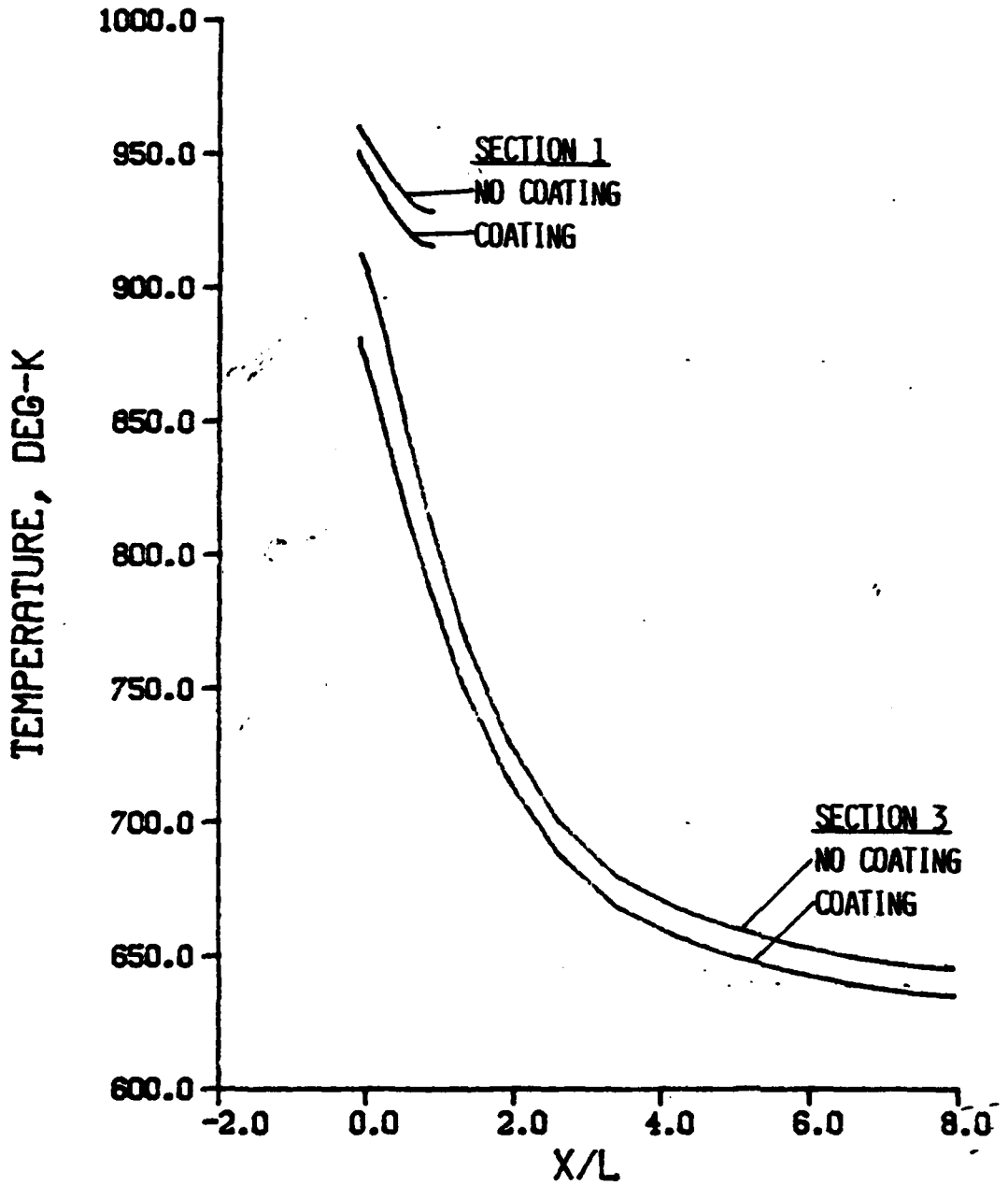

Figure 24. Continued

c. t = 2.0 seconds

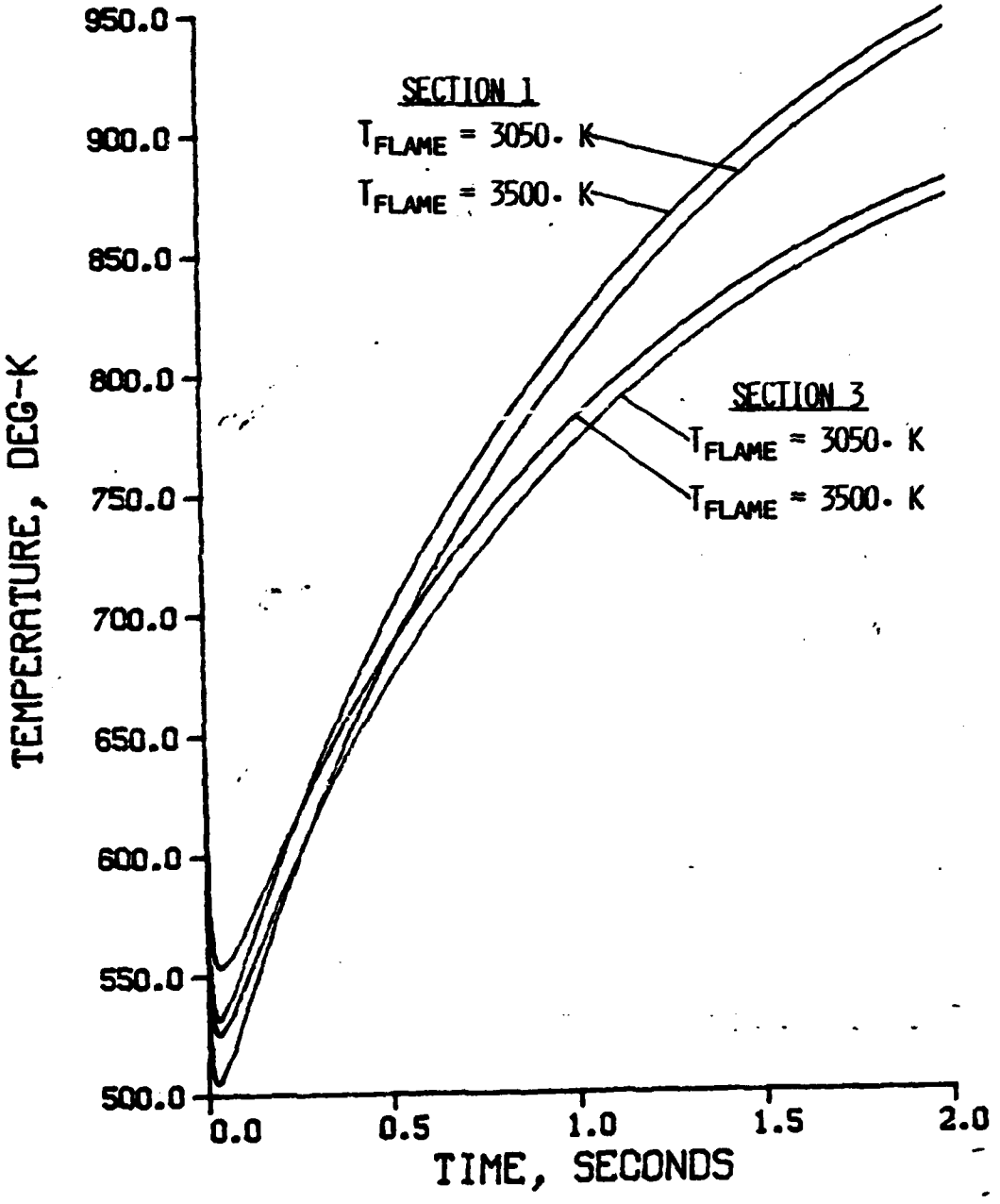

Figure 25. Temperature at Al/Al Oxide Interface on Leading Edge versus Time, Aluminum Fin with Hardcoating, Section 1, T_{flame} = 3050., 3500. K, Case ID 4, 10

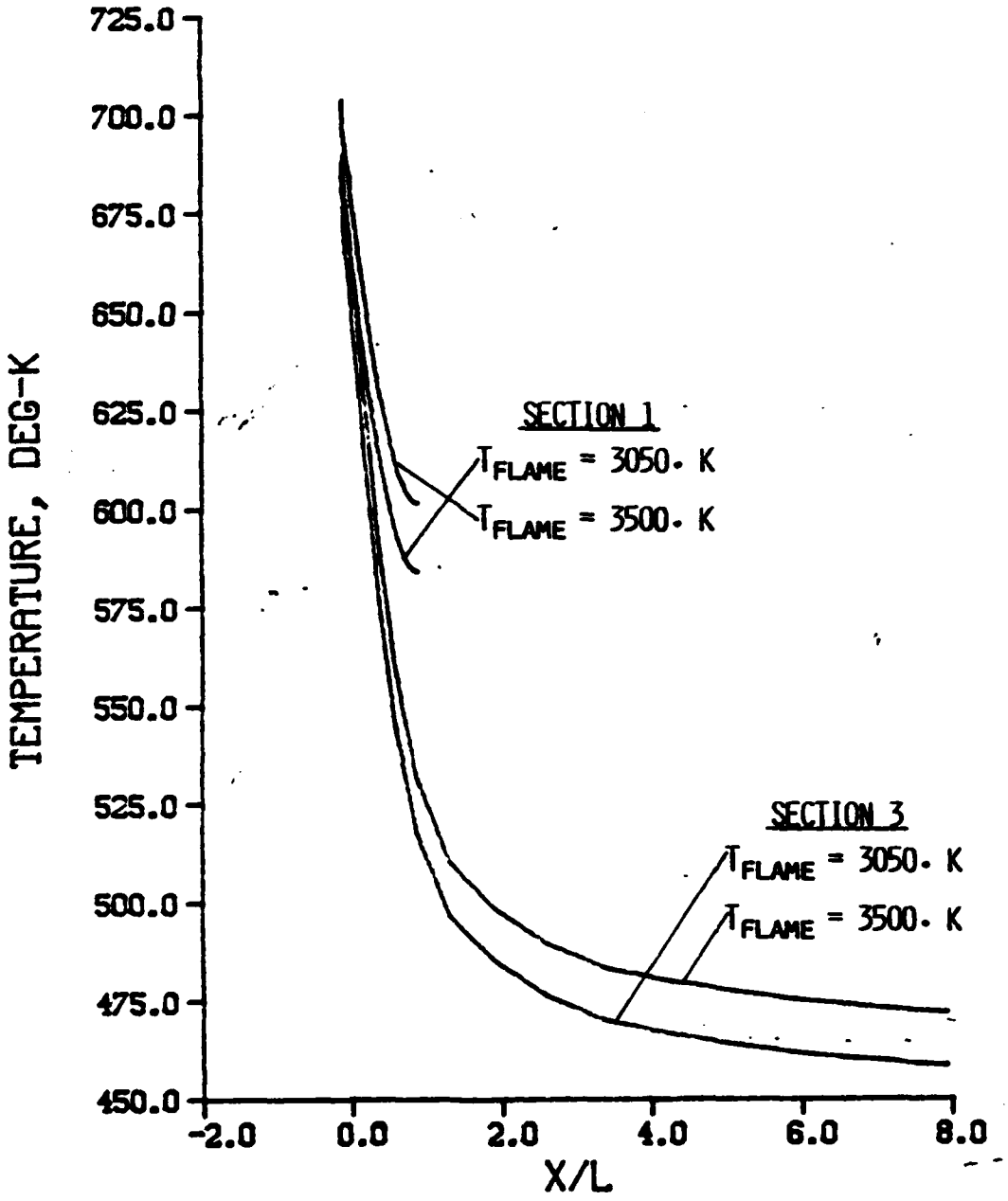

Figure 26. Temperature Along Fin Centerline, Aluminum Fin with Hardcoating, Sections 1, 3, T_{flame} = 3050., 3500. K, Case ID 7, 9, 10, 12

a. t = 0.5 seconds

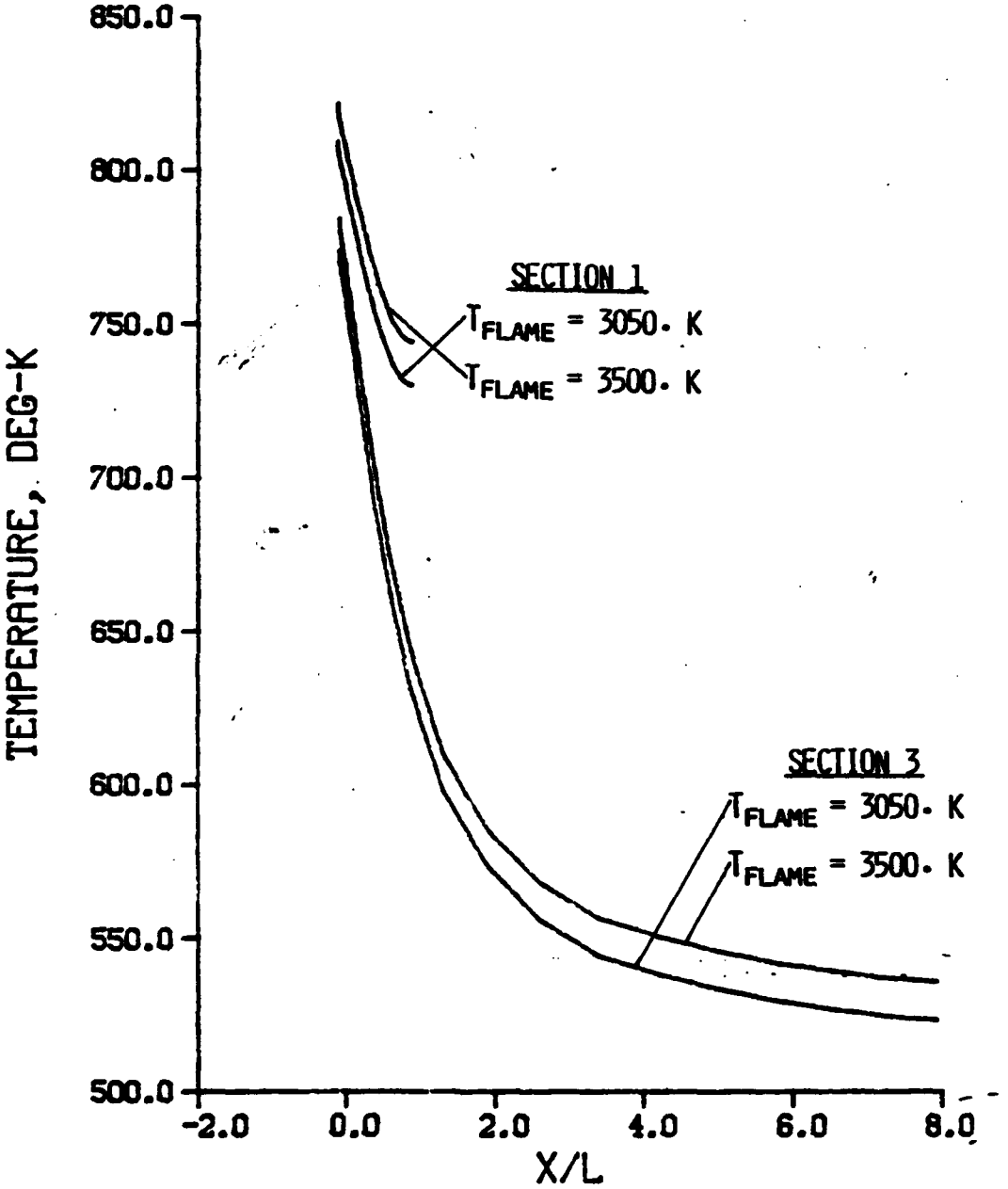

Figure 26. Continued

b. t = 1.0 seconds

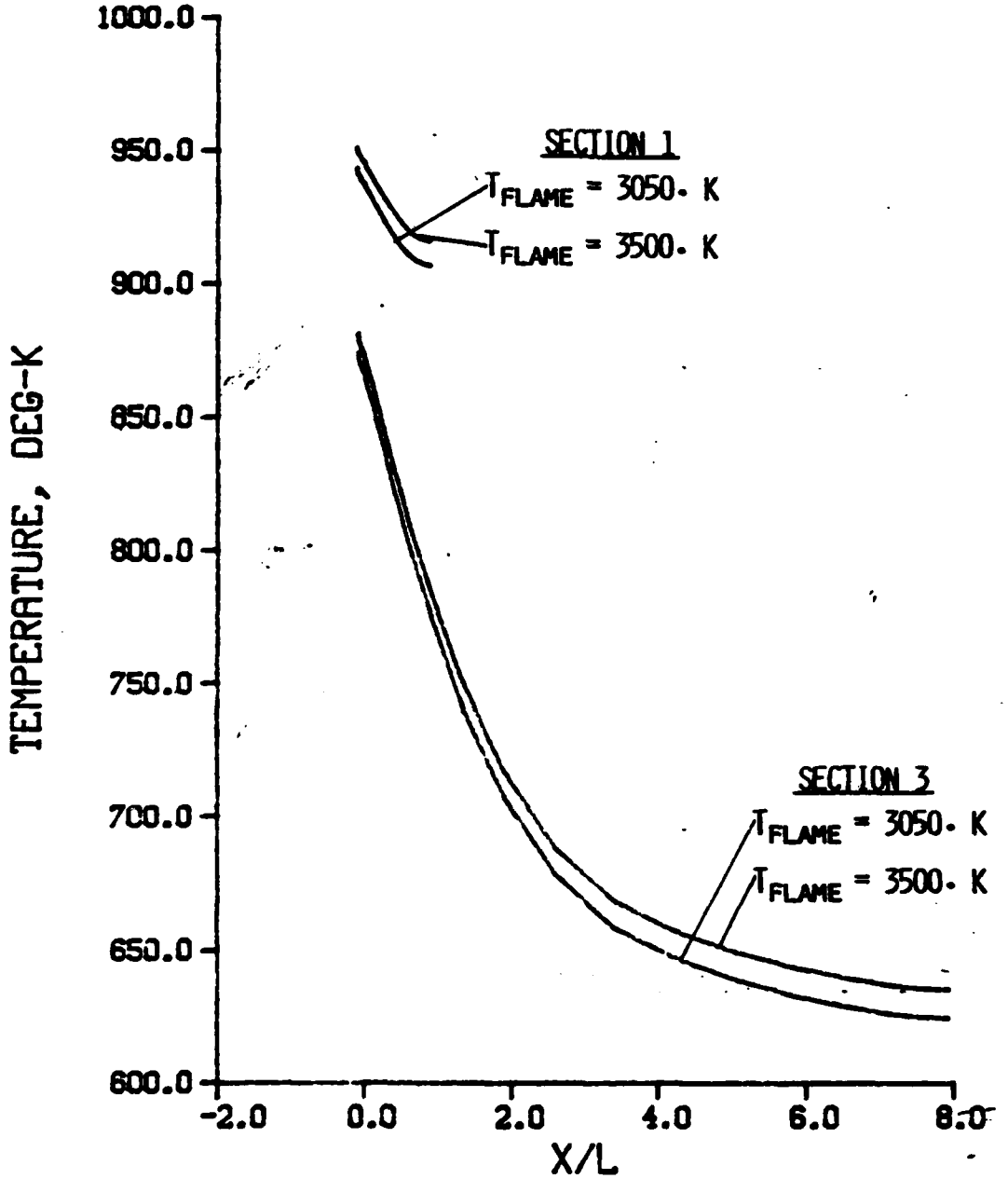

Figure 26. Continued

c. t = 2.0 seconds

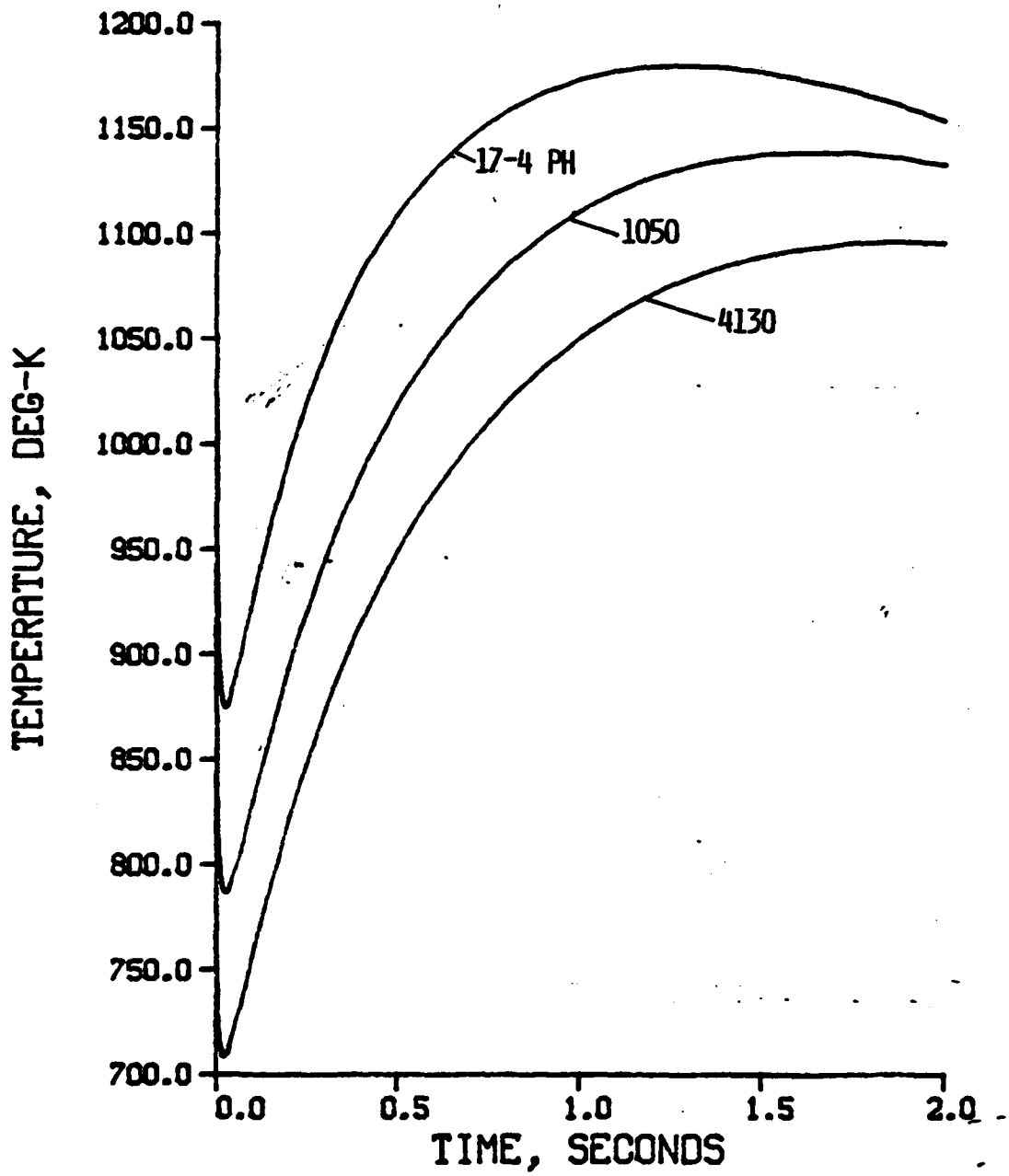

Figure 27. Temperature at Leading Edge versus Time, 4130, 1050, and 17-4PH Steel Fins, Section 1, T_{flame} = 3500. K, Case ID 13, 16, 19

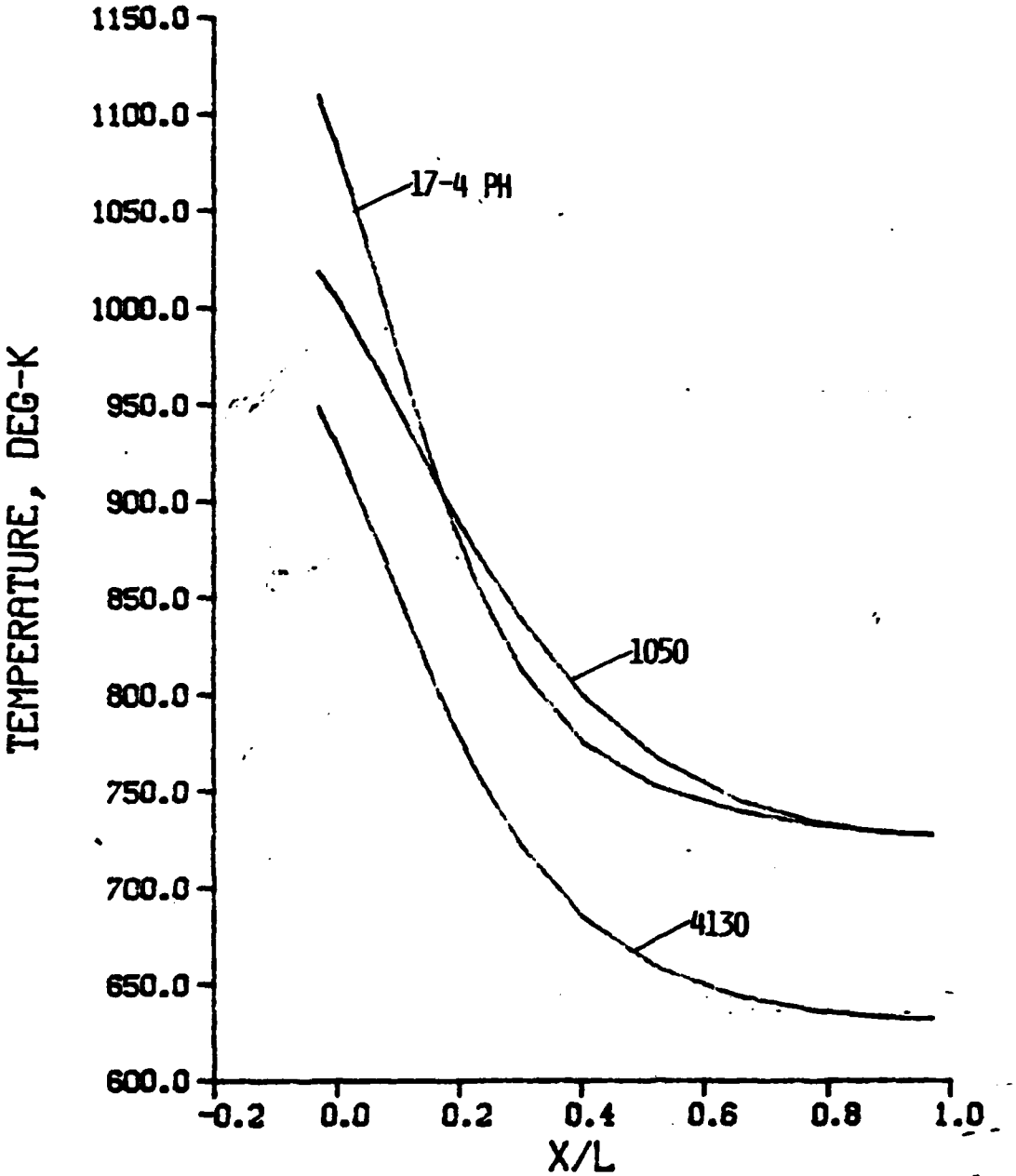

Figure 28. Temperature Along Fin Centerline, 4130, 1050, and 17-4PH Steel Fins, Section 1, T_{flame} = 3500. K, Case ID 13, 16, 19

a. t = 0.5 seconds

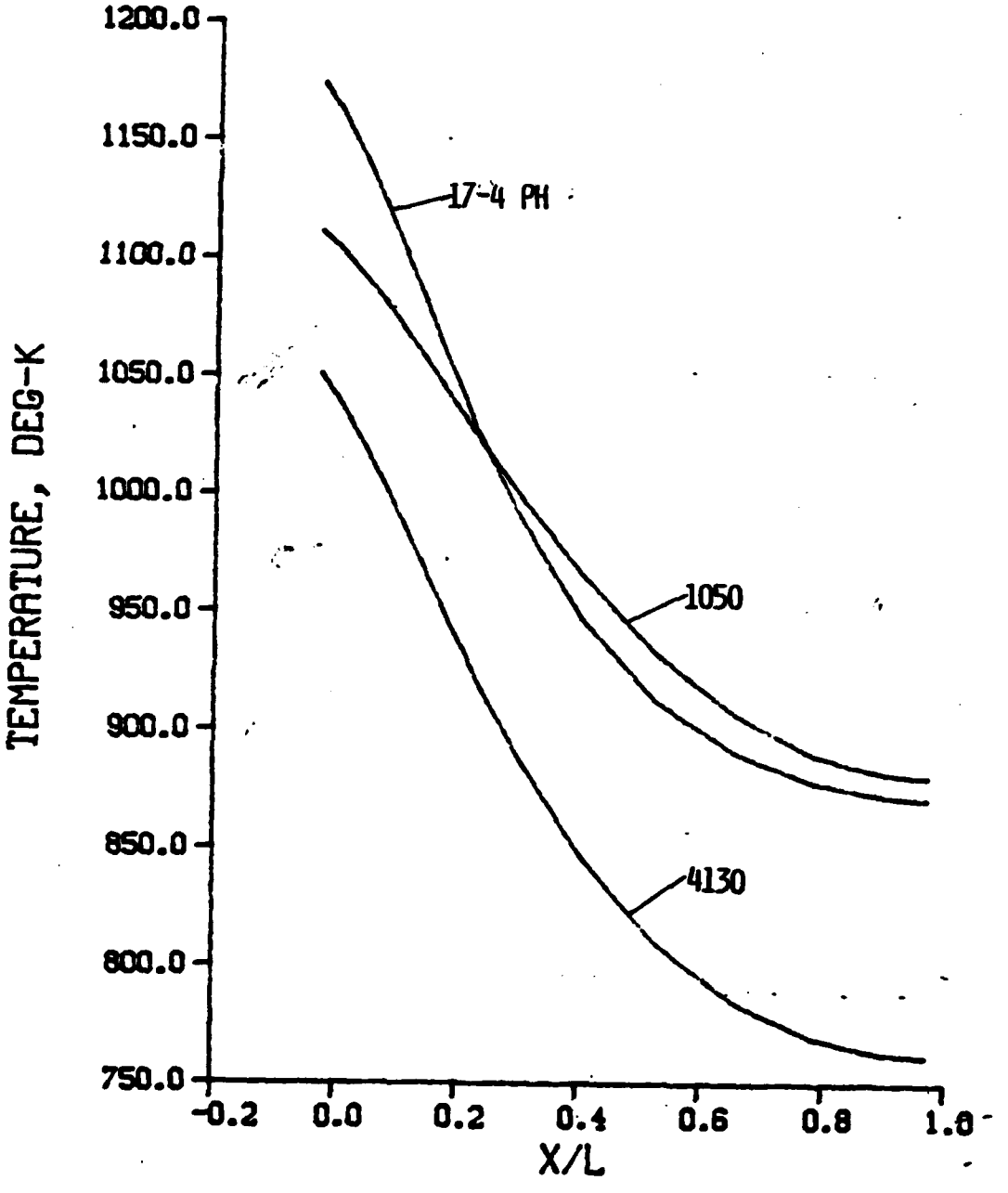

Figure 28. Continued

b. t = 1.0 seconds

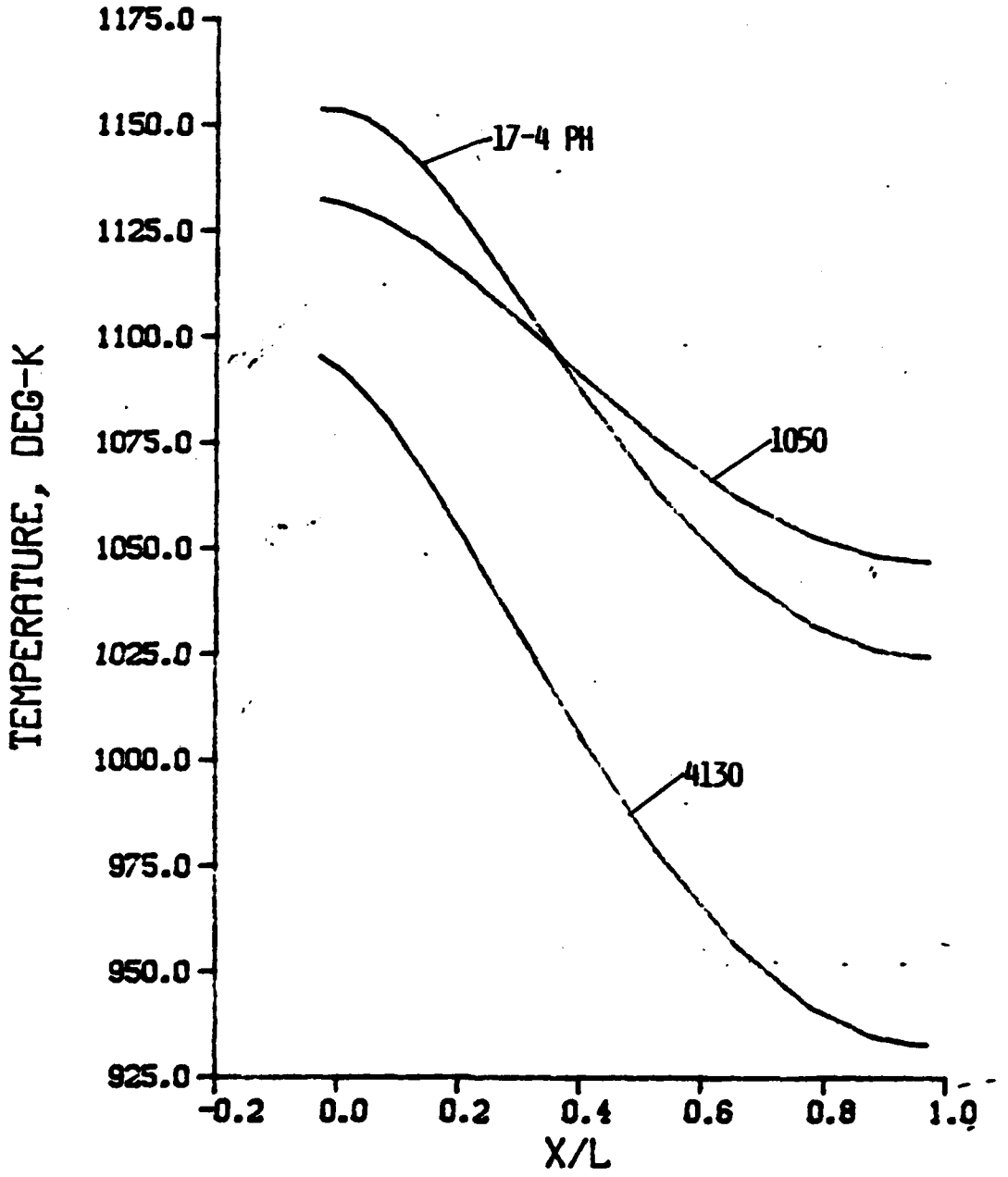

Figure 28. Continued

c. t = 2.0 seconds

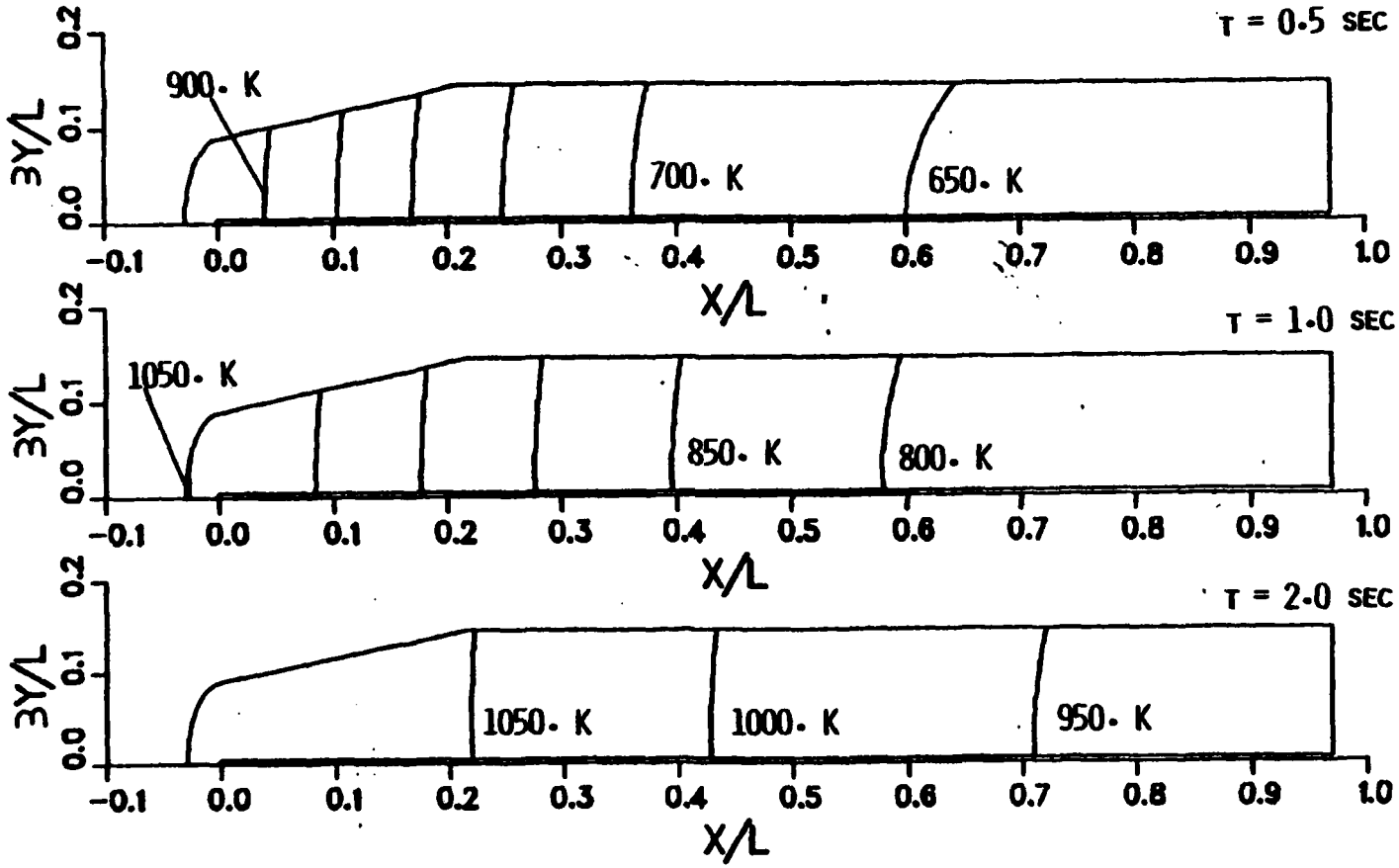

Figure 29. Inflight Temperature Contours, 4130 Steel Fin, T_{flame} = 3500, K

a. Section 1, Case ID 19

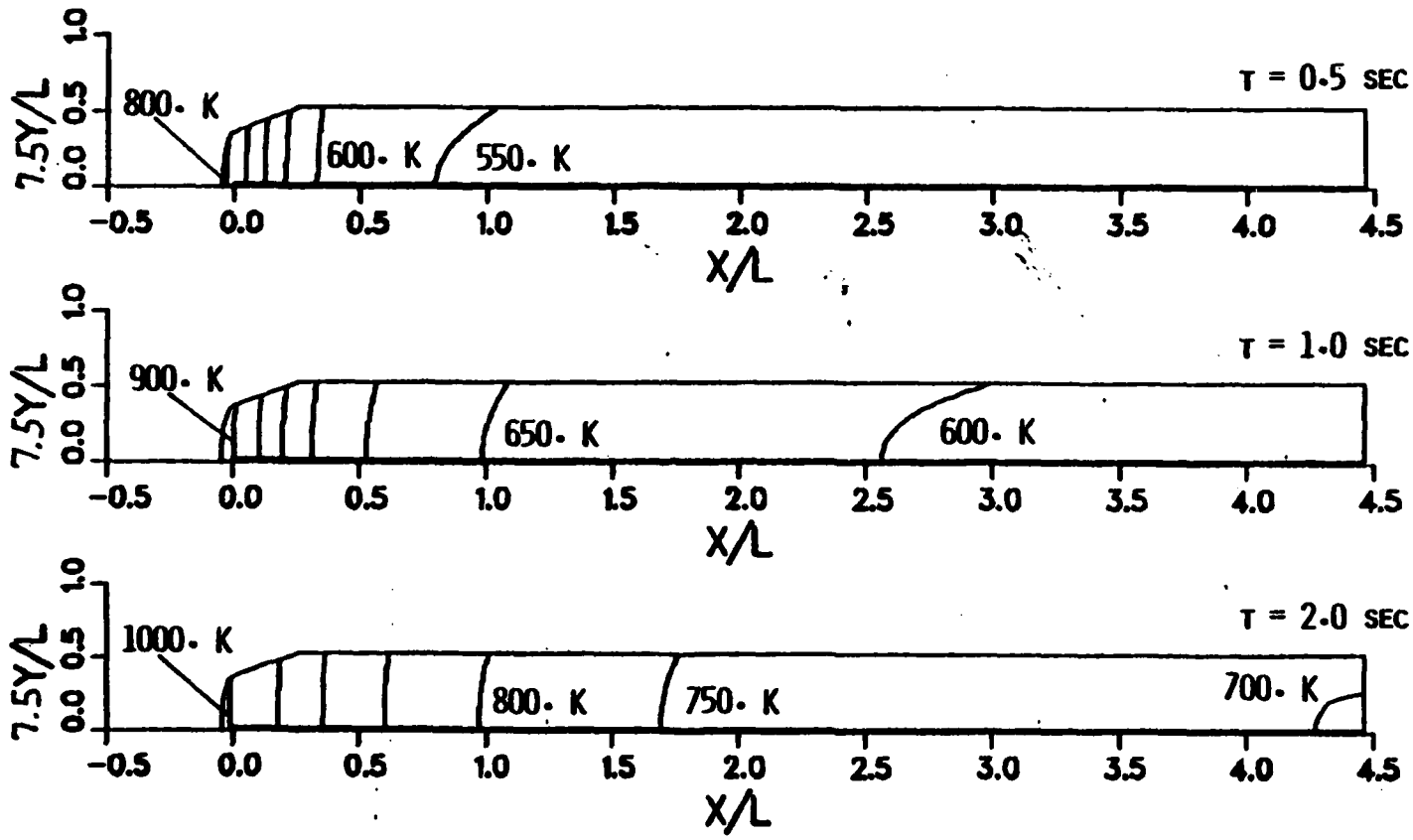

Figure 29. Continued

b. Section 2, Case ID 20

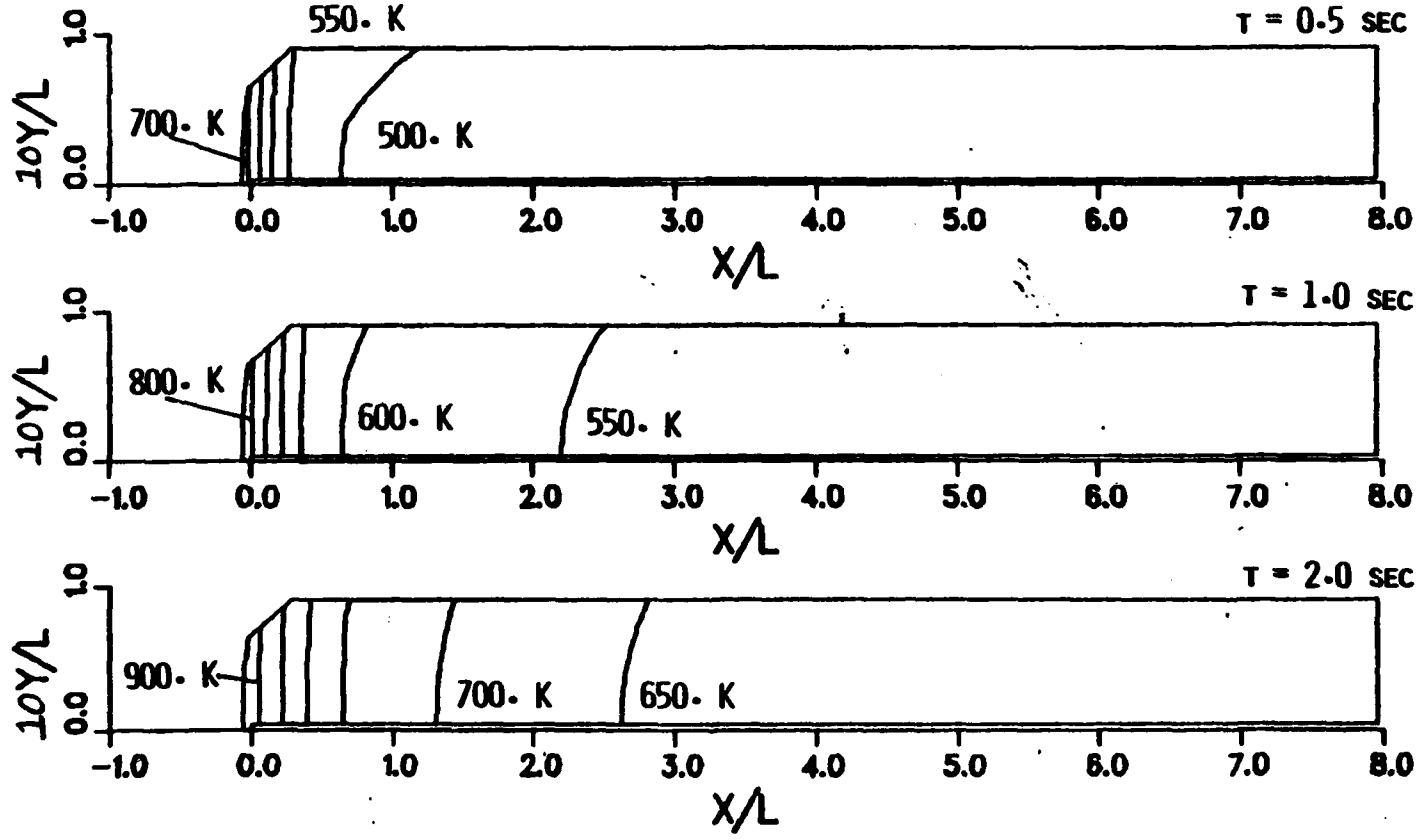

Figure 29. Continued

c. Section 3, Case ID 21

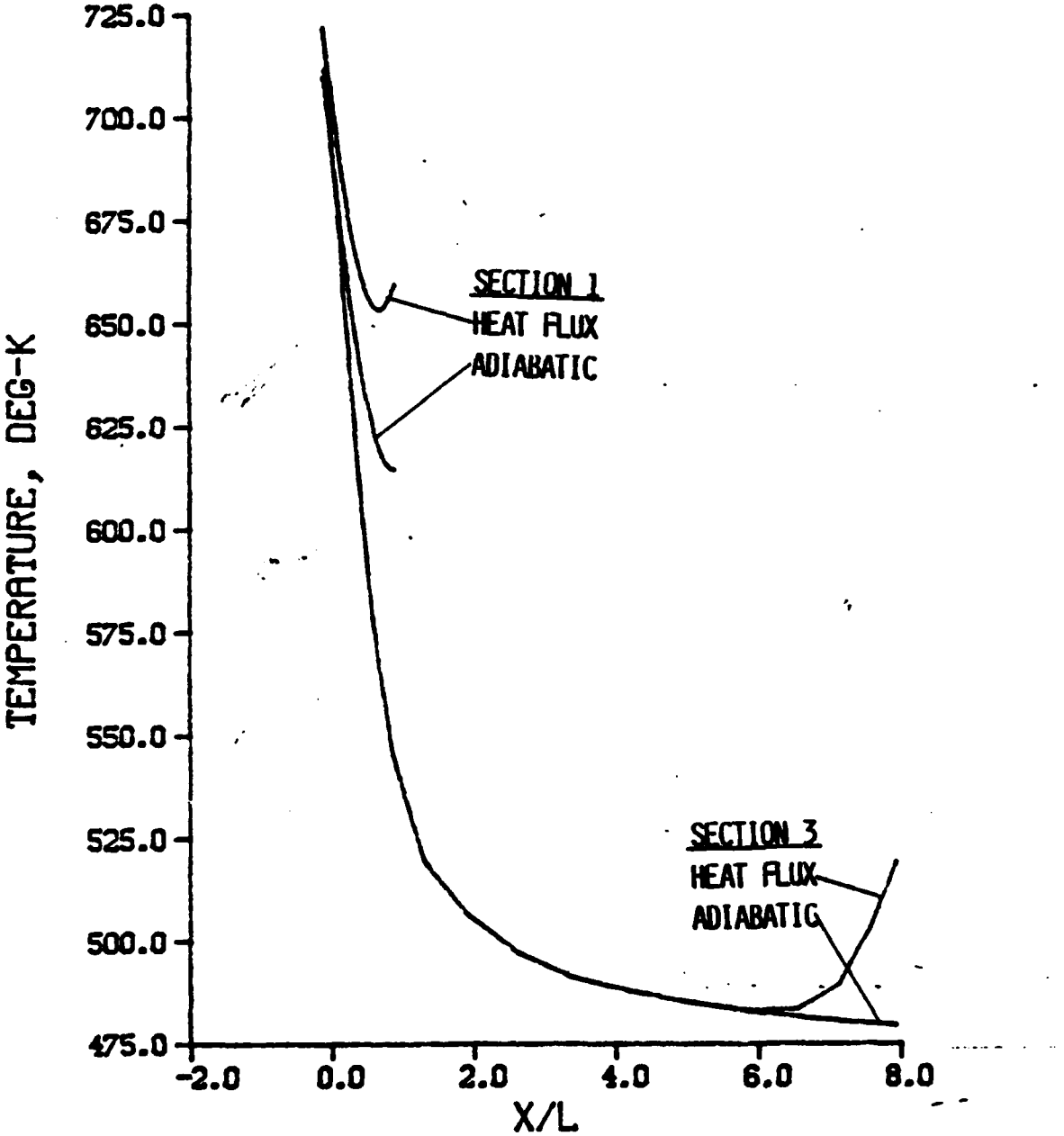

Figure 30. Temperature Along Fin Centerline, Aluminum Fin with No Hardcoat, T_{flame} = 3500. K, Sections 1, 3, Case ID 4, 6, 22, 24

a. t = 0.5 seconds

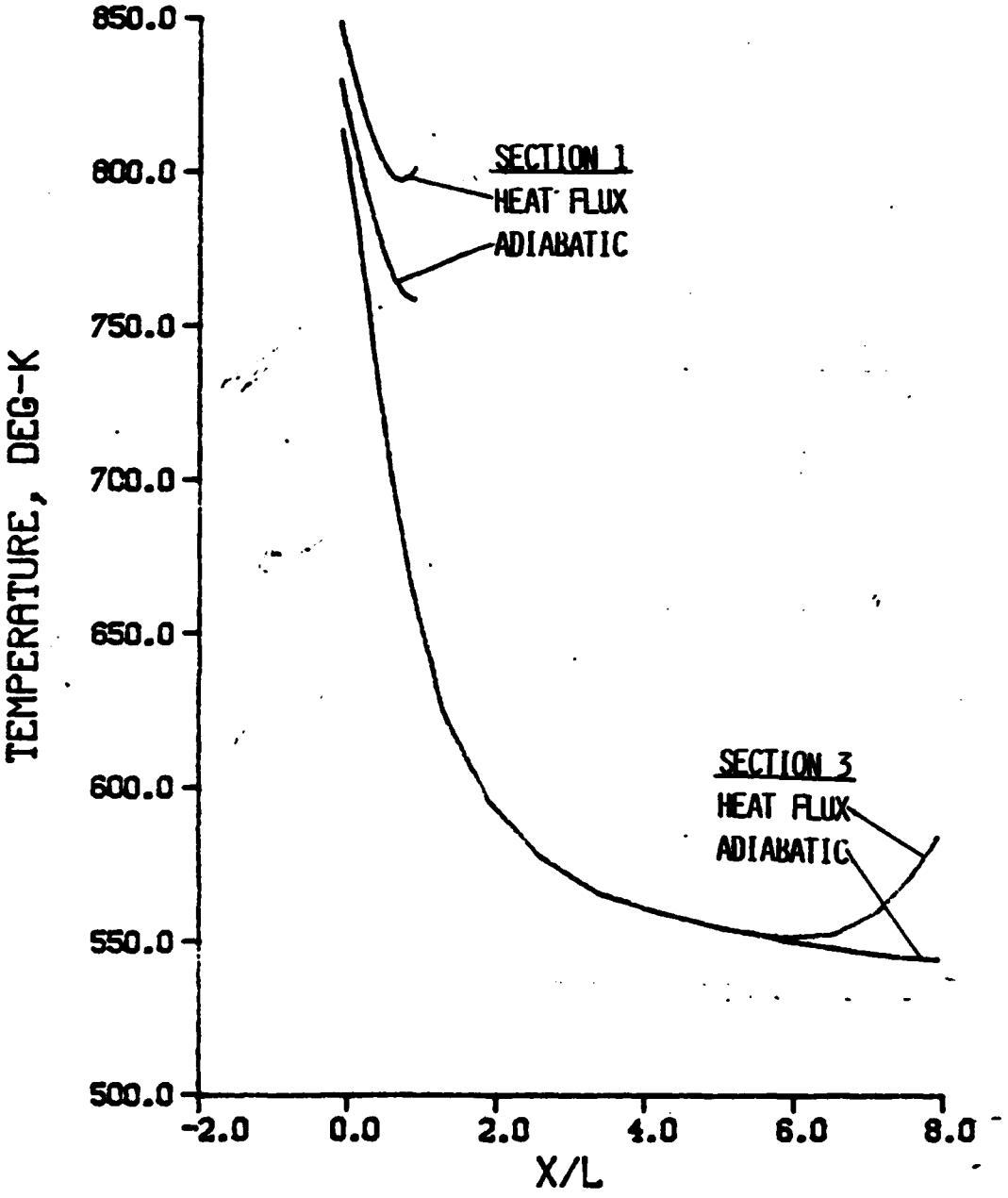

Figure 30. Continued

b. t = 1.0 seconds

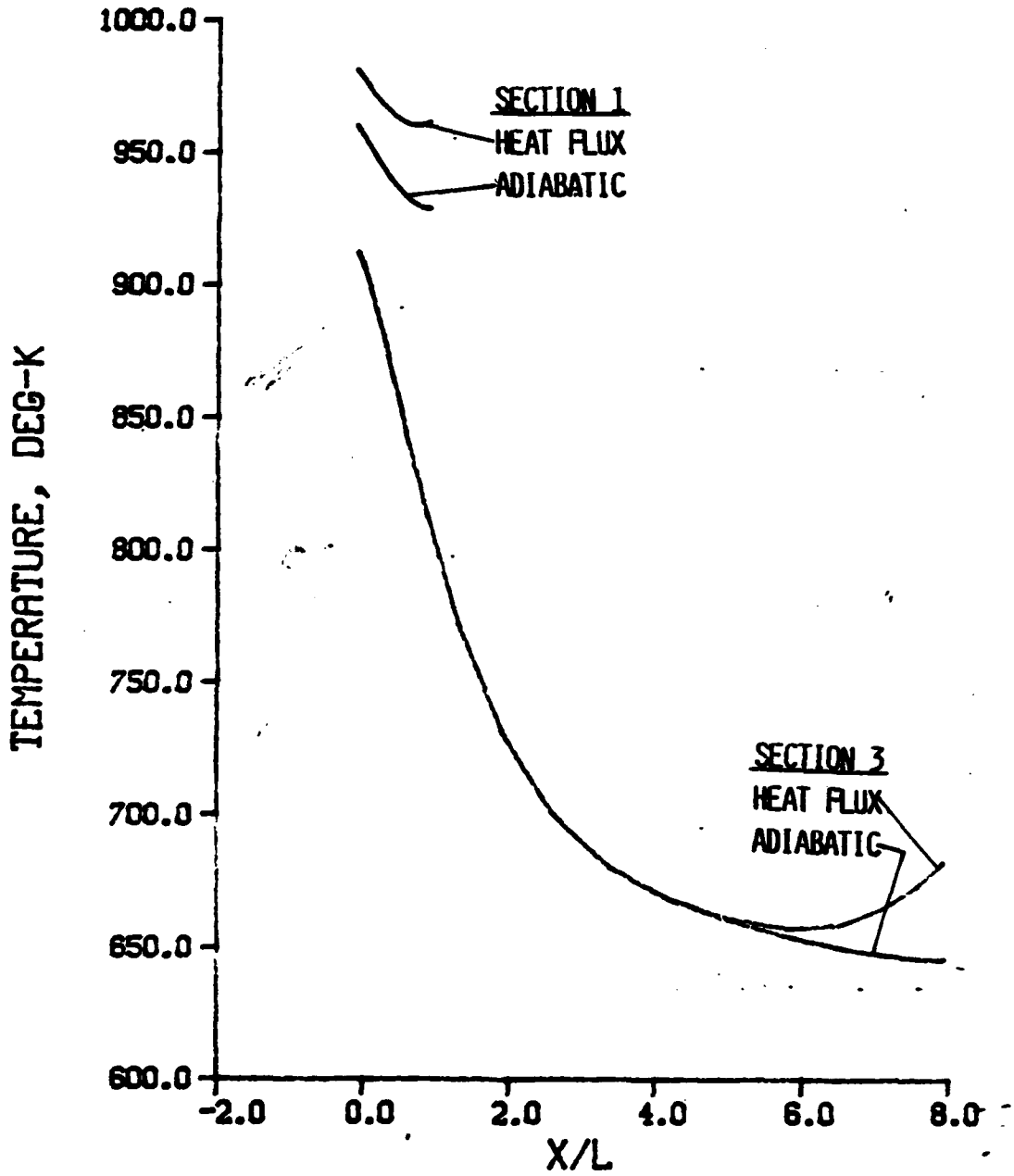

Figure 30. Continued

c. t = 2.0 seconds

REFERENCES

1. H. A. Dwyer, R. J. Kee, and B. R. Sanders,"Adaptive Grid Method for Problems in Fluid Mechanics and Heat Transfer," AIAA Journal, Vol. 18, No. 10, October 1980, pp1205-1212.

2. K. E. Suchland, "Aerothermal Assessment of Projectiles Using the ABRES Shape Change Code (ASCC)," Acurex Report TM-80-31-AS, June 1980.

3. W. B. Sturek, L. D. Kayser, and P. Weinacht, "Computational Study of Swept-Fin Aerodynamic Heating for the 105MM, M774," Ballistics Research Laboratory Memorandum Report to be published.

LIST OF SYMBOLS

h	heat transfer coefficient, kg/m^2 - s
H_{amb}	local recovery enthalpy, J/kg
H_{wall}	enthalpy at the fin surface, J/kg
k	thermal conductivity, W/m - K
L	chord length of fin section 1, m
n	unit normal to fin surface, m
R	leading edge radius of fin section 1, m
t	time, seconds
T	temperature, K
T_{flame}	flame temperature, K
X	chordwise coordinate, m
Y	cross fin coordinate, m
ξ, η	generalized coordinates, computational plane

DISTRIBUTION LIST

No. of Copies	Organization
12	Administrator Defense Technical Info Center ATTN: DTIC-DDA Cameron Station Alexandria, VA 22314
1	Commander US Army Materiel Development and Readiness Command ATTN: DRCDMD-ST 5001 Eisenhower Avenue Alexandria, VA 22333
8	Commander Armament R&D Center US Army AMCCOM ATTN: DRSMC-TDC (D) DRSMC-TSS (D) DRSMC-LCA-F (D) Mr. D. Mertz Mr. E. Falkowski Mr. A. Loeb Mr. R. Kline Mr. S. Kahn Mr. H. Hudgins Dover, NJ 07801
1	Commander US Army Armament, Munitions and Chemical Command ATTN: DRSMC-LEP-L(R) Rock Island, IL 61299
1	Director Benet Weapons Laboratory Armament R&D Center US Army AMCCOM ATTN: DRSMC-LCB-TL (D) Watervliet, NY 12189
1	Commander US Army Aviation Research and Development Command ATTN: DRDAV-E 4300 Goodfellow Blvd St. Louis, MO 63120
1	Commander US Army Missile Command ATTN: DRSMI-RDK, Mr. R. Deep Redstone Arsenal, AL 35898

No. of Copies	Organization
1	Director US Army Air Mobility Research and Development Laboratory Ames Research Center Moffett Field, CA 94035
1	Commander US Army Communications Research and Development Command ATTN: DRSEL-ATDD Fort Monmouth, NJ 07703
1	Commander US Army Electronics Research and Development Command Technical Support Activity ATTN: DELSD-L Fort Monmouth, NJ 07703
1	Commander US Army Missile Command ATTN: DRSMI-R Redstone Arsenal, AL 35898
1	Commander US Army Missile Command ATTN: DRSMI-YDL Redstone Arsenal, AL 35898
1	Commander US Army Tank Automotive Command ATTN: DRSTA-TSL Warren, MI 48090
1	Director US Army TRADOC Systems Analysis Activity ATTN: ATAA-SL White Sands Missile Range, NM 88002
1	Commander US Army Research Office P. O. Box 12211 Research Triangle Park, NC 27709

DISTRIBUTION LIST

No. of Copies	Organization
1	Commander US Naval Air Systems Command ATTN: AIR-604 Washington, D. C. 20360
2	Commander David W. Taylor Naval Ship Research and Development Center ATTN: Dr. S. de los Santos Mr. Stanley Gottlieb Bethesda, Maryland 20084
3	Commander US Naval Surface Weapons Center ATTN: Dr. F. Moore Mr. P. Daniels Mr. D. A. Jones 'II Dahlgren, VA 22448
4	US Naval Surface Weapons Center ATTN: Code 312 Dr. W. Yanta Code R44 Dr. C. Hsieh Dr. T. Zien Dr. R. U. Jettmar Silver Spring, MD 20910
1	Commander US Naval Weapons Center ATTN: Code 3431, Tech Lib China Lake, CA 93555
1	Director NASA Langley Research Center ATTN: NS-185, Tech Lib Langley Station Hampton, VA 23365
2	Commandant US Army Infantry School ATTN: ATSH-CD-CSO-OR Fort Benning, GA 31905
1	AFWL/SUL Kirtland AFB, NM 87117
1	ACUREX Corporation/Aerotherm Div ATTN: Mr. W. S. Kobayashi 555 Clyde Avenue P.O. Box 7555 Mountain View, CA 94039
1	Nielsen Engineering & Research, Inc. ATTN: Dr. S. Stahara 510 Clyde Avenue Mountain View, CA 94043
2	Sandia National Laboratory ATTN: Technical Staff, Dr. W.L. Oberkampf Aeroballistics Division 5631, H.R. Vaughn Albuquerque, NM 87115
1	Massachusetts Institute of Technology ATTN: Tech Library 77 Massachusetts Avenue Cambridge, MA 02139
1	University of Delaware Mechanical and Aerospace Engineering Department ATTN: Dr. J. E. Danberg Newark, DE 19711
	Aberdeen Proving Ground
	Dir, USAMSAA ATTN: DRXSY-D DRXSY-MP, H. Cohen
	Cdr, USATECOM ATTN: DRSTE-TO-F
	Cdr, CRDC, AMCCOM ATTN: DRSMC-CLB-PA DRSMC-CLN DRSMC-CLJ-L